Author:
Zhou, Liangzhi

Title:
Interfacial Adsorption and Structure on Graphene

Ion Adsorption, Air Bubbles, and Lipid Membranes

Interfacial Adsorption and Structure on Graphene: Ion Adsorption, Air Bubbles, and Lipid Membranes

Liangzhi Zhou

A dissertation submitted to the University of Bristol in accordance with the requirements for award of the degree of

Master of Science by Research

in the Faculty of Science, School of Chemistry

September 2018

Number of words: 28,302

Abstract

Graphene has shown its potential in bio-sensing. However, the cytotoxicity of graphene could restrict its applications in biotechnology. To improve the biocompatibility, one feasible solution is to functionalise graphene with biomolecules, such as lipids, to prevent direct contact of graphene from cell membranes. Therefore, understanding the structure of graphene in aqueous media the adsorption behaviour of lipids on graphene becomes important.

In this study, synchrotron X-ray reflectivity (XRR) has been applied to investigate the surface structure of graphene in air and in aqueous media, and also the interaction between graphene and liposomes of 1,2-dioleoyl-sn-glycero-3-phosphocholine (DOPC) or 1,2-dipalmitoyl-sn-glycero-3-phosphocholine (DPPC). X-ray photoelectron spectroscopy, photoemission electron microscopy, ellipsometry, atomic force microscopy, and contact angle measurement have been performed as complementary techniques to evaluate the composition, morphology, and the surface chemistry of the graphene substrates. The influences of temperature, the presence of ions (provided by phosphate buffered saline), and overnight water submergence on the surface structure of graphene and the graphene/lipid interaction have been examined.

The characterisation of bare graphene indicates the samples consisted of 3 - 4 layers of graphene, which should be accurately described as few layer graphene (FLG). In addition, a "contaminant" layer, comprising polymethylmethacrylate and graphene multilayers, was found present atop FLG. In aqueous systems, a diffuse layer of air bubbles was found immediately adjacent to FLG, which diminished after soaking. Tentative results showing the effects of temperature on the FLG thickness and affinity to ions have also been reported.

Both DOPC and DPPC were observed to form monolayer on the un-soaked FLG, but bilayer on the soaked FLG, due to the enhanced FLG hydrophilicity after soaking. The morphologies of lipid membranes were found to be temperature dependent. Our results have provided a new understanding of the morphology of lipid membranes on graphene and also demonstrated the capability of XRR – as a rigorous and quantitative method - to probe the surface and interfacial structures of graphene coated with biomolecules.

Acknowledgements

First of all, I would like to thank my supervisor Dr. Wuge H. Briscoe for his guidance throughout this project, without which this dissertation wouldn't be accomplished. Also, I would like to thank all my collaborators. I am grateful to Dr. Oier Bikondoa, the beamline scientists in XMaS ESRF, who kindly provided useful advice during the XRR experiments. I also appreciate all the help received from Dr. Robert Harniman and Dr. Mattia Cattelan, on AFM imaging and NanoESCA facilities, respectively. Furthermore, I would like to thank Dr. Luisa Islas Flores, Dr. Magdalena Wołdek, Anna Slastanova, Laura Fox, Nick Tylor, for their help and accompany at the beamline. I would also like to thank Eloise Creed and Michael Greaves for their demonstrations on DLS and the extruder.

Many thanks go to all the other (former) members of the Briscoe group, especially to Charlotte, Christian, Dajana, Lauren, and Tim who have created cheerful academic atmosphere and honourable traditions in office E024, Silvia who has cultivated my obsession with tiramisu, Sarah and Patryk who kindly chair the weekly group meetings, and Ben who is also working with lipids. It is my luck to work and befriend with these wonderful individuals.

I really appreciate the emotional support and encouragements from all my families, friends and Dr. Tian.

Last but not least, I would like to thank my father, Di, who sponsored me to do this research degree in University of Bristol, which has become and will remain to be one of the most valuable experiences in my life.

Author’s Declaration

I declare that the work in this dissertation was carried out in accordance with the requirements of the University's Regulations and Code of Practice for Research Degree Programmes and that it has not been submitted for any other academic award. Except where indicated by specific reference in the text, the work is the candidate's own work. Work done in collaboration with, or with the assistance of, others, is indicated as such. Any views expressed in the dissertation are those of the author.

SIGNED: ..... DATE: .....

Publications and Outputs

The following chapter is the basis of the publication listed below:

Chapter 3:

- **Zhou L.**, Fox L., Włodek M., Islas L., Slastanova A., Robles E., Bikondoa O., Harniman R., Fox N., Cattelan M., and Briscoe W. H., *Surface structure of few layer graphene.* Carbon, **2018**. 136: p. 255-261.

Chapter 4:

- **Zhou L.**, Islas L., Taylor N., Bikondoa O., Robles E., and Briscoe W. H., *Graphene surface structure in aqueous media: Evidence for an air-bubble layer and ion adsorption*. Carbon, **2019**. 143: p. 97-105.

The following chapters will form the basis of the publications listed below:

Chapter 5:

- **Zhou L.**, Islas L., O., Robles E., and Briscoe W. H., *Adsorption morphology of lipids on graphene surface*. (In preparation)

Additional publications:

- Włodek M., Kolasinska-Sojka M., Szuwarzynski M., Kereïche S., Kovacik L., **Zhou L.**, Islas L., Warszynski P., and Briscoe W. H., *Supported lipid bilayers with encapsulated quantum dots (QDs) via liposome fusion: Effect of QD size on bilayer formation and structure.* Nanoscale, **2018**. (In press, doi: 10.1039/c8nr05877f)

Contents

Abstract i

Acknowledgements iii

Author's Declaration v

Publications and Outputs vii

List of Tables xiii

List of Illustrations xv

Chapter 1 1

Introduction 1

1.1 Project Motivations 1

1.2 Brief Introduction to Graphene 2

1.2.1 Chemical vapour deposition of graphene 2

1.2.2 Influence of structure on graphene properties 3

1.3 Interaction between Biomolecules and Graphene 4

1.4 Brief Introduction to X-ray Reflectivity 5

1.4.1 X-ray 5

1.4.2 X-ray scattering 6

1.4.3 Specular reflection 7

1.4.5 X-ray reflection from layered interfaces 9

1.4.6 Scattering length density 12

1.5 Thesis Outline 13

Reference 15

Chapter 2 Methods 19

2.1 X-Ray Reflectivity 19

2.1.1 Experimental setup 19

2.1.2 Data analysis 20

2.1.3 Calculation of the SLD 24
2.2 Atomic Force Microscopy 27
2.3 Ellipsometry 27
2.4 NanoESCA Facilities 27
2.5 Dynamic Light Scattering 28
2.6 Contact Angle Measurement 30
References 31
Chapter 3 Surface Structure of Few Layer Graphene 33
3.1 Introduction 34
3.2 Experimental 37
3.2.1 Materials 37
3.2.2 Methods 37
3.3 Results and Discussion 38
3.3.1 The composition of the graphene samples 38
3.3.2 Structure of the graphene samples 40
3.4 Conclusions 46
References 48
Chapter 4 Graphene surface structure in aqueous media 53
4.1 Introduction 54
4.2 Experimental 55
4.2.1 Materials 55
4.2.2 Methods 55
4.3 Results and Discussion 56
4.3.1 XRR of the graphene-water interface 56
4.3.2 AFM imaging at the graphene-water interface 59
4.3.3 Effect of submerging CVD graphene on Si/SiO_2 under water 62

4.3.4 Effect of temperature and PBS on CVD graphene on Si/SiO_2 66
4.4 Conclusions 67
References 69
Chapter 5 Adsorption morphology of lipids on graphene surface 73
5.1 Introduction 74
5.2 Experimental 76
5.2.1 Materials 76
5.2.2 Sample preparation 76
5.2.3 Dynamic light scattering 77
5.2.4 X-Ray reflectivity 77
5.3 Results and Discussion 79
5.3.1 Influence of graphene wettability on the morphology of the adsorbed lipids 79
5.3.2 Influence of temperature on thickness and coverage of the lipid membrane 86
5.4 Conclusions 97
Reference 99
Chapter 6 Conclusions and future work 103
6.1 Conclusion 103
6.2 Future Work 104
Reference 107
Appendix 109
I. XPS Fittings and PEEM Results 109
II. Histogram Analysis of AFM Results 111
III. Contact Angle Measurement 112
IV. DLS Results 115
V. XRR Data Fitting 116

VI. DOPC Multilayers Formed on Graphene 126

VII. Publications and manuscripts 135

References 159

List of Tables

Table 2.1. The abbreviation, molecular formula, headgroup and carbon tail structures, molecular weight (M_w) and the transition temperature Tm of the lipids used for interacting with graphene surfaces..... 25

Table 2.2. The molecular volume (V) and corresponding real part of SLD (ρ_r) of the segments that compose lipids. The V values are cited from the studies reported by [a] Armen [11], and [b] Nagle [13]. 25

Table 2.3. Calculated ρ (with a beam energy of 14 keV). 26

Table 3.1. A summary of few well-established structural characterisation methods for graphene. 36

Table 3.2. Fitted XRR results of graphene on Si/SiO_2 samples in air at RT. The samples were purchased in 2 batches, namely [a] and [b]. 44

Table 3.3. Fitting parameters for XRR results of FLG in air at different temperatures, using the three layer model (*cf*. Figure 3.3a). The SLD (ρ) of graphene and SiO_2 were fixed during fitting, and that of the contaminant layer was fitted in the range between air to FLG, since it is presumed a layer of a mixture with limited coverage instead of a homogeneous film. Also listed are the two fitted interfacial roughness values, $R_{a,c}$ for the roughness at the interface between air and the "contaminant" layer (thus the subscript c) and $R_{a,g}$ for that at the interface between the "contaminant" layer and the graphene layer. 45

Table 4.1. Fitting parameters for the XRR data collected from graphene in air, in water, in PBS, and 24 h water-soaked graphene in water at 25 ºC. 59

Table 4.2. The maximum difference in the relative height, Δh_{max}, the root-mean square average, R_{sq}, and the arithmetic average values of height deviations, R_{ave}, of the surface height deviations in the AFM topological images of graphene in air and in water following the plane fitting. 61

Table 5.1. Membrane morphologies formed on graphene in water or PBS. 83

Table 5.2. Fitted bilayer structures of DPPC and DOPC formed on graphene. t_n, $R_{a,n}$, and ϕ_n denote the thickness, the roughness, and the lipid volume fraction of the n^{th} slab, respectively. The bilayers were prepared via vesicle fusion in PBS on the soaked

graphene, and the data were collected at 25 °C after incubating at 60 °C for 3 h and rinsing with PBS at 25 °C. 85

Table 5.3. Fitted parameters of the lipid membranes for XRR curves shown in Figure 5.5. t_H, $R_{a,H}$, ϕ_H, and t_T, $R_{a,T}$, ϕ_T are the thickness, roughness, the coverage of the lipid headgroup (H) and hydrocarbon tails (T), respectively. The total thickness of the monolayer membrane is represented by t_{mono}.....88

Table 5.4. Summary of the t_n, $R_{a,n}$, and ϕ_n of the slabs comprising the DPPC bilayer at different temperatures, obtained from fitting the XRR curves shown in Figure 5.7.....93

Table 5.5. Comparison between the lipid membrane thickness obtained from our results and in literature.....95

Table S1. Peak fittings of XPS results. 110

Table S2. Peak fittings for the histograms of the selected areas shown in Figure S3a, showing the peak height scales of the silica (h_s) substrate and graphene (h_g), the difference between the two peaks (Δh), and the coverage of graphene (ϕ_g). 111

Table S3. Contact angle measurements of graphene at 26.3 ºC.....112

Table S4. WCA of graphene before and after soaking. After soaking, the graphene samples were dried by two methods: (i) shaking the water off, and letting it dry naturally[a], or (ii) using an argon flow to dry the surface carefully[b]. 115

Table S5. The fitted D_z and PDI of the liposomes that had been used in the synchrotron experiments. 116

Table S6. Best fits for the studied XRR data in aqueous systems. 117

Table S7. Best fits for all the collected XRR data. The fitted thickness, SLD, and roughness of the n^{th} slab are denoted by t_n, ρ_n, and $R_{a,n}$, respectively. DOPC-H, DOPC-T, DPPC-H, and DPPC-T represent the headgroup, hydrocarbon tail slabs of the DOPC and DPPC monolayers, respectively. DOPC-H (i), DOPC-T (i), DOPC-H (o), DOPC-T (o), DPPC-H (i), DPPC-T (i), DPPC-H (o), DPPC-T (o) represent the headgroup, hydrocarbon tail slabs of the DOPC inner/outer leaflets, and DPPC inner/outer leaflets, respectively. 120

Table S8. Summary of the DOPC multilayer structure.....131

List of Illustrations

Figure 0.1. Illustration of a typical synchrotron with the arrays showing the direction of the moving electron bunches [42]. 5

Figure 0.2. The Bragg scattering geometry. $\boldsymbol{k}_\mathbf{i}$, $\boldsymbol{k}_\mathbf{f}$, θ, and d denote the wavevector of the incident and reflected beams, the angle of incidence, and the lattice spacing, respectively. 7

Figure 0.3. Illustration of a reflection from an interface. $\boldsymbol{k}_\mathbf{i}$ and $\boldsymbol{k}_\mathbf{f}$ represent the wavevectors of the beam of incidence and reflection, respectively. $\boldsymbol{Q}$ denotes the wavevector transfer. 7

Figure 0.4 Reflection and refraction of a beam from an ideal surface with a refractive index of n, $\boldsymbol{k}_\mathbf{i}$, $\boldsymbol{k}_\mathbf{f}$, and $\boldsymbol{k}_\mathbf{t}$ are the wavevectors of the incident, reflected, and transmitted beams, respectively. θ represents the angle of incidence. x and z are the parallel and perpendicular axis. 9

Figure 0.5 Reflection of X-rays from an interface region modelled as a series of uniform layers. The figure is reproduced from reference [45]. 10

Figure 0.6 Example reflectivity curve with intensity plotted as log$R$ against the wavevector transfer $\boldsymbol{Q}$. Q_c is the respective wavevector of the critical angle θ_c, and the layer thickness d can be estimated from the spacing of the Kiessig fringes (the interference oscillations), ΔQ. 12

Figure 2.1. Key components of the XRR cell, consisting of three stainless steel plates (B-D), and the cooling (A) and heating jackets (E). Two Mylar® windows (d) are clamped between plates B, D and plate C, creating a liquid chamber with a capacity of 5 ml. Sealing is facilitated by means of O-rings placed in grooves (e). The samples (b) 1 cm × 1 cm in size are clamped by two small plates (c), onto a stainless steel stage (a). A nozzle (f) allows *in situ* liquid/gas exchange. The heating jacket can be controlled by two heaters (g) while the cooling jacket can be connected to a water circulating bath *via* an inlet (i) and an outlet (h). 19

Figure 2.2. Schematic of the XRR experiment setup with an incident synchrotron X-ray beam reflected from the sample with an incident angle θ_i to the avalanche photodiode detector (APD) that collects the specular reflection. 20

Figure 2.3. A schematic showing an X-ray beam striking a sample with a width of L at angle θ. The incident beam has an intensity of I_0 and beam height of H_0, while the beam that hits on the sample has a height of H. When $H_0 > H$, the beam footprint along the y axis is L_0, the intensity of the reflected beam, I_r, that collected by the detector needs to be corrected as the beam only hits the sample partially. 21

Figure 2.4. a) An illustration of a cross section of a beam whose intensity satisfied a Gaussian profile. a) A z-scan profile (red circles) and its spline fitting (black solid line) are plotted at the top, comparing with the beam intensity profile (black circles) among the z-axis and its fitted Gaussian distribution (blue solid line) at the bottom. 22

Figure 2.5. The headgroup (highlighted in the pink ovals) and hydrocarbon (highlighted in the blue ovals) tail regions of DOPC and DPPC lipids. The PC headgroup is comprised of a phosphocholine group (circled in purple), a glyceryl group and a carbonyl groups (highlighted in the brown shapes). 24

Figure 2.6. Key components of the DLS instrument, which applied a backscatter mode that collected scatterings at 173°. The hydrodynamic size of different type of particles is also shown. 29

Figure 3.1. a) The XPS surveys for the graphene sample measured before (black line) and after (pink line) annealing. b) shows the C 1s photoemission region highlighted in the dashed rectangle in a), and the fittings for the photoemission lines before and after annealing are shown in c) and d), respectively. The fittings suggest the existence of carbon oxides in the sample, including O-C=O and C-OH, with the peak energy values listed in Table S4 in SI-3. After annealing, the amount of the oxides decreased. e) The work function map of graphene annealed at 450 ºC for 1 h, with 2 types of contaminants labelled as **A** and **B**. 40

Figure 3.2. a) An example AFM scale topological image on a 1 μm × 1 μm scale; b) Three line profiles followed the direction of the coloured arrow lines in a), with the grey highlighted areas attributed to the graphene layer; c) An example AFM topographic image on a 5 μm × 5 μm scale, highlighting PMMA residues (*e.g.* **2**, **3**) on a continuous graphene layer with holes (*e.g.* **1**) and defects (*e.g.* **4**) exposing underlying SiO_2; d) the corresponding histogram shows the height distribution of SiO_2, graphene, and the contaminant layer. 41

Figure 3.3. a) The fitted SLD profile of the graphene sample at different temperatures with the corresponding physical model used for the fitting. Here, t_c and t_g are the thickness of the 2 slabs representing the contaminants and graphene, respectively. b) The open circles and solid lines are corresponded to the collected XRR data points and fits on a log scale of graphene plotted against $\boldsymbol{Q}$ at different temperatures (with the curves offset vertically for clarity). The fitting parameters are listed in Table 3.3 and Table 3.2. 43

Figure 3.4 XRR results of the commercially available graphene sample (black circles), fitted as FLG with a contaminant layer on top (black line), as monolayer graphene (blue line), and as FLG without contaminants (pink line), respectively. 43

Figure 4.1. a) Physical model used to fit the XRR curves of graphene in water. b) The experimental (open symbols) and fitted (solid lines) XRR curves plotted as $R\boldsymbol{Q}^4$ vs. $\boldsymbol{Q}$ for graphene in air (circles), in water (triangles), and 24 h-water soaked graphene (squares). The complete fitting parameters are listed in Table S6 in Appendix V). c) The fitted SLD ρ_n of the graphene sample in air (dashed line) and in water (solid line), plotted against z, the distance from the SiO_2 surface, with the SLD variations highlighted in different coloured regions across the interfaces of the graphene sample in air and in water. Each coloured region, with the width representing t_n, represents a modelled layer as defined in a). The contaminant layer on graphene (represented as **Gr**) in air [27] is highlighted in pink, and a diffuse layer is present on the graphene in water. 57

Figure 4.2. a) Example AFM topological images on a 1 μm × 1 μm area indicating graphene defects (1 and 2), PMMA residues (3), and air bubbles (4) on a continuous graphene layer with holes (white circle). b) Plotted line-profiles following the direction of the coloured arrow lines in a). 60

Figure 4.3. a) Example AFM 3D topological images of graphene in air and in water, showing a possible bubble (indicated by an oval) appear after the adding of water; and b) the corresponding histograms of height distributions on the sample surface with the Gaussian peak fittings for the measurements in air (left) and in water (right). 61

Figure 4.4. a) Fitted XRR SLD profiles in water of the un-soaked graphene (red solid line) and soaked graphene (blue dashed line), with the coloured regions representing different layers in the Slab Model used to fit the data. b) The water CA = 84.9° of a bare graphene sample reduced to CA = 55.6° after soaking in Milli-Q for 24 h. The diminishing

of the air bubble layer, the hydration of the SiO_2 substrate, and the formation of the ion adsorbed layer upon soaking are schematically illustrated in (c).....65

Figure 4.5. a) The experimental (open circles) and fitted (solid lines) XRR curves (offset vertically for clarity) of water-soaked graphene in PBS at different temperatures, with the fitting parameters (t_n, ρ_n and $R_{a,n}$) tabulated in Table S6. The fits show that the graphene thickness t_g remained at ~ 4.2 Å at all temperatures; while its SLD was relatively constant at ρ_g ~ 15 × 10^{-6} Å^{-2} at lower temperatures, it increased to ρ_g = 17.6 × 10^{-6} Å^{-2} at 60 °C. Similarly, the SLD and thickness of the ion adsorbed layer ρ_a and t_a increased at 60 °C, and the increment remained after cooling back to RT as shown in b). The SLD profiles of graphene samples at 25 °C and 60 °C are shown in (c) and (d), respectively, which show that the thickness of the silanol layer also increased at 60 °C, with the interface between graphene and the ion adsorbed layer becoming smoother. 66

Figure 5.1. 4 models of the lipid adsorption morphologies on graphene that have been reported. Monolayers (a) and trilayers (with a tilted monolayer sandwiched between graphene and the lipid bilayer) (c) were observed to form on hydrophobic graphene, whereas bilayers were found to form with a trapped water layer sandwiched between the substrate and the membrane. Intact liposomes (d) were also detected in the primary stage after deposition.....75

Figure 5.2. Illustration of the preparation procedure of the liposomes. 76

Figure 5.3. Schematic of the XRR setup with an incident synchrotron X-ray beam hitting the supported lipid bilayer (SLB), which generates specular reflections from the interfaces of the measured sample to the APD, where the data can be collected. 78

Figure 5.4. XRR data points (open markers) and the fittings (solid lines) of graphene incubated in DOPC suspensions in water (a) or in PBS (b), in comparison to the corresponding XRR curves of graphene in aqueous medias, plotted on $\boldsymbol{RQ}^4$ against $\boldsymbol{Q}$ (with curves offset vertically for clarity). The fitted XRR curves of DOPC suspensions in PBS on un-soaked graphene and soaked graphene are shown in (c) and (d), respectively, with their SLD profiles shown as insets. On the SLD profiles, the modelled slabs are highlighted with different colours across the interfaces of the DOPC layer on graphene (Gr), with the DOPC structure divided to two regions: the headgroup (H) that possesses higher electron density and the hydrocarbon tail (T). The complete fitting parameters of the curves are listed in Table S7 in Appendix V.....79

Figure 5.5. XRR data points (open markers) and the fittings (solid lines) of DOPC (a) and DPPC (b) liposomes suspended in PBS incubating on the un-soaked graphene at 25 °C, 40 °C, and 60 °C, plotted as $\boldsymbol{RQ}^4$ against $\boldsymbol{Q}$. The XRR curves collected at different temperatures were offset vertically for clarity. The fitted SLD profiles (*cf.* Figure 5.6) of the XRR curves in (a) and (b) suggest that both DOPC and DPPC liposomes have fused into monolayer membrane on un-soaked graphene. c) and d) illustrate the graphene surfaces before and after the vesicle fusion, respectively. 86

Figure 5.6. SLD profiles of DOPC (a) and DPPC (b) samples on un-soaked graphene collected at diffeent temperatures with the inset cartoons of lipid showing the possible morphologies. The thickness (categories), t, rougness (error bars), R_a, and the coverage (markers and lines), ϕ, of each slabs are compared in (c). 89

Figure 5.7. DPPC bilayer formed on the soaked graphene *via* vesicle fusion (b) and its thinning (c) and extending (d) behaviour upon heating and cooling suggested by fittings (solid lines) of the XRR results (open markers) shown in (a). The XRR curves were offset vertically for clarity. The DPPC bilayer has been investigated in PBS at 25 °C, 40 °C, 60 °C, after 3 h incubating at 60 °C, cooling back to 25 °C, and rinsing with PBS. 90

Figure 5.8. Illustration of the DPPC bilayer structure as insets in (a) and (b) at different temperatures suggested by their fitted SLD profiles of the XRR data (*cf.* Figure 5.7a). The thickness (categories), t, rougness (error bars), R_a, and the coverage (markers and lines), ϕ, of the DPPC proximal and distal leaflets are compared in (c). The interfacial roughness between the inner and outer layer hydrocarbon tails remained <0.8 Å, except for the measurements at 60 °C and at 25 °C after cooling, suggesting the two chains exhibits different states of phase during the two measurements. 91

Figure 5.9. Comparison of the thickness t_n (categories) with the corresponding roughness shown as error bars and the coverage ϕ_n (markers and lines) between the graphene layer (g) and the ion adsorbed layer (denoted as a) of the bare graphene (denoted as g) and the lipid adsorbed graphene (denoted as l). 94

Figure 6.1 XRR curves of the possible LPS-Ra adsorption on graphene, in water and in the presence of 10 mM $CaCl_2$. 105

Figure S1. a) The XPS surveys for a CVD graphene sample measured at RT (black), after annealed at 200 °C (blue), after further annealed at 400 °C (yellow) and at 450 °C (red). b) shows the C 1s photoemission region highlighted in the dashed rectangle in a).....109

Figure S2. The work function maps of graphene samples annealed at 400 ºC for 1 h (a) and at 450 ºC for a further 20 min. Additional annealing reduced PMMA contaminants on the graphene surface.....110

Figure S3. a) AFM topological image on a 5 μm × 5 μm scale. The squares (1-5) are the selected area for the histogram analysis of the graphene sample. The highlighted regions in b) and c) attributed to the silica substrate and contaminants (graphene multilayers and PMMA) from the analysi``s, respectively. 112

Figure S4. A contact angle measurement of graphene, the droplet is water. 112

Figure S5. WCA of graphene, before and after soaking. 114

Figure S6. The SLD profiles of soaked graphene in PBS at 25 °C (a), 40 °C (b), 60 °C (c), and after cooling back to 25 °C (d). The modelled slabs are highlighted in boxes, the height and width of each box represents the represents the ρ_n, and the t_n of the n^{th} layer, respectively.....119

Figure S7. a) XRR curves (circles) of the drop-cast DOPC multilayer on graphene at different temperatures, in comparison to that of bare graphene (triangle), the reflectivity curves are offset for better comparison. Although the presence of Bragg peaks indicated periodic structures, the broad peak width and split peaks imply highly disordered structures. b) An example of peak fitting, showing the 1st order (n = 1) Bragg peak of the measurement at 25 °C highlighted in the rectangle in (a): the simulated Gaussian peaks (blue lines, i = 1, 2, 3) composing the fitting (red line) of the example Bragg peak (circles), and the base line (green line) fitted with a cubic spline of the vicinity. c) An illustration of the DOPC multilayer on graphene, comprised by domains (lipid bilayer) with a spacing of d and a coherence length of L_a (the mean domain size perpendicular to the substrate). 127

Figure S8. The calculated d (a and b) and L_a (c and d) of the DOPC multilayers on graphene at 25 °C (solid circles), 40 °C (solid triangles), 60 °C (solid diamonds), cooling to 40 °C (triangles), and cooling to 25 °C (circles), plotted against the diffraction order

(*n*) on the same scale for comparison. Results obtained from different peak position were represented with different marker size, to access full results of the data, see Table S7 in SI-3. The large error bars can be attributed to the limited number of data points for fitting the resolved peaks. 130

Chapter 1

Introduction

The structure of graphene is related to its physical properties, thus crucial to its integration in composite materials and its bioanalytic applications. In this project, we have performed in situ structural characterisation of graphene in air, in water, and after it is coated with lipid membranes via vesicle fusion. This chapter gives a brief review of the structural characterisation of graphene and adsorption of molecules on graphene, which highlights the importance of understanding the structure of graphene under such conditions. An introduction to the main characterisation technique applied in this study, X-ray reflectivity, is also presented.

1.1 Project Motivations

Since the first exfoliation of graphene [1, 2], it has attracted intense interest in both scientific research and industrial applications as a promising 2D material. Over the last decade, one of the most developed applications of graphene and its derivatives is sensing the adsorption of molecules in the adjacent environments. Among which, bioanalytic applications of graphene have attracted wide attention, yet the biocompatibility issue of graphene restricted its actual application in this field. To solve this problem, one method is to functionalise the graphene surface with biomolecules, thus cutting down the probability of direct contact between graphene and the surrounding biomolecules. For this purpose, lipid, the fundamental component of the cell membrane, has been utilised in the graphene surface modification [3-5]. However, there is controversy as to whether lipids form monolayer or bilayer membranes on graphene, since both morphologies have been observed previously. In addition, it has been reported that the physical properties of graphene are related to the structure of itself [6, 7], the adsorbed molecules [8, 9], and the underlying substrate [10, 11]. Therefore, the structural information of graphene that has been coated with lipids is important for the development of biofunctionalised graphene devices.

This project aims to apply synchrotron X-ray reflectivity (XRR) to probe the surface structures of lipid membranes adsorbed on graphene and the buried graphene surfaces. The adsorption behaviour of liposomes on the commercially available graphene supported by Si/SiO_2 (with a 300 nm SiO_2 layers) and their response to changes of the

surrounding environments (*e.g.* temperature and the adding of electrolytes) have been investigated. Despite that XRR is a vigorous technique in structural characterisation, it has rarely been used on graphene and the related systems. In this study, the graphene substrates have been investigated at the air/solid and the liquid/solid interfaces, using XRR and complimentary techniques such as atomic force microscopy (AFM), X-ray photoelectron spectroscopy (XPS), and photoemission electron microscopy (PEEM), in order to compare with the lipid adsorbed graphene, thus understanding the interaction between graphene and lipids thoroughly.

1.2 Brief Introduction to Graphene

Despite that graphene is considered as a novel material, it has been studied theoretically since 1947 (by then it was referred as a single layer graphite) [12]. It was only until 2004 that the first piece of graphene has been produced successfully in lab by Geim and Novoselov [1], who have also revealed the extraordinary electronic properties of graphene experimentally [13, 14]. The sp^2 hybrid orbitals alongside the one-atomically thin structure provide graphene unusual electronic properties such as ultrahigh carrier mobility, massless Dirac fermions, and half-integer quantum Hall effect [13-15]. These unique 2D electronic properties have since stimulated numerous studies aiming to develop its usage in applications such as supercapacitors, batteries, interconnects, transistors, phonon detectors, and especially sensors in various fields [2, 16]. For instance, the surface charging of graphene due to ion adsorption has been exploited to monitor pH changes [17] and lipid membrane disruptions [18].

1.2.1 Chemical vapour deposition of graphene

Concurrently, the advances in the applications of graphene have stimulated the production and modification of graphene and its derivatives. The first method used by Geim and Novoselov to create graphene is known as mechanical cleavage method [1]. It can generate highly ordered graphene planes, but it is time-consuming, and the planes can be fragile nonetheless [16]. One of the most promising methods for producing high quality graphene on an industrial scale is chemical vapour deposition (CVD), which involves depositing graphitic layers atop another crystalline substrate, such as SiC [19], Ni [20], and Cu [21]. Graphene prepared by the CVD method has been reported to exhibit an electronic spectrum that can be described by a 2D analogue of the Dirac equation, similar to that of free-standing graphene [16]. Among all the substrates, Cu attracted particular

attention. As confirmed by Raman spectroscopy, graphene deposited on Cu by the CVD method could yield over 93% coverage (with the rest consisting of 2-3 layer graphene), thanks to its weak interaction with graphene which benefits 2D crystal growth, thereby generating "monolayer" graphene on the Cu surface [22]. However, the limited choices of substrate for graphene deposition launched a necessity of transferring graphene to an arbitrary substrate [23, 24]. There are mainly two types of techniques to transfer graphene, namely dry transfer and wet transfer. In the dry transfer method, the graphene layer would be peeled off and directly placed onto the targeted substrate, which could easily result in structural defects that are undesirable for further applications [23, 25, 26]. In the wet transfer method, usually, a polymethylmethacrylate (PMMA) layer would be deposited atop graphene *via* spin coating as a support before the original substrate is removed by chemical etching, and then the graphene would be transferred onto a desired substrate, such as SiO_2 [23-26]. The wet transfer method also has disadvantages, it has been reported that this procedure could leave residues of PMMA and etching agents [23-26], which can affect the electronic properties of graphene. Treatments to clean the CVD graphene surface has been developed, including annealing at high temperature in ultra-high vacuum conditions [27], and applying other polymers that are easier to remove to assist PMMA (*e.g.* polyvinylacetate [28] and poly(bisphenol A carbonate) [29]).

1.2.2 Influence of structure on graphene properties

Graphene is a two-dimensional monolayer of carbon with atoms arranged in a honeycomb lattice [30]. Previous studies have shown that the physical properties of graphene materials are determined by its structure, specifically the thickness and the defects or contaminants. For example, the thermal conductivity of graphene materials increases with the layer number, with monolayer, double-layer, and *few layer graphene* (FLG) (3-10 layers) showing different 2D electronic properties [6, 7]; the transport properties in epitaxial graphene are influenced by its sp^2 aromatic lattice structure, which is in turn affected by its substrate and growth conditions [10, 11]; and the presence of ripples and wrinkles on graphene is expected to have a negative effect on its electronic properties [22]. Thus, a precise determination of the thickness and morphology of graphene samples under different conditions is important.

1.3 Interaction between Biomolecules and Graphene

Because of the superb electronic properties and the inert chemical nature of graphene, researches have been carried out to develop it for the use in bioelectronics [16, 31]. Furthermore, the interaction between graphene and different biomolecules, such as such as DNA, nucleic acids, proteins, peptides, and lipids has been reported [8, 31], showing the affinity of graphene to biomolecules. The driving force that can trigger the assembly of biomolecules on pristine graphene has been attributed to the π–π stacking and hydrophobic force. Other forces such as hydrogen bonding, electrostatic interaction, and covalent binding can also contribute to the adsorption of biomolecules on functionalised graphene derivatives [8, 31]. The combination of the properties discussed above make graphene a potential material to be used in biomolecule detecting, drug delivery, tissue engineering, and so on [31].

Despite that graphene is chemically inert, it has been reported to exhibit mild cytotoxicity [32, 33]. The destructive behaviours of cell membranes initiated by the nanosheet graphene insertion and the extraction of lipids has been demonstrated both theoretically and experimentally [34]. The rupture of cells on a graphene surface has been attributed to the membrane stress generated from direct physical contacts with the sharp structures on the graphene surface, and the cellular oxidization stress that leads to the oxidation of key cell components, such as lipids and proteins, thereby disrupting a specific microbial process [33, 35, 36]. In order to increase the biocompatibility issue of graphene, one of the feasible solutions is surface modification, which can efficiently reduce the undesired contact of graphene to the biomolecules. Therefore, understanding the interaction between graphene and biomolecules becomes important to further researches on improving the safety of graphene related systems.

The interaction between graphene and biomolecules had been investigated by various techniques [4, 37-39]. AFM [5, 37, 40, 41] and quartz crystal microbalance with dissipation monitoring technique [4, 37, 38], for instance, are among the most commonly used methods to monitor the physical adsorption of biomolecules on solid substrates, including the deposition of lipids on graphene [4, 5, 37]. The quality of the adsorbed biomolecule membranes on graphene, such as the homogeneity and the coverage can be determined by AFM, and the internal reflection fluorescence correlation spectroscopy (ITIR-FCS) [5]. However, these techniques focus on the characterisation of the deposited

biomolecules, lacking the *in situ* structural information of the buried graphene substrate, which is important to the integration of graphene in electronic devices as mentioned earlier in section 1.2.2.

1.4 Brief Introduction to X-ray Reflectivity

1.4.1 X-ray

X-rays were discovered by Wilhelm Conrad Röntgen in 1985. They are a type of electromagnetic radiation, that exhibit a wavelength, λ, in the region of 0.1 – 100 Å. The numerical relation between λ and the photon energy $\mathcal{E}$ can be expressed as:

$$\lambda\,[\text{Å}] = \frac{hc}{eE} = \frac{hc}{\mathcal{E}} = \frac{12.398\ [\text{keV}\cdot\text{Å}]}{\mathcal{E}\ [\text{keV}]}, \qquad \text{Equation 0.1}$$

where $e = 1.602\times10^{19}$ C represents the electronic charge, $c = 2.998\times10^{8}$ m s^{-1} the speed of light and $h = 2\pi\hbar = 6.626\times10^{-34}$ m^2 kg s^{-1} the Planck's constant. From Equation 0.1, it is straightforward that X-rays have an energy range of 0.1-120 keV. The energy of an X-ray is relevant to its capability to penetrate a material. When $\mathcal{E}$ < 10 keV, the X-radiation (known as soft X-rays) exhibits a lower penetrating ability (~ 10 nm) and is commonly applied to investigate the electron bindings of atoms or bond resonance energies in molecular structures near the studied surface (*e.g.* XPS). When $\mathcal{E}$ >10 keV, the X-rays (known as hard X-rays) can penetrate through materials and interact with electrons. The interactions between the hard X-rays and the atomic electrons are the basis of many X-ray analysis techniques, such as XRR and XRD.

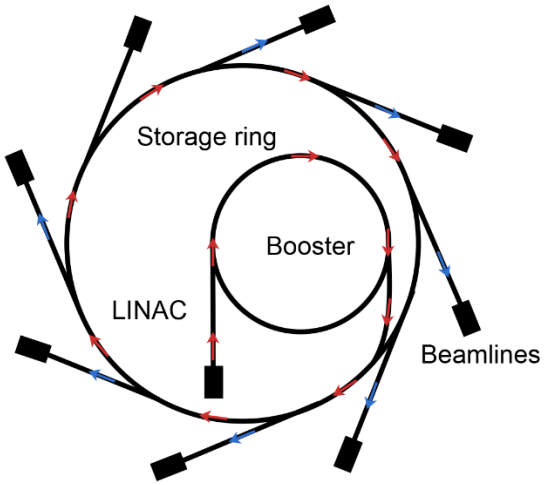

Figure 0.1. Illustration of a typical synchrotron with the arrays showing the direction of the moving electron bunches [42].

Since the discovery of X-rays, the rapid development of the beam sources (the 3rd generation synchrotron source) provides researchers with X-rays that are ~ 10^{12} times brighter than the early lab-built ones. Figure 0.1 illustrates a typical beamline at a 3rd generation X-ray synchrotron source. Electrons emitted from the electron gun of a metal electrode are accelerated up to a relativistic speed by a linear accelerator (LINAC) and then injected into a booster ring, which increases its electron energy. These electrons are injected into a storage ring and simultaneously serve multiple beamlines for scientific applications. In the storage ring, radiation can be produced in the bending magnet part as well as the insertion device, such as wigglers or undulators, due to the angular momentum changes of the electrons [42, 43].

1.4.2 X-ray scattering

The scattering event of X-rays with a single electron is conventionally described as the interaction between the electric field of the incident X-rays and the targeted electrons, which then generates the scattered wave. Theoretically, the scattering of an X-ray is necessarily *elastic*, also called as *Thomson* scattering, which means the wavelength of the incident and the scattered beams are of the same value. However, in a quantum mechanical description, energy of the incident beam may be adsorbed by and transferred to the electron during a scattering, which is known as *inelastic* or *Compton* scattering. In this case, the incident beam consists of a momentum of $\hbar\boldsymbol{k}$ and an energy of $\hbar\omega$, and the momentum transfer from an X-ray to an electron is represented by the wavevector transfer or scattering vector $\boldsymbol{Q}$, usually expressed in units of $Å^{-1}$, and can be given as,

$$\hbar\boldsymbol{Q} = \hbar\boldsymbol{k}_{\mathbf{f}} - \hbar\boldsymbol{k}_{\mathbf{i}} , \qquad \text{Equation 0.2}$$

where $\boldsymbol{k}_{\mathbf{i}}$ and $\boldsymbol{k}_{\mathbf{f}}$ are the incident and reflected momentum of the photon, respectively.

For materials with periodical structure, such as a crystal, which is composed of a repeating lattice structure, Bragg's law can be applied to describe the constructive interference waves, when the phase shift from the lattice is proportional to 2π, the relation between the lattice spacing d and the incident beam wavelength λ can be given as,

$$2d\,[Å]\,sin\theta = n\lambda\,[Å] , \qquad \text{Equation 0.3}$$

where n is a positive integer, θ is the incident angle of beam.

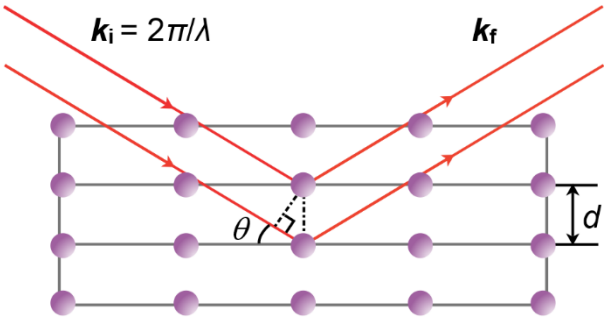

Figure 0.2. The Bragg scattering geometry. $\boldsymbol{k}_i$, $\boldsymbol{k}_f$, θ, and d denote the wavevector of the incident and reflected beams, the angle of incidence, and the lattice spacing, respectively.

1.4.3 Specular reflection

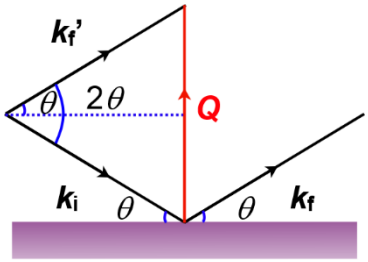

Figure 0.3. Illustration of a reflection from an interface. $\boldsymbol{k}_i$ and $\boldsymbol{k}_f$ represent the wavevectors of the beam of incidence and reflection, respectively. $\boldsymbol{Q}$ denotes the wavevector transfer.

The most simplified model for beam reflection is a specular reflection from an ideal surface (*i.e.* flat and smooth), in which the reflection is *elastic*, hence no loss of energy. As shown schematically in Figure 0.3, the wavevector transfer, $\boldsymbol{Q}$, in this case, can be expressed as

$$\boldsymbol{Q} = \boldsymbol{k}_f - \boldsymbol{k}_i \,, \qquad \text{Equation 0.4}$$

where the momentum of the incident wave, $\boldsymbol{k}_i$, equals to that of the reflected wave, $\boldsymbol{k}_f$, $|\boldsymbol{k}_i| = |\boldsymbol{k}_i| = |\boldsymbol{k}|$, this yields a geometrical relationship between the Q and k values, that is

$$Q\,[\text{Å}^{-1}] = 2k\,[\text{Å}^{-1}]\,sin\theta \,, \qquad \text{Equation 0.5}$$

where θ is the angle of incidence, with $k = 2\pi/\lambda$,

$$Q\,[\text{Å}^{-1}] = \frac{4\pi sin\theta}{\lambda\,[\text{Å}]} \,. \qquad \text{Equation 0.6}$$

If we combine Equation 0.6 with the Bragg's law, the relation between the lattice spacing *d* and *Q* can be acquired

$$d\,[\text{Å}] = \frac{2\pi}{Q\,[\text{Å}^{-1}]}\,. \qquad \text{Equation 0.7}$$

This relation can be used to calculate the *d* of ordered periodical multilayers.

1.4.4 Reflection and refraction

The elementary unit for an X-ray to interact with is an electron, whose scattering length can be used to express the ability to scatter the X-ray. To describe the scattering length of more complex units, the classical electron radius or *Thomson* scattering length, $r_{0,}$ needs to be introduced,

$$r_0 = \left(\frac{e^2}{4\pi\epsilon_0 mc^2}\right) = 2.82 \times 10^{-5}\ \text{Å}\,, \qquad \text{Equation 0.8}$$

where ϵ_0 =8.854 × 10^{-12} Å s V^{-1} m^{-1} is the permittivity of vacuum, m = 9.109 × 10^{-31} kg is the mass of an electron.

The interaction between X-rays and the interfaces of a material can be characterised by its refractive index, *n*, given by

$$n = 1 - \delta + i\beta, \qquad \text{Equation 0.9}$$

where δ and β denote the dispersion and the adsorption, respectively, and can be defined as

$$\delta = \frac{\lambda^2}{4\pi}\rho_{\text{r}} \text{ and } \beta = \frac{\lambda^2}{4\pi}\rho_{\text{m}}\,, \qquad \text{Equation 0.10}$$

where ρ_{r} and ρ_{m} are the real and imaginary parts of the scattering length density of the material, respectively, which is described in detail in section 1.4.6.

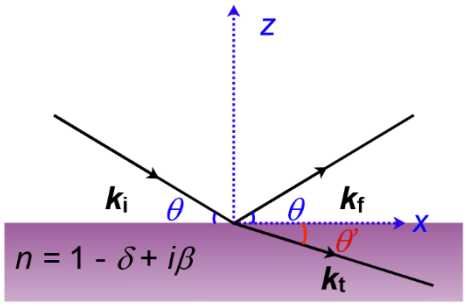

Figure 0.4 Reflection and refraction of a beam from an ideal surface with a refractive index of n, $\boldsymbol{k}_i$, $\boldsymbol{k}_f$, and $\boldsymbol{k}_t$ are the wavevectors of the incident, reflected, and transmitted beams, respectively. θ represents the angle of incidence. x and z are the parallel and perpendicular axis.

When the incident angle is smaller than the critical angle, θ_c, the X-ray can be totally reflected from an interface, this phenomenon is known as a total reflection, where the adsorption can be neglected. The wavevector corresponding to θ_c can be given as

$$Q\,[\text{Å}^{-1}] = \frac{4\pi sin\theta_c}{\lambda\,[\text{Å}]}\,. \qquad \text{Equation 0.11}$$

And by applying Snell's law and small angle approximation, the critical angle can be expressed as

$$n = 1 - \delta = cos\theta_c \approx 1 - \frac{\theta_c^2}{2}\,, \qquad \text{Equation 0.12}$$

which yields

$$\theta_c \approx \sqrt{2\delta} = \sqrt{\frac{\lambda^2}{4\pi}\rho_r}\,. \qquad \text{Equation 0.13}$$

It can be seen that the critical angle of a specific reflection is related to the material hit by the X-rays.

1.4.5 X-ray reflection from layered interfaces

When the incident angle is above the θ_c, a fraction of the X-rays will transmit into the media, and if the media is composed of several layered materials with different reflective index $n_j = 1 - \delta_j + i\beta_j$, thickness t_j, and roughness $R_{a,j}$, it can lead to reflections from all the interfaces, as shown in Figure 0.5. The magnitude of the wavevector that of the X-

rays propagating through the j^{th} layer, k_j can be given as $k_j = n_j k$. As the x component, $k_{x,j}$ of all the k_j is constant, the z component, $k_{z,j}$, can be deduced trigonometrically as

$$k_{z,j}^2 = (n_j k)^2 - k_x^2 = (1 - \delta + i\beta)^2 k^2 - k_x^2 \approx k_z^2 - 2\delta_j k^2 + i2\beta_j k^2. \quad \text{Equation 0.14}$$

The respective wavevector transfer Q_j value can then be expressed as

$$Q_j = 2k_j sin\theta_j = 2k_{z,j} = \sqrt{Q^2 - 8\delta_j k^2 + i8\beta_j k^2}\,. \quad \text{Equation 0.15}$$

If neglecting multiple reflections, the reflectivity $r_{j,j+1}$ can be obtained by the Fresnel relationship

$$r_{j,j+1} = \frac{Q_j - Q_{j+1}}{Q_j + Q_{j+1}}\,. \quad \text{Equation 0.16}$$

If roughness (R_a) is taken into account, as described by Nevot and Croce [44], the reflectivity can can be described as:

$$r'_{j,j+1} = r_{j,j+1}\sigma_j\,, \quad \text{Equation 0.17}$$

And

$$\sigma_j = e^{-\frac{1}{2}Q_j Q_{j+1} R_{a_{j,j+1}}^2}\,. \quad \text{Equation 0.18}$$

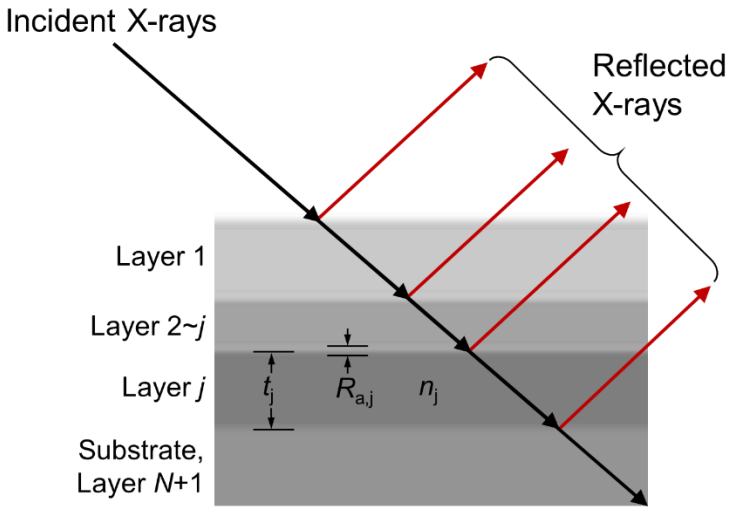

Figure 0.5 Reflection of X-rays from an interface region modelled as a series of uniform layers. The figure is reproduced from reference [45].

Based on the Fresnel relationship, the reflectivity for a multilayer system can then be deduced. From the very bottom layer, N, above the substrate, N+1, of the considered system as shown in Figure 0.5, the reflectivity can be given as

$$r'_{N,N+1} = \frac{Q_N - Q_{N+1}}{Q_N + Q_{N+1}} \sigma_N \,. \qquad \text{Equation 0.19}$$

In this relationship, no multiple reflections are considered, since the substrate is assumed to be infinite. However, in the calculation of the reflectivity from the interface between layer N and layer N - 1, the contribution of multiple reflection will need to be taken into account, which gives

$$r_{N-1,N} = \frac{r'_{N-1,N} - r'_{N,N+1} p_N^2}{1 + r'_{N-1,N} r'_{N,N+1} p_N^2} \,, \qquad \text{Equation 0.20}$$

where the phase factor $p_N^2 = e^{iQ_N d_N}$. Similarly, if needed, the successive layers can be built recursively as

$$r_{N-2,N-1} = \frac{r'_{N-2,N-1} - r_{N-1,N} p_{N-1}^2}{1 + r'_{N-2,N-1} r_{N-1,N} p_{N-1}^2} \,, \qquad \text{Equation 0.21}$$

until the top interface, where N = 0. Finally, the overall reflectivity of the examined system can be calculated from the absolute square of the reflectivity amplitude

$$\boldsymbol{R} = |r|^2 \,. \qquad \text{Equation 0.22}$$

This approximation is referred to the Parratt's exact recursive method [43], which allows the intensity of the reflectivity to be plotted against the wavevector $\boldsymbol{Q}$. An example of the XRR curve plotted as log$R$ vs. $\boldsymbol{Q}$ is shown in Figure 0.6, illustrating the interference oscillations, known as Kiessig fringes, which can be used to estimate the layer thickness d, from the curve.

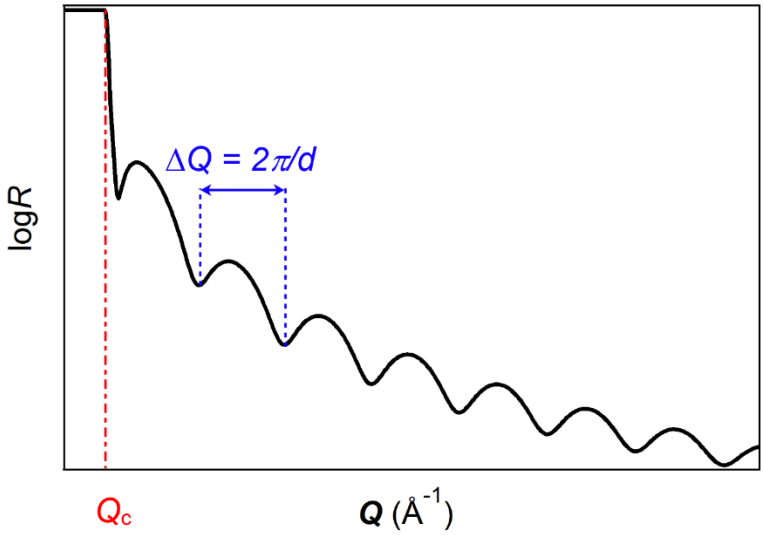

Figure 0.6 Example reflectivity curve with intensity plotted as log$R$ against the wavevector transfer $\boldsymbol{Q}$. Q_c is the respective wavevector of the critical angle θ_c, and the layer thickness d can be estimated from the spacing of the Kiessig fringes (the interference oscillations), ΔQ.

1.4.6 Scattering length density

XRR can be used to detect the interfacial structures of the sample comprised by materials with different scattering length densities (SLD, ρ). And the analysis of the obtained X-ray reflectivity data will need the ρ of each layer to do the fittings. SLD is defined as the scattering length of the electrons in the basic unit, such as unit cell in a crystal, of the material per unit volume, with a unit of Å^{-2}. It has a real part ρ_r, which is related to δ, representing the dispersion ability and an imaginary part ρ_m, which is related to β, representing the absorption of the X-rays by the material (*cf.* Equation 0.10), ρ can be given as

$$\rho = \rho_r + i\rho_m \qquad \text{Equation 0.23}$$

and

$$\rho_r = \frac{r_0 f_1}{V} = r_0 f_1 \rho_a \qquad \text{Equation 0.24}$$

$$\rho_m = \frac{r_0 f_2}{V} = r_0 f_2 \rho_a \qquad \text{Equation 0.25}$$

where f_1 and f_2 are the real and imaginary parts of the atomic scattering factor of the molecule (the values of f_1 and f_2 of each element at different wavelength can be found in literature [46]), V is the molecular volume or unit cell volume. Considering molecules composed by multiple atoms, the scattering length density can be described by the sum of the atomic scattering length of each atom in the material:

$$\rho = \frac{r_0 \sum_{i=1}^{n} N_i f_1(i)}{V} + i\frac{r_0 \sum_{i=1}^{n} N_i f_2(i)}{V} \qquad \text{Equation 0.26}$$

where N_i is the number of the i element per unit volume, $f_1(i)$ and $f_2(i)$ are the atomic scattering factors of the i element in the molecule. For most of the molecules, the molecular volume of them can be simply calculated from the atomic density ρ_a

$$V = \frac{1}{\rho_a} \qquad \text{Equation 0.27}$$

and

$$\rho_a = \frac{N_A}{M}\rho_m \qquad \text{Equation 0.28}$$

where N_A=6.022 × 10^{23} is the Avogadro constant, M is the molecular mass and ρ_m is the mass density of the molecule.

1.5 Thesis Outline

The main purpose of this work is to probe the structure of the graphene surface in air and in aqueous medias as well as that of the lipid membrane prepared by vesicle fusion method on graphene.

In Chapter 2, the theoretical background of the techniques that have been used in this project is given, mainly focusing on the introduction to the XRR technique. The synchrotron beam source, the experimental setup, and the data analysis of XRR are described in detail.

Chapter 3 to 5 present the results of this project. In Chapter 3, the structure of the commercially available graphene samples on Si/SiO_2 studied by XRR, XPS, PEEM and AFM, and a tentative temperature responsive thickness expansion of graphene shown by XRR are reported. In Chapter 4, the graphene-water interface has been studied by

synchrotron XRR before and after soaking the sample in Milli-Q® water for 24 h, complemented by AFM imaging and contact angle measurements. The influences of temperature and the presence of phosphate buffered saline (PBS) on the graphene surface structure are also discussed. Finally, in Chapter 5, the interaction between liposomes and graphene surface (before and after soaking) in water and in PBS and at different temperatures is investigated.

The conclusion and possible future work of this thesis is given in Chapter 6.

Reference

1. Novoselov, K.S., et al., *Electric field effect in atomically thin carbon films.* Science, 2004. **306**(5696): p. 666-669.
2. Novoselov, K.S., et al., *A roadmap for graphene.* Nature, 2012. **490**(7419): p. 192-200.
3. Pinto, A.M., Goncalves, I.C., and Magalhaes, F.D., *Graphene-based materials biocompatibility: a review.* Colloids and Surfaces B-Biointerfaces, 2013. **111**: p. 188-202.
4. Tabaei, S.R., et al., *Controlling the formation of phospholipid monolayer, bilayer, and intact vesicle layer on graphene.* Acs Applied Materials & Interfaces, 2016. **8**(18): p. 11875-11880.
5. Ang, P.K., et al., *A bioelectronic platform using a graphene-lipid bilayer interface.* Acs Nano, 2010. **4**(12): p. 7387-7394.
6. Xu, M.S., et al., *Auger electron spectroscopy: a rational method for determining thickness of graphene films.* Acs Nano, 2010. **4**(5): p. 2937-2945.
7. Jang, W.Y., et al., *Thickness-dependent thermal conductivity of encased graphene and ultrathin graphite.* Nano Letters, 2010. **10**(10): p. 3909-3913.
8. Wang, Y., et al., *Graphene and graphene oxide: biofunctionalization and applications in biotechnology.* Trends in Biotechnology, 2011. **29**(5): p. 205-212.
9. Gurunathan, S. and Kim, J.H., *Synthesis, toxicity, biocompatibility, and biomedical applications of graphene and graphene-related materials.* International Journal of Nanomedicine, 2016. **11**: p. 1927-1945.
10. Rutter, G.M., et al., *Scattering and interference in epitaxial graphene.* Science, 2007. **317**(5835): p. 219-222.
11. Aitken, Z.H. and Huang, R., *Effects of mismatch strain and substrate surface corrugation on morphology of supported monolayer graphene.* Journal of Applied Physics, 2010. **107**(12): p. 123531.
12. Wallace, P.R., *The band theory of graphite.* Physical Review, 1947. **71**(9): p. 622-634.

13. Novoselov, K.S., et al., *Two-dimensional gas of massless Dirac fermions in graphene.* Nature, 2005. **438**(7065): p. 197-200.

14. Geim, A.K. and Novoselov, K.S., *The rise of graphene.* Nature Materials, 2007. **6**(3): p. 183-191.

15. Zhang, Y.B., et al., *Experimental observation of the quantum Hall effect and Berry's phase in graphene.* Nature, 2005. **438**(7065): p. 201-204.

16. Geim, A.K., *Graphene: status and prospects.* Science, 2009. **324**(5934): p. 1530-1534.

17. Ang, P.K., et al., *Solution-gated epitaxial graphene as pH sensor.* Journal of the American Chemical Society, 2008. **130**(44): p. 14392-14393.

18. Ang, P.K., et al., *A bioelectronic platform using a graphene-lipid bilayer interface.* Acs Nano, 2010. **4**(12): p. 7387-7394.

19. Wang, D.C. and Zhang, Y.M., *Spectroscopic and scanning probe analysis on large-area epitaxial graphene grown under pressure of 4 mbar on 4H-SiC (0001) substratesl.* Chinese Physics B, 2014. **23**(7): p. 10893-10900.

20. Kadowaki, R., et al., *PEEM and micro PES study of graphene growth on Ni(110) substrate.* E-Journal of Surface Science and Nanotechnology, 2015. **13**: p. 347-351.

21. Liu, W., et al., *Synthesis of high-quality monolayer and bilayer graphene on copper using chemical vapor deposition.* Carbon, 2011. **49**(13): p. 4122-4130.

22. Mattevi, C., Kim, H., and Chhowalla, M., *A review of chemical vapour deposition of graphene on copper.* Journal of Materials Chemistry, 2011. **21**(10): p. 3324-3334.

23. Suk, J.W., et al., *Transfer of CVD-grown monolayer graphene onto arbitrary substrates.* Acs Nano, 2011. **5**(9): p. 6916-6924.

24. Li, X.S., et al., *Transfer of large-area graphene films for high-performance transparent conductive electrodes.* Nano Letters, 2009. **9**(12): p. 4359-4363.

25. Unarunotai, S., et al., *Transfer of graphene layers grown on SiC wafers to other substrates and their integration into field effect transistors.* Applied Physics Letters, 2009. **95**(20): p. 202101.

26. Caldwell, J.D., et al., *Technique for the dry transfer of epitaxial graphene onto arbitrary substrates.* Acs Nano, 2010. **4**(2): p. 1108-1114.

27. Lin, Y.C., et al., *Graphene annealing: how clean can it be?* Nano Letters, 2012. **12**(1): p. 414-419.

28. Ngoc, H.V., et al., *PMMA-etching-free transfer of wafer-scale chemical vapor deposition two-dimensional atomic crystal by a water soluble polyvinyl alcohol polymer method.* Scientific Reports, 2016. **6**: p. 33096.

29. Lin, Y.C., et al., *Clean transfer of graphene for isolation and suspension.* Acs Nano, 2011. **5**(3): p. 2362-2368.

30. Singh, V., et al., *Graphene based materials: past, present and future.* Progress in Materials Science, 2011. **56**(8): p. 1178-1271.

31. Li, D.P., et al., *When biomolecules meet graphene: from molecular level interactions to material design and applications.* Nanoscale, 2016. **8**(47): p. 19491-19509.

32. Akhavan, O. and Ghaderi, E., *Toxicity of graphene and graphene oxide nanowalls against bacteria.* Acs Nano, 2010. **4**(10): p. 5731-5736.

33. Hegab, H.M., et al., *The controversial antibacterial activity of graphene-based materials.* Carbon, 2016. **105**: p. 362-376.

34. Tu, Y.S., et al., *Destructive extraction of phospholipids from Escherichia coli membranes by graphene nanosheets.* Nature Nanotechnology, 2013. **8**(8): p. 594-601.

35. Liu, S.B., et al., *Antibacterial activity of graphite, graphite oxide, graphene oxide, and reduced graphene oxide: membrane and oxidative stress.* Acs Nano, 2011. **5**(9): p. 6971-6980.

36. Sanchez, V.C., et al., *Biological interactions of graphene-family nanomaterials: an interdisciplinary review.* Chemical Research in Toxicology, 2012. **25**(1): p. 15-34.

37. Frost, R., et al., *Graphene oxide and lipid membranes: interactions and nanocomposite structures.* Nano Letters, 2012. **12**(7): p. 3356-3362.

38. Melendrez, D., et al., *Adsorption and binding dynamics of graphene-supported phospholipid membranes using the QCM-D technique.* Nanoscale, 2018. **10**(5): p. 2555-2567.

39. Zou, X.Q., et al., *Molecular interactions between graphene and biological molecules.* Journal of the American Chemical Society, 2017. **139**(5): p. 1928-1936.

40. Tsuzuki, K., et al., *Reduced graphene oxide as the support for lipid bilayer membrane.* Asia-Pacific Interdisciplinary Research Conference 2011 (Ap-Irc 2011), 2012. **352**: p. 012016.

41. Lei, H.Z., et al., *Morphology change and detachment of lipid bilayers from the mica substrate driven by graphene oxide sheets.* Langmuir, 2014. **30**(16): p. 4678-4683.

42. Sironi, B., *Lipid adsorption at interfaces: a synchrotron X-ray reflectivity study.*, in *School of Chemistry*. 2016, University of Bristol: Bristol, UK.

43. Als-Nielsen, J. and McMorrow, D., *Elements of modern X-ray physics.* 2nd ed. 2011, Oxford: Wiley-Blackwell. xii, 419 p.

44. Nevot, L. and Croce, P., *Characterization of surfaces by grazing X-ray reflection - application to study of polishing of some silicate-glasses.* Revue De Physique Appliquee, 1980. **15**(3): p. 761-779.

45. Snow, T., *Polymer brushes on charged surfaces: synthesis, characterisation and interactions*, in *Bristol, UK*. 2015, University of Bristol: University of Bristol.

46. *The atomic scattering factor files*. 1993; Available from: http://henke.lbl.gov/optical_constants/asf.html.

Chapter 2

Methods

In this chapter, the instruments in this project and the corresponding experimental setups are described. Moreover, the data analysis method and the calculation of the scattering length density are also outlined.

2.1 X-Ray Reflectivity

2.1.1 Experimental setup

Synchrotron X-ray reflectivity (XRR) measurements were performed at beamline BM28-XMaS, European Synchrotron Radiation Facility (ESRF), Grenoble, France. A custom designed sample cell was used in all XRR experiments, as shown schematically in Figure 2.1 [1, 2]. The cell, originally designed to accommodate the "bending mica method" [3], consists of a chamber to house the sample stage for both curved and flat substrates. Temperature control in the range 10 - 90 ºC is facilitated by two brass jackets sandwiching the chamber, one to house electrical heaters and the other connected to a water bath to provide cooling. Graphene samples were mounted on the sample stage in the XRR cell, which was sealed *via* two polyester (Mylar®) windows.

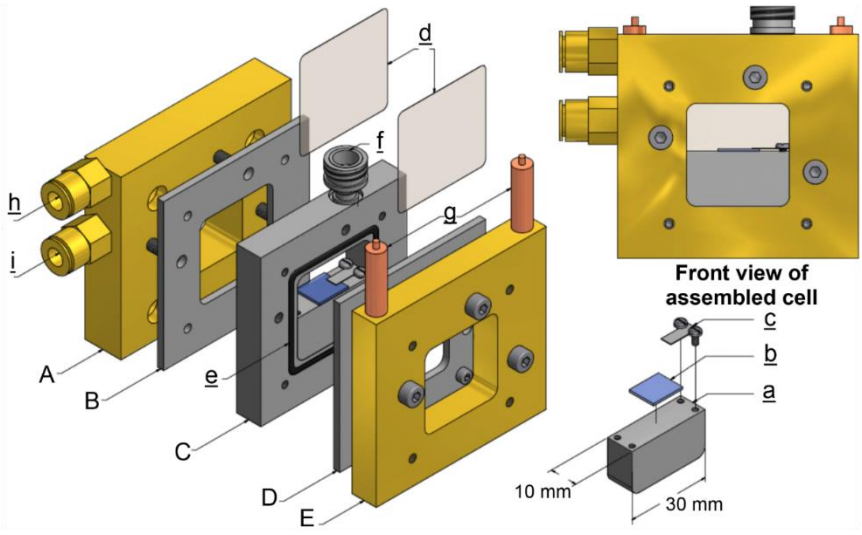

Figure 2.1. Key components of the XRR cell, consisting of three stainless steel plates (B-D), and the cooling (A) and heating jackets (E). Two Mylar® windows (d) are clamped between plates B, D and plate C, creating a liquid chamber with a capacity of 5 ml. Sealing is facilitated by means of O-rings placed in grooves (e). The samples (b) 1 cm × 1 cm in

size are clamped by two small plates (c), onto a stainless steel stage (a). A nozzle (f) allows *in situ* liquid/gas exchange. The heating jacket can be controlled by two heaters (g) while the cooling jacket can be connected to a water circulating bath *via* an inlet (i) and an outlet (h).

The X-ray beam energy used in this project was 14 keV (wavelength λ = 0.8856 Å), and the incident beam size defined by aperture slits was 100 µm (vertical FWHM) × 255 µm (horizontal FWHM). Specular XRR scans were collected with the incident angle θ_i varying from 0.06-3.0º and the reflection angle $\theta_r = \theta_i$, corresponding to a momentum of transfer $\boldsymbol{Q} = 4\pi\sin(2\theta/2)/\lambda$ range of 0.015 - 0.74 Å^{-1}, where $2\theta = \theta_r + \theta_i$. The specular reflection was detected at each angle using an avalanche photodiode detector (APD), as shown in Figure 2.2.

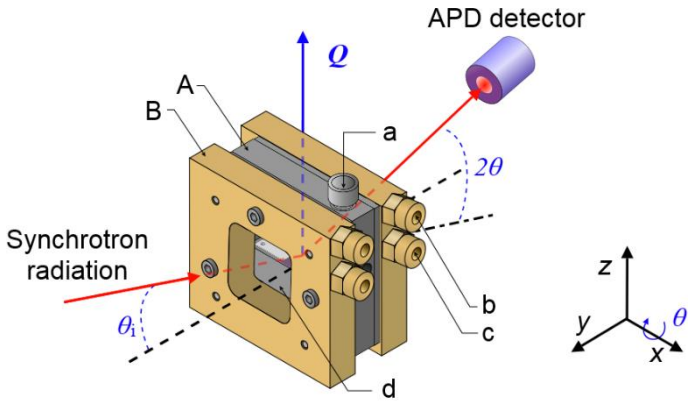

Figure 2.2. Schematic of the XRR experiment setup with an incident synchrotron X-ray beam reflected from the sample with an incident angle θ_i to the avalanche photodiode detector (APD) that collects the specular reflection.

2.1.2 Data analysis

The raw reflection data was saved in a space delimited text (SPEC), which was then extracted into text files (txt) and processed for further analysis. When the incident angle is smaller than a "critical" angle θ_s, where the beam height (H_0) equals to the beam height that hits on the sample (H) as shown in Figure 2.3, the footprint (the projection of the beam onto the sample surface of the beam, e.g. along x axis, it is L_0) will exceed the physical dimensions of the samples, reducing the beam intensity. θ_s is defined as:

$$\sin\theta_s = \frac{H}{L}, \qquad \text{Equation 2.1}$$

where L is the length of the sample.

And when an incident beam hits the sample at angle θ, the corresponding H (Figure 2.3) can be given by:

$$H(\theta)=L\sin\theta. \qquad \text{Equation 2.2}$$

The grazing angle range for the reflection measurements was set between 0-3°, which ensured the incident beam always exceed the sample length. As such, a "footprint correction" for the beam intensity is needed. The most straight forward way to correct the intensity of the beam can be given by a geometric argument:

$$I_c=\frac{I_r\times\sin\theta_s}{\sin\theta_i}\ , \qquad \text{Equation 2.3}$$

where I_c is the corrected intensity, I_r is the detected beam intensity, and θ_i is the incident angle.

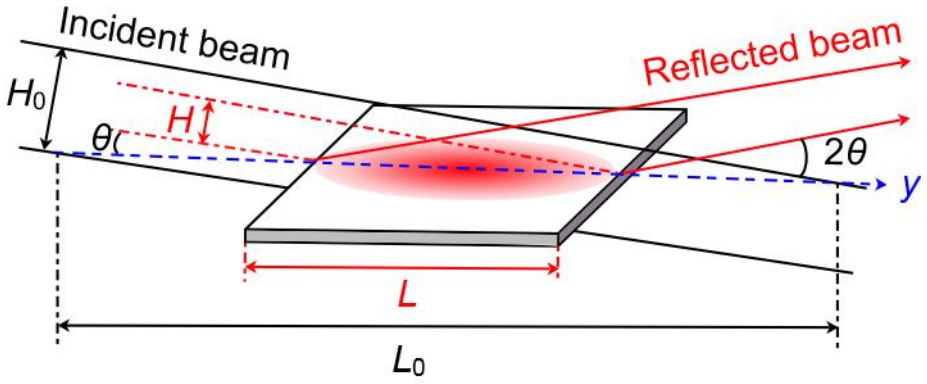

Figure 2.3. A schematic showing an X-ray beam striking a sample with a width of L at angle θ. The incident beam has an intensity of I_0 and beam height of H_0, while the beam that hits on the sample has a height of H. When $H_0 > H$, the beam footprint along the y axis is L_0, the intensity of the reflected beam, I_r, that collected by the detector needs to be corrected as the beam only hits the sample partially.

In addition, as shown in Figure 2.4a, a real beam source normally generates a Gaussian beam, instead of a uniform one. A well-defined height (z) scan (Figure 2.4b) is therefore collected at an angle $\theta = 2\theta = 0$, where the highest beam intensity can be detected, to generate the Gaussian profile of the applied beam source for the correction of the intensity of the collected data [4]. The intensity profile can be deduced from the first order

differential of the *z*-scan, which can then be fitted applying a Gaussian fit (x = 0 was set as the peak of the beam intensity):

$$G(x)=Ae^{(-\frac{x}{2c^2})}, \qquad \text{Equation 2.4}$$

where A is the peak amplitude and c follows the relationship with the full-width at half maximum (FWHM) of the peak that given by:

$$\text{FWHM}=2\sqrt{2\ln 2}c\,. \qquad \text{Equation 2.5}$$

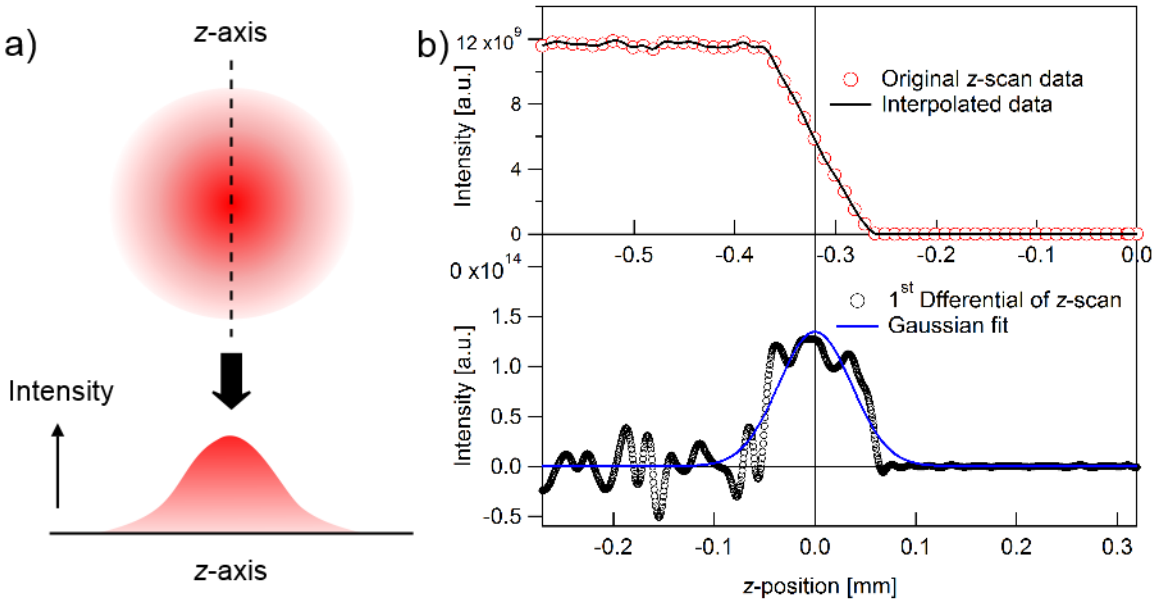

Figure 2.4. a) An illustration of a cross section of a beam whose intensity satisfied a Gaussian profile. a) A *z*-scan profile (red circles) and its spline fitting (black solid line) are plotted at the top, comparing with the beam intensity profile (black circles) among the *z*-axis and its fitted Gaussian distribution (blue solid line) at the bottom.

The total reflected intensity I_r from the sample with a width of L at angle θ, can thus be expressed as the integration of the Gaussian fits at the corresponding angle within $H(\theta)$:

$$I_r=\int_{-\frac{H(\theta)}{2}}^{\frac{H(\theta)}{2}} G(x)\mathrm{d}x\,. \qquad \text{Equation 2.6}$$

Then the corrected intensity I_c can be obtained from the reflected intensity I_r from the relation of the integral of $G(x)$ within the limits $H(\theta)$, divided by the total beam intensity:

$$I_c = I_r / \left(\frac{\int_{-\frac{H(\theta)}{2}}^{\frac{H(\theta)}{2}} G(x)\mathrm{d}x}{\int_{-\frac{H_0(\theta)}{2}}^{\frac{H_0(\theta)}{2}} G(x)\mathrm{d}x} \right), \qquad \text{Equation 2.7}$$

where $H_0(\theta)$ is the real beam height as shown in Figure 2.3.

After the correction of the raw data, *Motofit* in *Igor Pro* (WaveMetrics, Inc., Lake Oswego, OR, USA) was used for curve fitting. For reflectivity data collected on a well-defined flat substrate such as silicon, the surface layer was modelled as stacked homogeneous slabs. Each layer can be described by three parameters: the scattering length density (SLD, ρ), thickness t, and inter-slab roughness R_a (*cf.* Figure 0.5). These parameters were varied in the total reflectivity calculation using the Abeles matrix method, which yields the same result as Parratt's recursive method (*cf.* section 1.4.3) [5]. In this case, the wavevector, k, in layer n, is given by:

$$k_n = [k_0^2 - 4\pi(\rho_n - \rho_0)]^{1/2}, \qquad \text{Equation 2.8}$$

where:

$$k_0 = Q/2. \qquad \text{Equation 2.9}$$

The Fresnel reflection coefficient (r) between layer n and layer $n + 1$ is then given by:

$$r_{n,n+1} = \frac{k_n - k_{n+1}}{k_n + k_{n+1}}. \qquad \text{Equation 2.10}$$

If taken roughness (R_a) into account, as described by Nevot and Croce [6], it can be described as:

$$r_{n,n+1} = \frac{k_n - k_{n+1}}{k_n + k_{n+1}} e^{-1/2 k_n k_{n+1} R_{a_{n,n+1}}^2}. \qquad \text{Equation 2.11}$$

A genetic algorithm optimisation is adopted in this software to minimize the χ^2 value, which shows the goodness of fitting,

$$\chi^2 = \sum_{n=1}^{L} \frac{1}{L - P} \left(y_{0,n} - y_n \right)^2, \qquad \text{Equation 2.12}$$

where L is the number of collected data points; P the number of variables which are varied during fitting, *e.g.* n, ρ_n, t_n, and $R_{a,n}$; y_0 the measured value; and y_n the corresponding theoretically fitted value yielded from the used parameters.

2.1.3 Calculation of the SLD

For a material with homogeneous electron distribution, the calculation of SLD should be straightforward, using the equations described in section 1.4.6. However, for amphiphiles, such as lipids and surfactants, due to their uneven electron distribution, the SLD contrast between the headgroup and the tail is often large enough to be considered separately [2, 7-9]. The structure of phosphatidylcholine (PC) lipids is commonly divided into two regions for studies [8, 10]: the phosphatidylcholine polar headgroup (phosphate, choline, glyceryl, and two carbonyl groups) and the non-polar hydrocarbon tails, as shown in Figure 2.5. Not only the wettability of these two regions are different, but also the electron density, which is richer in the headgroup part.

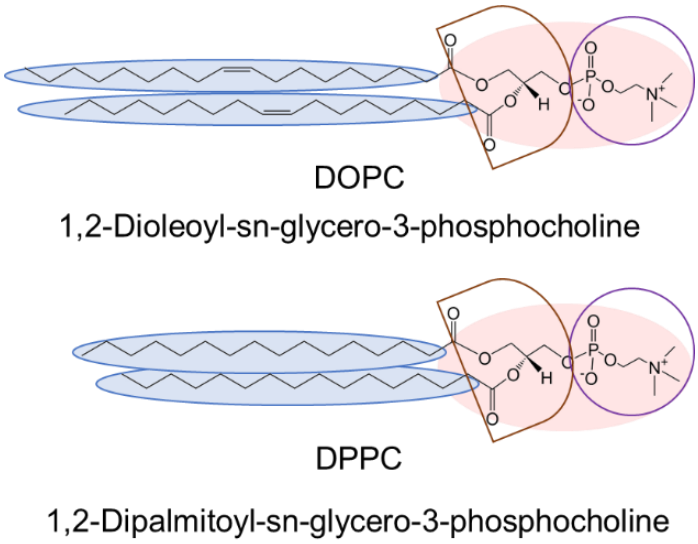

Figure 2.5. The headgroup (highlighted in the pink ovals) and hydrocarbon (highlighted in the blue ovals) tail regions of DOPC and DPPC lipids. The PC headgroup is comprised of a phosphocholine group (circled in purple), a glyceryl group and a carbonyl groups (highlighted in the brown shapes).

In section 1.4.6, Equation 0.26, when calculating the SLD of a substance, V is required. Works that determined the V of PC headgroup and the DOPC and DPPC hydrocarbon tails can be found in literature, as phospholipid is the one of the main components of a cell membrane, which has attracted wide interest on its structure in biology area. Studies

have also been carried out to estimate the structure of hydrated lipid membranes in aqueous medias, both from computer simulation [10, 11] and experiments [11, 12]. For the calculations in this study, *V* of the lipid headgroups and tails were adopted from the values reported by Nagle *et al.*, as shown in. To prove the SLD of the phosphocholine and triformate (glyceryl and carbonyl groups) can be recognized as a uniform layer by XRR, which turned out to be positive, a more specific volume determination given by Armen *et al.*, was used. Moreover, in consideration of the transition temperature (T_m) of DPPC (T_m = ~ 41 °C), where the physical state of the hydrocarbon chains changes from the ordered gel phase to the fluid liquid-crystalline phase, the SLD used for fitting XRR data collected below 40 °C was calculated from the volume reported for DPPC chain below its T_m, and for those collected at and above 40 °C, the SLD was calculated from the volume reported above its T_m. The T_m of lipids used in this study are listed in Table 2.1, the atomic volume and the corresponding SLD are listed in Table 2.2.

Table 2.1. The abbreviation, molecular formula, headgroup and carbon tail structures, molecular weight (M_w) and the transition temperature Tm of the lipids used for interacting with graphene surfaces.

Lipid	**Formula**	**Carbon chain**	**Headgroup**	M_w **(g mol^{-1})**	T_m **(°C)**
DOPC	$C_{44}H_{84}NO_8P$	$C_{17}H_{33}$	$C_{10}H_{18}NO_8P$	786.11	-17
DPPC	$C_{40}H_{80}NO_8P$	$C_{15}H_{31}$	$C_{10}H_{18}NO_8P$	734.039	41

Table 2.2. The molecular volume (*V*) and corresponding real part of SLD (ρ_r) of the segments that compose lipids. The *V* values are cited from the studies reported by [a] Armen [11], and [b] Nagle [13].

	V **(Å^3)**	ρ_r **(10^{-6} Å^{-2})**
Carboxyl	39[a]	14.45
Glyceryl	68.8[a]	
Phosphoryl	53.7[a]	14.42

Choline	120.4[a]	
Lipid headgroup	319[b]	14.52
DOPC carbon chain	492.0[b]	7.74
DPPC carbon chain > T_m	455.6[b]	7.48
DPPC carbon chain < T_m	412.5[b]	8.27

The calculated SLDs related to this study are listed in Equation 0.28 in section 1.4.6.

Table 2.3; the molecular volume V required in Equation 0.26 of graphene is obtained directly from its bond length (1.43 Å [14]) and theoretical thickness (3.5 Å), as graphene is not a conventional flat thin film. The V values of ions was calculated from their intrinsic radius [15]. Volumes of the PC headgroup and the lipid carbon tails have been described above in Table 2.2, and those of the other materials were calculated from their mass density ρ_m from Equation 0.28 in section 1.4.6.

Table 2.3. Calculated ρ (with a beam energy of 14 keV).

	Molecular formula	**ρ_r (10^{-6} Å^{-2})**	**ρ_m (Å^{-2})**
Water	H_2O	9.44	9.427×10^{-09}
Graphene	C	18.2	8.179×10^{-09}
Silica	SiO_2	18.74	8.089×10^{-08}
PMMA	$(C_5O_2H_8)_n$	10.81	6.702×10^{-9}
Silanol	$Si(OH)_x$	28.72	9.798×10^{-08}
PC headgroup	$C_{10}H_{18}NO_8P$	14.52	2.314×10^{-08}
DOPC chain	$C_{17}H_{33}$	7.74	2.628×10^{-09}
DPPC chain > T_m	$C_{15}H_{31}$	7.48	2.499×10^{-09}
DPPC chain < T_m	$C_{15}H_{31}$	8.27	2.766×10^{-09}
K^+	K^+	55.06	1.020×10^{-06}

Na^+	Na^+	86.75	3.100×10^{-07}

However, there are still controversies on the volumes of graphene, lipids and ions, beyond which, the complex environmental conditions made the SLD of the materials uncertain. To get better fitting resolutions, when processing the XRR data, the SLD of complicated layers, namely the graphene layer (with ions adsorbed), the lipid layer, the silanol layer and the air bubble layer were allowed to vary freely, for well-studied materials such as water, silica, the SLD was allowed to vary with an error of 0.5×10^{-6} $Å^{-2}$.

2.2 Atomic Force Microscopy

Atomic force microscopy (AFM) is widely used to investigate the topological morphology and the force information of samples, it is also one of the first technique used to reveal the structure of graphene [16]. The atomic force microscopy (AFM) investigation was conducted in ambient conditions using a MultiMode VIII microscope with a NanoScope V controller, utilizing PeakForce feedback control (Bruker, CA, USA). The cantilever employed was SCANASYST_FLUID+ with nominal spring constant and tip radius of 0.7 N m^{-1} and 2 nm, respectively.

2.3 Ellipsometry

Ellipsometry is a a non-invasive and non-destructive technique to determine the structural properties of thin films such as thickness, composition, roughness, and refractive index. The experiments were performed using a J.A. Wollam M-2000 ellipsometer (J.A. Woollam Company, Incorporated, Lincoln, NE, USA), to obtain the total thickness of the graphene sample, using a white light source (wavelengths of 245 - 1000 nm) at a fixed incident angle of 75º. The obtained data was processed and fitted using VASE 32 software from J.A. Wollam adopting a three-layer model consists of a silicon substrate, a silicon dioxide layer and a graphene layer.

2.4 NanoESCA Facilities

The X-ray photoelectron spectroscopy (XPS) and the photoemission electron microscopy (PEEM) measurements of the samples were performed at the Bristol NanoESCA II facilities. XPS measurements were performed with an Argus spectrometer before and after annealing at 450 ºC at an ultra-high vacuum (UHV) base pressure of 4.0×10^{-11} mbar for 1 h. Core-level photoemission spectra were acquired at 45° *w.r.t.* the sample surface,

using a monochromatic Al Kα (1486.7 eV) X-ray source with a pass energy of 20 eV at room temperature (RT) and an estimate total energy resolution of 600 meV. The relative composition of C, O, and Si can be calculated from the corresponding photoemission line intensity.

The PEEM was performed at RT under the UHV condition with a pass energy of 50 eV, a lateral resolution of 150 nm, and an overall energy resolution of 140 meV. The energy calibration was confirmed by fitting a Fermi edge of a clean metallic substrate at the same measurement condition. A He I (21.2 eV) discharge lamp was used as excitation source, and the absolute work function measurement for a particular sample area was obtained from electronic counting of the emitted photoelectrons [17]. The work function values in the maps were obtained by fitting the 600 × 600 camera pixels spectra with an "error function". The low excitation photon energy makes PEEM extremely surface sensitive (to 2-3 atomic surface layers), and the PEEM images were acquired after cleaning by annealing to show the surface morphology.

2.5 Dynamic Light Scattering

The hydrodynamic diameter (D_z) and polydispersity index (PDI) of the vesicles were determined by dynamic light scattering (DLS), using a Malvern Nano Zetasiser ZS (Malvern, Instruments, Malvern, Worcestershire, UK), since it has been reported that uniform liposomes forms more homogenous membrane structure [8]. The DLS instrument is with a λ = 633 nm laser set measuring in the Non-Invasive Backscatter (NIBS) mode at 173°. Main components of the DLS instrument (Malvern Nano Zetasiser ZS) is illustrated in Figure 2.6.

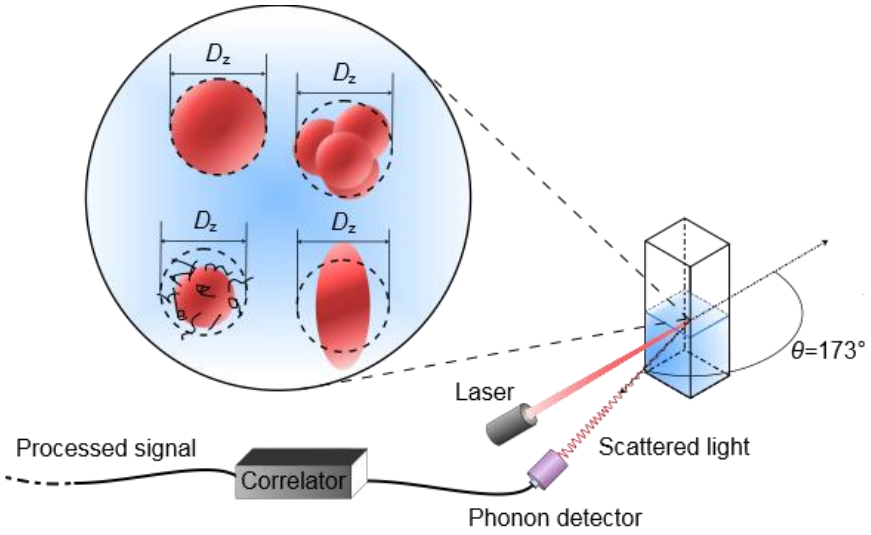

Figure 2.6. Key components of the DLS instrument, which applied a backscatter mode that collected scatterings at 173°. The hydrodynamic size of different type of particles is also shown.

Dynamic light scattering (DLS) is widely used in colloidal science to determine the hydrodynamic size of particles, vesicles can proteins. DLS has a list of advantages in terms of size determination in biotechnology, to name but a few, it is non-invasive, it is fast, it is insensitive to noise and it generates results in liquid solutions, where most of bioreactions happen. Hydrodynamic diameter (D_z) is the diameter of a sphere that exhibits the same translational diffusion coefficient (D_t) as the measured particle (shown in Figure 2.6). When the measured particle is non-spherical, which is the most common situation in scientific research, the D_z is not the actual size of the particle, but also includes a hydration layer. The relationship between D_t and D_z is given by the Stokes-Einstein equation [18]:

$$D_z = \frac{k_B T}{3\pi\eta_s D_t}, \qquad \text{Equation 2.13}$$

where k_B is the Boltzmann's constant, T is the environmental temperature, and η_s is the solvent viscosity.

The mechanism of the DLS is based on the theory that because of Brownian motion, which is related to the hydrodynamic diameter of the particles, the intensity of scattered beam from dispersed particles fluctuates as a function of time. Therefore the obtained $D_{t,ave}$ from DLS is the intensity weighted diffusion coefficient, the given average

hydrodynamic diameter (often expressed as the "z-average size") should be the intensity weighted harmonic mean size as it is inversely proportional to D_t [19].

2.6 Contact Angle Measurement

The water contact angle measurements can be used to evaluate the wettability of a solid material. In order to exam the hydrophobicity of graphene surface, the static contact angle measurements have been performed, using the Sessile drop method on a KRÜSS® DSA100 instrument.

References

1. Briscoe, W.H., et al., *Synchrotron XRR study of soft nanofilms at the mica-water interface.* Soft Matter, 2012. **8**(18): p. 5055-5068.

2. Speranza, F., et al., *Quiescent bilayers at the mica-water interface.* Soft Matter, 2013. **9**(29): p. 7028-7041.

3. Briscoe, W.H., et al., *Applying grazing incidence X-ray reflectometry (XRR) to characterising nanofilms on mica.* Journal of Colloid and Interface Science, 2007. **306**(2): p. 459-463.

4. Sironi, B., *Lipid adsorption at interfaces: a synchrotron X-ray reflectivity study.*, in *School of Chemistry*. 2016, University of Bristol: Bristol, UK.

5. Nelson, A., *Co-refinement of multiple-contrast neutron/X-ray reflectivity data using MOTOFIT.* Journal of Applied Crystallography, 2006. **39**: p. 273-276.

6. Nevot, L. and Croce, P., *Characterization of surfaces by grazing X-ray reflection - application to study of polishing of some silicate-glasses.* Revue De Physique Appliquee, 1980. **15**(3): p. 761-779.

7. de Ghellinck, A., et al., *Probing the position of resveratrol in lipid bilayers: a neutron reflectivity study.* Colloids and Surfaces B-Biointerfaces, 2015. **134**: p. 65-72.

8. Sironi, B., et al., *Structure of lipid multilayers via drop casting of aqueous liposome dispersions.* Soft Matter, 2016. **12**(17): p. 3877-3887.

9. Eicher, B., et al., *Joint small-angle X-ray and neutron scattering data analysis of asymmetric lipid vesicles.* Journal of Applied Crystallography, 2017. **50**: p. 419-429.

10. Petrache, H.I., Feller, S.E., and Nagle, J.F., *Determination of component volumes of lipid bilayers from simulations.* Biophysical Journal, 1997. **72**(5): p. 2237-2242.

11. Armen, R.S., Uitto, O.D., and Feller, S.E., *Phospholipid component volumes: determination and application to bilayer structure calculations.* Biophysical Journal, 1998. **75**(2): p. 734-744.

12. Als-Nielsen, J. and McMorrow, D., *Elements of modern X-ray physics*. 2nd ed. 2011, Oxford: Wiley-Blackwell. xii, 419 p.

13. Nagle, J.F. and Tristram-Nagle, S., *Structure of lipid bilayers.* Biochimica Et Biophysica Acta-Reviews on Biomembranes, 2000. **1469**(3): p. 159-195.

14. Warner, J.H., et al., *Bond length and charge density variations within extended arm chair defects in graphene.* Acs Nano, 2013. **7**(11): p. 9860-9866.

15. Slater, J.C., *Atomic radii in crystals.* Journal of Chemical Physics, 1964. **41**(10): p. 3199-3204.

16. Novoselov, K.S., et al., *Electric field effect in atomically thin carbon films.* Science, 2004. **306**(5696): p. 666-669.

17. Li, W.Y., Goto, K., and Shimizu, R., *PEEM is a suitable tool for absolute work function measurements.* Surface and Interface Analysis, 2005. **37**(2): p. 244-247.

18. Koppel, D.E., *Analysis of macromolecular polydispersity in intensity correlation spectroscopy - method of cumulants.* Journal of Chemical Physics, 1972. **57**(11): p. 4814-4820.

19. Thomas, J.C., *The determination of log normal particle-size distributions by dynamic light-scattering.* Journal of Colloid and Interface Science, 1987. **117**(1): p. 187-192.

Chapter 3

Surface Structure of Few Layer Graphene

(A paper based on this chapter, as attached in Appendix VII, has been published in *Carbon, 2018. 136: p. 255-261*: *https://doi.org/10.1016/j.carbon.2018.04.089*)

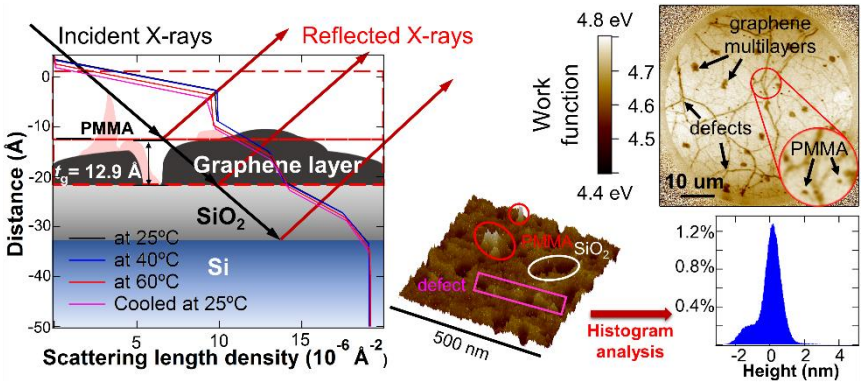

Understanding surface structure of graphene is important for its integration into composite materials. In this chapter, we have used synchrotron X-ray reflectivity (XRR) to study the structure of commercially available graphene samples (prepared via chemical vapour deposition, and marketed as graphene monolayers) on SiO_2/Si at different temperatures. X-ray photoelectron spectroscopy, photoemission electron microscopy and atomic force microscopy (AFM) were employed to evaluate the composition and morphology of the graphene layer. The results suggest that the samples we characterized consisted of 3 - 4 layers of graphene, which should thus be more accurately described as few layer graphene (FLG). Furthermore, a "contaminant" layer, comprising polymethylmethacrylate and graphene multilayers, was found present atop FLG. We also report tentative results on the effect of temperature on the graphene sample thickness. At 25 ºC, the FLG thickness from XRR measurements was 13.0 ± 1.0 Å, in agreement with that obtained from AFM (13.9 ± 0.7 Å). Upon heating to 60 ºC, the FLG thickness expanded to 13.8 Å, which further increased to 14.3 Å upon cooling to 25 ºC. We attribute this temperature dependent thickness to the out-of-plane rippling of graphene as previously reported. These unprecedented results on the FLG surface structure are valuable to its potential bioanalytical applications.

3.1 Introduction

Since the 1970s, studies on growing graphene monolayers on crystals have been carried out, and the first graphene was successfully exfoliated in 2004 by Novoselov and Geim [1]. Different techniques have been employed for the structural characterisation of graphene and its derivatives, as listed and compared in Another powerful technique is X-ray reflectivity (XRR), which is widely used for probing buried interfaces and thin film monolayers [28], bilayers [29, 30] and multilayers [31] structures. XRR has been used to study the structure of graphene coated with other popular materials in electronic devices (*e.g.* HfO2 [32], Au [33], and perylenetetracarboxylic dianhydride (PTCDA) [34]), and exposed and buried interfacial structures of graphene grown on SiC [35, 36], showing its potential to be used on the structural characterization of graphene.

Table 3.1. For instance, graphene on silica was first revealed by optical microscopy, scanning electron microscopy (SEM), and atomic force microscopy (AFM) [1]. Non-destructive techniques such as electron microscopy (EM) [2-10], Raman/Rayleigh scattering microscopy [4, 11-15], ellipsometry [16, 17], and near edge X-ray absorption spectroscopy (NEXAS) [18, 19] have been used to study the graphene structure and/or its adsorbates. For the in-plane structural characterisation, scanning tunnelling microscopy (STM) and scanning tunnelling spectroscopy (STS) [2, 5, 20, 21] have been used to image the graphene lattice. X-ray photoelectron spectroscopy (XPS) and Auger electron spectroscopy (AES) [22-24] assisted by low energy electron microscopy (LEEM) and photoemission electron microscopy (PEEM) measurements [6, 20, 25-27] have also been employed for the compositional, structural and morphological characterisation of graphene on conductive substrates. However, these techniques have a limited capacity to probe the out-of-plane structure of the adsorbed layer.

Another powerful technique is X-ray reflectivity (XRR), which is widely used for probing buried interfaces and thin film monolayers [28], bilayers [29, 30] and multilayers [31] structures. XRR has been used to study the structure of graphene coated with other popular materials in electronic devices (*e.g.* HfO_2 [32], Au [33], and perylenetetracarboxylic dianhydride (PTCDA) [34]), and exposed and buried interfacial structures of graphene grown on SiC [35, 36], showing its potential to be used on the structural characterization of graphene.

Table 3.1. A summary of few well-established structural characterisation methods for graphene.

Technique	Description	Advantages	Restrictions
Optical microscopy [1, 15]	Graphene can be seen on 300 nm SiO_2	Non-destructive, efficient, low cost	Limited substrate
EM	SEM [1] transmission electron microscopy (TEM) [2-10]	Non-destructive, can observe the graphene surface structure and possible contaminants with Ångström resolution	Complementary methods are needed for determining the number of layers
AFM [1]	One of the most common methods to determine the graphene thickness	Can provide direct thickness information	Destructive, and the obtained apparent thickness is overestimated, due to the chemical contrast and the unknown separation between graphene and its substrate
Raman spectroscopy [4, 11-14], Rayleigh scattering microscopy [15], ellipsometry [16, 17]	Quick methods of counting the number of layers of graphene. Raman spectroscopy is also used to determine the defects and contaminants of graphene	Non-destructive, efficient, and the methods are well-established	No information about the surface morphology
STM and STS [2, 5, 20, 21]	Scanning tunnelling microscopy could provide clear image of the graphene in-plane lattice structure and defects	Non-destructive, Ångström resolution	Only provide the surface morphology
Electron Spectroscopy for Chemical Analysis (ESCA)	XPS, AES [22-24], LEEM, and PEEM [6, 20, 25-27]	Can determine the thickness, the impurity (XPS, AES), the moiré structure (PEEM, LEEM) and stacking structure (LEED) with atomic precision	No information about the thickness of graphene.
X-ray diffraction (XRD), selected area diffraction (SAD) [3, 7, 8, 37] and NEXAS [18, 19]	Usually applied to detect the functionalisation (XRD, SAD) or chemical absorption (NEXAS) on graphene.	Non-destructive	No information about the surface morphology and thickness of graphene

In this chapter, commercially available graphene samples on Si/SiO_2 widely used in the studies of graphene applications have been studied using synchrotron XRR. XPS, PEEM and AFM were also used to provide complementary information on the composition and

morphology of the samples. Our findings are valuable to graphene research and applications, and also demonstrate the suitability of XRR as a sensitive method for characterising the graphene surface structure, paving the way for further investigations of biomolecular structures on graphene using XRR.

3.2 Experimental

3.2.1 Materials

Graphene samples onto 1 cm × 1 cm Si wafers with 300 nm SiO_2 atop were purchased from *Graphenea Inc* and were prepared by chemical vapour deposition (CVD), the preparation process is described in section 1.2.1. Graphene produced is being marketed as "*monolayer graphene*", and is widely used in the studies to evaluate potential application of graphene monolayers in electronic devices.

3.2.2 Methods

Synchrotron XRR, AFM, XPS and PEEM have been used to study the structure and the composition of commercially available graphene samples. The experimental setups of the techniques are given in Chapter 2. XRR scans were collected at 25 ºC, 40 ºC and 60 ºC in air, with the incident angle θ_i varying from 0.06-3.0º, corresponding to a $\boldsymbol{Q}$ range of 0.015-0.74 $Å^{-1}$, where the vertical momentum transfer vector $\boldsymbol{Q} = 4\pi\sin\theta/\lambda$.

It is useful to compare the footprint size of different complementary methods when interpreting the results. For XPS it was approximately an oval with major/minor axes of 3mm/2mm for PEEM it was 60 µm × 60 µm; for XRR it was 255 µm × 1 cm (the projection of the vertical beam size onto the sample); for ellipsometry the circular spot size was ~3 mm in diameter; for AFM, the scan size was either 5 µm × 5 µm or 1 µm × 1 µm; and for the contact angle measurement, the diameter of the water droplet was of ~3.3 mm. As such, AFM and PEEM provided localised morphological and chemical information, whilst XRR, XPS, ellipsometry, and contact angle provided average structural information across a larger sample area. It is also worth bearing in mind the different conditions for these measurements: XPS and PEEM were carried out under UHV (3×10^{-11} mbar), whilst the rest of the measurements were performed under ambient conditions.

3.3 Results and Discussion

3.3.1 The composition of the graphene samples

The XPS measurements were performed before and after annealing the graphene in UHV sequentially at 200 ºC, 400 ºC, and 450 ºC, which showed that the annealing is more efficient at higher temperatures (> 200 ºC) as shown Figure S1. The photoemission lines are fitted by the programme package *Multipeak* in *Igor Pro*. The XPS spectra from the survey scans of a wide bonding energy range on the graphene sample survey collected before and after annealing at 450 ºC are shown in Figure 3.1a. In both cases, only the presence of C, O, and Si was observed, and no metal residues from the original copper substrate and the etchant were observed on the sample. The elemental compositions estimated from the spectra show that, before annealing, the atomic composition of C, O, and Si was 32.2%, 36.7% and 31.1%, respectively; and after annealing, the percentage of C decreased to 17.4%, but those of O and Si increased to 42.6% and 40.0%, respectively. The C 1s photoemission lines before and after annealing in Figure 3.1b show clear differences in their shape and relative intensity. Deconvolution of these photoemission lines (Figure 3.1c and d; Table S1) indicates the presence of C 1s (sp^2 and sp^3), C-OH and O-C=O [3, 37, 38] before annealing, whereas after annealing, the intensity of the C-OH and C=O peaks dropped remarkedly.

The CVD method is known to produce graphene with an ordered structure and exceptional electronic properties. However, the substrates on which graphene can be grown are limited, and typically transition metals are used. Subsequently, epitaxial graphene often needs to be transferred from the original growth substrate, a process that could cause contamination [39-41]. In this case, there were four possible types of contaminants: the multilayer graphene formed on top of the single layer graphene, the PMMA used for transferring, residues due to incomplete Cu dissolution [42, 43], and etchant liquid residues (typically $FeCl_3$). We ascribe the observed changes in the XPS carbon peaks in Figure 3.1 to PMMA residues being removed by the annealing procedure. This explanation is consistent with the observed decreased C composition (from 32.2% to 17.4%) and C/Si ratio (from 1.03 to 0.44) after annealing. Note that the XPS detection limit was ~ 0.1 atomic% in our measurements.

The annealed samples were further investigated by PEEM, an extremely surface sensitive technique, to reveal their surface morphology, which also helps to identify any possible

contaminants on the graphene surface due to the contrast in their work function. Work function is the energy needed to excite an electron from the Fermi level of the material to free space. An example work function map in Figure 3.1e shows darkened (lower work function) lines and spots appearing on a continuous light background (higher work function). We attribute the dark lines to defects (cracks) likely caused by the transferring process [39], and the spots to two types of contaminants (examples labelled as **A** and **B** on Figure 3.1e). Contaminants **A** (of size ~ 2 μm) were found sparsely over the sample surface, while **B** (of size ~ 500 nm) were found in the vicinity of the defects. The work function of annealed graphene (*i.e.* the light background in Figure 3.1e) was ~ 4.7 - 4.8 eV, which is slightly larger than the reported work function of intrinsic graphene (4.56 eV) [44]. This difference could be related to the redistribution of electrons between the substrate and graphene [27, 45, 46]. Upon annealing, the defects and contaminants **A** remained, whereas contaminants **B** with a lower work function of ~ 4.3 - 4.6 eV gradually disappeared. We thus attribute **B** to PMMA residues from the transferring process of the graphene from its Cu substrate during fabrication. These PMMA residues were removed upon annealing at 450 ºC, an interpretation consistent with a previous study which showed that PMMA was burnt off from the graphene surface at high temperatures in UHV [42, 43].

The formation of multilayer graphene with a size of few micrometres on monolayer graphene grown on Cu has been previously characterised by Raman spectroscopy [47]. Few layer graphene (FLG) with more than 3 graphene monolayers exhibited a work function of 4.6 eV, similar to that of graphite [27, 48, 49]. Thus, contaminants **A** with a work function of ~ 4.6 eV were likely graphene multilayers.

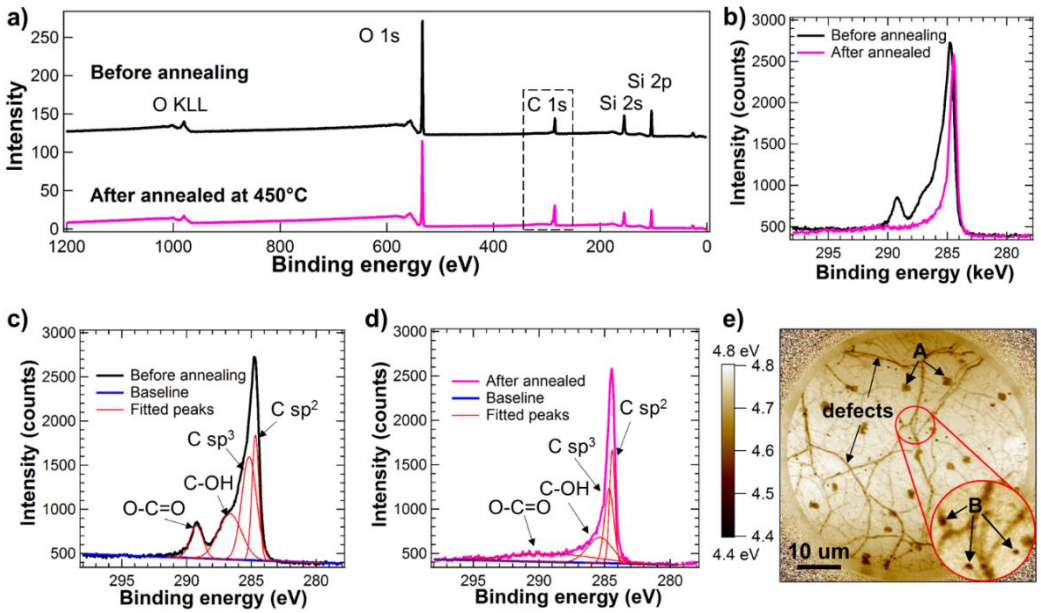

Figure 3.1. a) The XPS surveys for the graphene sample measured before (black line) and after (pink line) annealing. b) shows the C 1s photoemission region highlighted in the dashed rectangle in a), and the fittings for the photoemission lines before and after annealing are shown in c) and d), respectively. The fittings suggest the existence of carbon oxides in the sample, including O-C=O and C-OH, with the peak energy values listed in Table S4 in SI-3. After annealing, the amount of the oxides decreased. e) The work function map of graphene annealed at 450 ºC for 1 h, with 2 types of contaminants labelled as **A** and **B**.

3.3.2 Structure of the graphene samples

Figure 3.2a shows a topographic AFM image on a 1 μm × 1 μm scale, and three line profiles along the coloured lines (with arrows pointing towards the directions of the profiles taken) are shown in Figure 3.2b shown in the corresponding colours. By analysing the topological histograms of the AFM images, the position and the thickness of the graphene layer can be obtained, as described in the section Appendix II. The highlighted areas in the line profiles represent the position of the graphene layer from the histogram analysis, and the PMMA residues with thickness in the range of 0 - 57 Å were seen on top of the graphene surface. Figure 3.2c shows an AFM topological image over a larger scale (5 μm × 5 μm), indicating the deposited graphene appeared continuous with a number of defects (dark holes, *i.e.* **1** in Figure 3.2c) of size ~ 100 nm and a small number of PMMA residues appearing as elevated (lighter) spots. The PMMA residues varied in size (~10-100 nm), and two such spots (**2 and 3**) are circled in the figure. The red

rectangle **(4)** in Figure 3.2c highlights a crack defect on the graphene surface with PMMA partially filling the crack. This interpretation agrees with the work function map (Figure 3.1e), where PMMA was detected around the defects. The apparent thickness of the graphene layer from the height histogram on a scale described in Appendix II is 13.9 ± 0.7 Å, which includes any (small) spacing between graphene and the underlying SiO_2 substrate. The graphene layer thickness points to the presence of the FLG instead of a graphene monolayer, in agreement with numerous AFM studies determining the thickness of graphene and FLG on flat substrates, with the reported thickness ranging from 3.5 Å to 15 Å, depending on the fabrication method and the AFM imaging [1, 50-52].

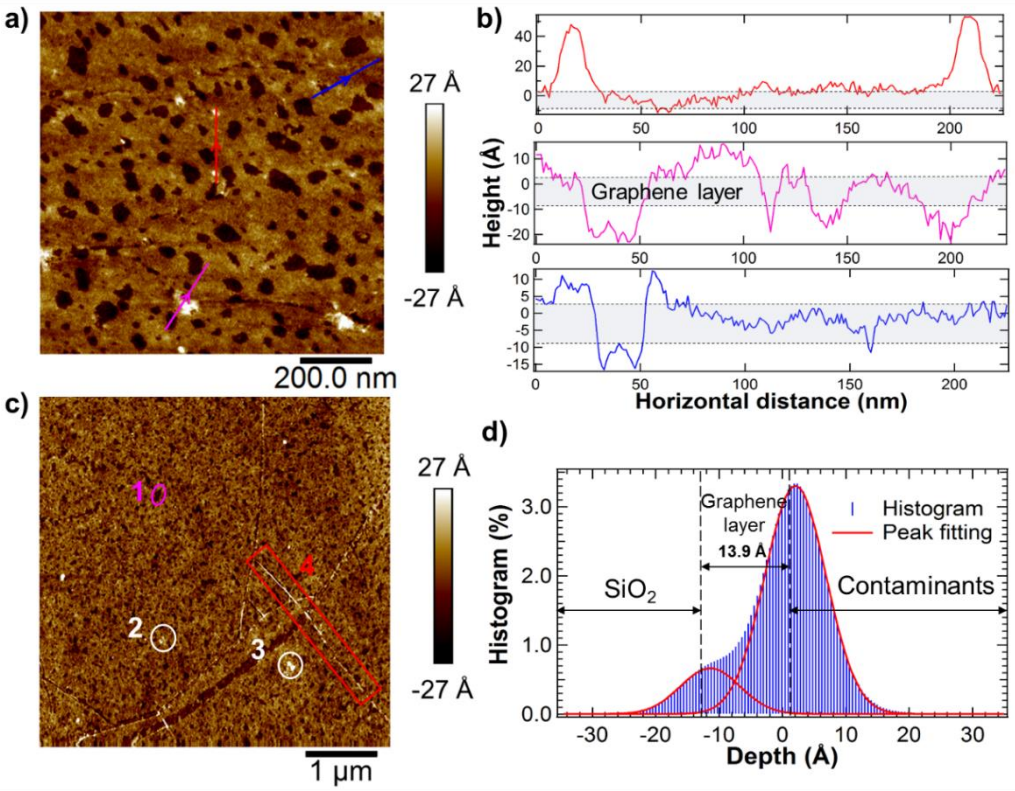

Figure 3.2. a) An example AFM scale topological image on a 1 µm × 1 µm scale; b) Three line profiles followed the direction of the coloured arrow lines in a), with the grey highlighted areas attributed to the graphene layer; c) An example AFM topographic image on a 5 µm × 5 µm scale, highlighting PMMA residues (*e.g.* **2**, **3**) on a continuous graphene layer with holes (*e.g.* **1**) and defects (*e.g.* **4**) exposing underlying SiO_2; d) the corresponding histogram shows the height distribution of SiO_2, graphene, and the contaminant layer.

Assuming PMMA residues existed mostly atop the measured sample, from the height histogram analysis, the graphene coverage on SiO_2 was ϕ_g 85.1 ± 2.1 %, as described in Appendix II. However, if the graphene layer did not remain intact during the transferring process, PMMA could have been transferred onto silica instead of graphene; in that case, the graphene coverage would have been overestimated, whilst that of PMMA underestimated.

The XRR curves of the graphene samples are shown in Figure 3.3b. These curves were collected at 25 ºC, 40 ºC and 60 ºC, and after the sample was cooled back down to 25 ºC after heating. It is interesting to study such a temperature effect, given its relevance to potential biomedical applications of graphene. These results are representative from two separate synchrotron experiments on two different batches of samples from the same supplier. The open circles are the experimental data points, and the solid red lines the fits using a three-layer model, with the details of XRR analysis given in SI-2. The morphology and thickness measurement of graphene from AFM imaging (*cf*. Figure 3.2) indicates that the graphene sample was not a graphene monolayer, but more likely FLG. PEEM (*cf*. Figure 3.1) suggests that a "contaminant" layer was present atop the graphene layer, which was likely a mixture of graphene multilayers and PMMA residues. Therefore, when analysing the XRR data, we have used a three layer Slab Model (Figure 3.3a): a contaminant layer (of thickness t_c) atop a graphene layer (t_g) attached to the substrate with a SiO_2 layer (t_s). The fitted thickness (t), inter-layer roughness (R_a) and SLD (ρ) are listed in Table 3.3. Overall, the structural information from fitting the XRR data is consistent with the observations from AFM and PEEM measurements. The fittings of our sample show an FLG structure instead of monolayer graphene with a contaminant layer on top. As shown in Figure 3.4, neither a monolayer graphene model, nor a model without a contaminant layer can satisfactorily fit the experimental curve. Thus, the three-slab model as demonstrated in Figure 3.3 was applied.

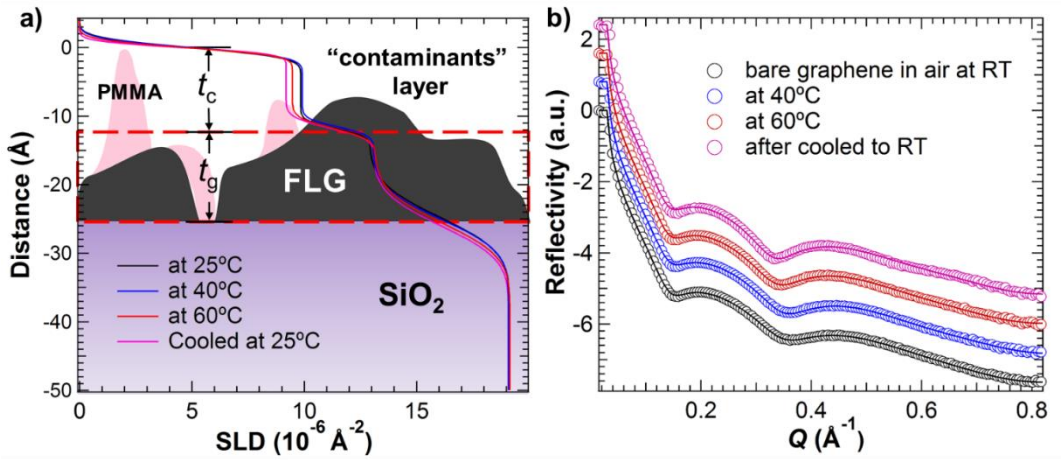

Figure 3.3. a) The fitted SLD profile of the graphene sample at different temperatures with the corresponding physical model used for the fitting. Here, t_c and t_g are the thickness of the 2 slabs representing the contaminants and graphene, respectively. b) The open circles and solid lines are corresponded to the collected XRR data points and fits on a log scale of graphene plotted against $\boldsymbol{Q}$ at different temperatures (with the curves offset vertically for clarity). The fitting parameters are listed in Table 3.3 and Table 3.2.

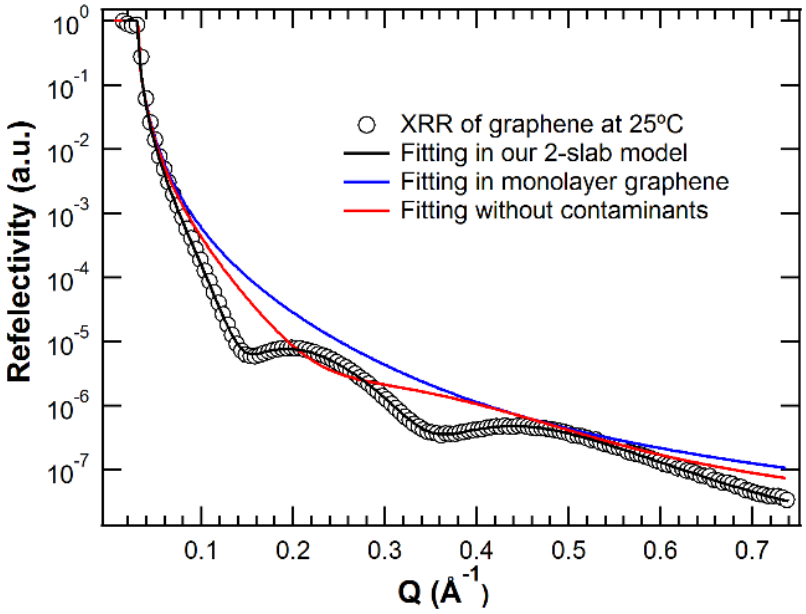

Figure 3.4 XRR results of the commercially available graphene sample (black circles), fitted as FLG with a contaminant layer on top (black line), as monolayer graphene (blue line), and as FLG without contaminants (pink line), respectively.

The average fitted XRR thickness of four different FLG samples from two different sample batches at 25 ºC was t_g = 13.0 ± 1.0 Å as shown in Table 3.2. The fittings are of good qualities (χ^2 < 0.0017), indicating a FLG (t_g = 13.0 ± 1.0 Å) structure. This value is slightly smaller than the AFM thickness of 13.9 ± 0.7 Å (Figure 3.2d), which nonetheless is broadly consistent with the conclusion that the graphene layer was FLG with an average of 3 - 4 graphene monolayers. This is probably due to XRR measurements giving an average thickness over a much larger footprint (~ 10^6 μm^2), while AFM measures the local apparent thickness (with a footprint of ~ 1 μm^2) that is affected by the interaction between the tip and the surface. The total thickness of graphene and the contaminant layers from XRR fitting was ~25 Å, close to the thickness (27.1 ± 0.8 Å) obtained from the ellipsometry measurement on the same samples.

Table 3.2. Fitted XRR results of graphene on Si/SiO_2 samples in air at RT. The samples were purchased in 2 batches, namely [a] and [b].

No.	t_g (Å)	$R_{a,g}$ (Å)	ρ_g (10^{-6} Å^{-2})	ϕ_g (%)	t_c (Å)	$R_{a,c}$ (Å)	ρ_c (10^{-6} Å^{-2})	χ^2 (10^{-3})
1[a]	12.9	0.9	12.9	70.9	11.8	1.2	9.8	1.21
2[a]	12.2	0.0	12.9	70.9	10.4	1.2	9.3	1.62
3[b]	14.4	0.4	14.1	77.7	10.8	2.4	11.9	1.22
4[b]	12.3	2.7	15.6	85.6	15.0	4.3	11.6	1.55
Mean	13.0	1.0	13.9	76.3	12.0	2.3	10.7	1.40
Standard deviation	1.0	1.2	1.3	7.0	2.1	1.5	1.3	0.22

The coverage of each layer can be calculated by comparing the fitted ρ with theoretical values, *i.e.* $\phi = \rho_{fitted}/\rho_{calculated}$. The fitted ρ values of each layer are shown in, the theoretical ρ of each material is listed in Table 2.3; the calculated SLD for graphene is $\rho_g = 1.820\times10^{-5}$ Å^{-2} at 14 keV. The FLG coverage at RT from XRR is ϕ_g = 76.3 ± 7.0 %, broadly

consistent with the value ϕ_g ~ 85.1 ± 2.1% estimated from AFM imaging, with the discrepancy again ascribable to the differences in the footprint size the two techniques probe. As such, the XRR ϕ_g value is an average over a much larger sample area, compared to the localised information from AFM imaging.

Table 3.3. Fitting parameters for XRR results of FLG in air at different temperatures, using the three layer model (*cf*. Figure 3.3a). The SLD (ρ) of graphene and SiO_2 were fixed during fitting, and that of the contaminant layer was fitted in the range between air to FLG, since it is presumed a layer of a mixture with limited coverage instead of a homogeneous film. Also listed are the two fitted interfacial roughness values, $R_{a,c}$ for the roughness at the interface between air and the "contaminant" layer (thus the subscript c) and $R_{a,g}$ for that at the interface between the "contaminant" layer and the graphene layer.

T (°C)	t_g (Å)	$R_{a,g}$ (Å)	ρ_g (10^{-6} Å^{-2})	ϕ_g (%)	t_c (Å)	$R_{a,c}$ (Å)	ρ_c (10^{-6} Å^{-2})	χ^2 (10^{-3})
25	12.9	0.9	12.91	70.9	11.8	1.2	9.80	1.21
40	13.4	1.0	13.06	71.8	11.6	1.1	9.90	1.85
60	13.8	1.3	13.13	72.2	11.8	0.9	9.47	4.57
25 (Cooled)	14.3	1.3	13.08	71.9	11.7	0.7	9.19	9.72

An interesting observation is that the graphene layer thickness t_g experienced a subtle expansion from 12.9 Å at 25 ºC to 13.8 Å at 60 ºC, and the roughness $R_{a,g}$ from 0.9 Å to 1.3 Å correspondingly. Meanwhile, the thickness of the contaminant layer remained largely constant at t_c = 11.7 Å, but its roughness $R_{a,c}$ decreased from 1.2 Å to 0.9 Å from 25 ºC to 60 ºC, suggesting a possible "curing" procedure upon heating, leading to a reduction of the roughness. The $R_{a,c}$ value continued to decrease to 0.7 Å, suggesting possible further relaxation. Furthermore, this change in the graphene layer thickness was irreversible; since after cooling to 25 ºC, t_g further increased slightly to 14.3 Å. This observation might be explained by the out-of-plane motion of graphene, which may also be considered as a perpendicular thermal expansion or enhanced surface ripples. Unlike

most of the materials, including SiO_2 and PMMA, graphene was demonstrated both theoretically and experimentally to have a negative in-plane thermal expansion coefficient (TEC) below ~500 K, as a consequence of decreasing phonon energies exhibited by 2D materials with smaller lattice parameters (rippled) upon heating, in contrast to increasing phonon energies in bulk materials [53-55]. In addition, the asymmetric bond length distribution of graphene caused by the delocalized p-cloud and the structural defects forces graphene to become non-planar to minimize free energy [56]. The rippling of graphene supported by Si/SiO_2 upon heating above 200 K was observed with SEM [57] and Raman spectroscopy [55]. When graphene attached to a SiO_2 substrate is heated, the graphene layer would experience an in-plane compressive stress because of its negative TEC, while SiO_2 would have experienced a tensile stress. Once the force applied on graphene exceeds the vdW attractive force between graphene and the substrate (normally at higher temperature), graphene might escape from the underlying layer to enhance the amplitude of the ripples. This is also consistent with our observation that, after cooling back to RT, the graphene layer thickness detected by XRR further increased. This could be attributed to the tension on the graphene being smaller than the pining force, and the graphene stayed attached to the substrate, manifesting in enhanced rippling. It should be addressed that the conclusions on the temperature dependence of the graphene sample thickness are tentative at this stage, and more measurements are needed to further verify these interesting and important observations.

3.4 Conclusions

The physical properties of graphene are intimately dependent on its thickness and surface structure. Understanding the surface structure of graphene is also important to its integration in composite materials and its bioanalytic applications. In this chapter, XRR was used to study the thickness of commercially sourced graphene prepared using the CVD method on Si/SiO_2 in air at different temperatures for the first time. Such graphene samples have been widely used in research and applications on monolayer graphene. Complementary techniques as AFM, XPS, and PEEM have been used to provide information on topography and chemical compositions of the graphene layer. Our XRR and AFM results show that the thickness of the graphene layer was ~ 13.0 ± 1.0 Å and 13.9 ± 0.7 Å, respectively, corresponding to 3 - 4 graphene monolayers. As such, the samples we characterized appeared to consist of 3 - 4 monolayers of graphene. This may

suggest that other such commercial graphene samples are not of monolayer character. Given that XRR has not been previously widely used for studying the graphene structure, we hope to stimulate further investigations rather than regarding our conclusions as certainty and applicable to all commercial graphene samples. The XPS and PEEM results suggest the presence of PMMA residues from the transfer process of graphene fabrication. In addition, isolated islands of multilayer graphene were also present atop the FLG layer. We also observed a slight but detectable increase of 0.5 - 0.9 Å in the graphene layer thickness as it was heated from room temperature (RT) to 60 ºC. This thermal expansion was irreversible, with the graphene thickness increasing a further 0.5 Å upon cooling back to RT. Such temperature dependent graphene thickness could be attributed to the out of plane rippling behaviour of graphene upon heating as previously reported. It should be addressed that the conclusions on the temperature dependence of the FLG thickness are tentative at this stage, and more measurements are needed to further verify these interesting and important observations.

References

1. Novoselov, K.S., et al., *Electric field effect in atomically thin carbon films.* Science, 2004. **306**(5696): p. 666-669.

2. Novoselov, K.S., et al., *Two-dimensional atomic crystals.* Proceedings of the National Academy of Sciences of the United States of America, 2005. **102**(30): p. 10451-10453.

3. Lesiak, B., et al., *Preparation of graphene oxide and characterisation using electron spectroscopy.* Journal of Electron Spectroscopy and Related Phenomena, 2014. **193**: p. 92-99.

4. Casiraghi, C., et al., *Raman spectroscopy of graphene edges.* Nano Letters, 2009. **9**(4): p. 1433-1441.

5. Ishigami, M., et al., *Atomic structure of graphene on SiO2.* Nano Letters, 2007. **7**(6): p. 1643-1648.

6. Yan, K., et al., *Modulation-doped growth of mosaic graphene with single-crystalline p-n junctions for efficient photocurrent generation.* Nature Communications, 2012. **3**: p. 1280.

7. Tang, L.H., et al., *Preparation, structure, and electrochemical properties of reduced graphene sheet films.* Advanced Functional Materials, 2009. **19**(17): p. 2782-2789.

8. Zhang, K., et al., *Graphene/polyaniline nanofiber composites as supercapacitor electrodes.* Chemistry of Materials, 2010. **22**(4): p. 1392-1401.

9. Mao, Y.D., et al., *Graphene structures at an extreme degree of buckling.* Acs Nano, 2011. **5**(2): p. 1395-1400.

10. Eberlein, T., et al., *Plasmon spectroscopy of free-standing graphene films.* Physical Review B, 2008. **77**(23): p. 233406.

11. Ferrari, A.C., et al., *Raman spectrum of graphene and graphene layers.* Physical Review Letters, 2006. **97**(18): p. 187401.

12. Das, A., Chakraborty, B., and Sood, A.K., *Raman spectroscopy of graphene on different substrates and influence of defects.* Bulletin of Materials Science, 2008. **31**(3): p. 579-584.

13. Huang, M.Y., et al., *Phonon softening and crystallographic orientation of strained graphene studied by Raman spectroscopy*. Proceedings of the National Academy of Sciences of the United States of America, 2009. **106**(18): p. 7304-7308.

14. Hao, Y.F., et al., *Probing layer number and stacking order of few-layer graphene by Raman spectroscopy.* Small, 2010. **6**(2): p. 195-200.

15. Casiraghi, C., et al., *Rayleigh imaging of graphene and graphene layers.* Nano Letters, 2007. **7**(9): p. 2711-2717.

16. Losurdo, M., et al., *Ellipsometry as a real-time optical tool for monitoring and understanding graphene growth on metals.* Journal of Physical Chemistry C, 2011. **115**(44): p. 21804-21812.

17. Al-Hazmi, F.S., et al., *Raman and ellipsometry spectroscopic analysis of graphene films grown directly on Si substrate via CVD technique for estimating the graphene atomic planes number*. Journal of Molecular Structure, 2016. **1118**: p. 275-278.

18. Geng, D.S., et al., *Nitrogen doping effects on the structure of graphene.* Applied Surface Science, 2011. **257**(21): p. 9193-9198.

19. Xu, J.Q., et al., *X-ray absorption spectra of graphene and graphene oxide by full-potential multiple scattering calculations with self-consistent charge density.* Physical Review B, 2015. **92**(12): p. 125408-125419.

20. Sutter, P. and Sutter, E., *Microscopy of graphene growth, processing, and properties.* Advanced Functional Materials, 2013. **23**(20): p. 2617-2634.

21. Rutter, G.M., et al., *Scattering and interference in epitaxial graphene.* Science, 2007. **317**(5835): p. 219-222.

22. Xu, M.S., et al., *Auger electron spectroscopy: a rational method for determining thickness of graphene films.* Acs Nano, 2010. **4**(5): p. 2937-2945.

23. Wang, D.C. and Zhang, Y.M., *Spectroscopic and scanning probe analysis on large-area epitaxial graphene grown under pressure of 4 mbar on 4H-SiC (0001) substratesl.* Chinese Physics B, 2014. **23**(7): p. 10893-10900.

24. Shivaraman, S., et al., *Thickness estimation of epitaxial graphene on SiC using attenuation of substrate raman intensity.* Journal of Electronic Materials, 2009. **38**(6): p. 725-730.

25. Rollings, E., et al., *Synthesis and characterization of atomically thin graphite films on a silicon carbide substrate.* Journal of Physics and Chemistry of Solids, 2006. **67**(9-10): p. 2172-2177.

26. Man, K.L. and Altman, M.S., *Low energy electron microscopy and photoemission electron microscopy investigation of graphene.* Journal of Physics-Condensed Matter, 2012. **24**(31): p. 314209.

27. Kadowaki, R., et al., *PEEM and micro PES study of graphene growth on Ni(110) substrate.* E-Journal of Surface Science and Nanotechnology, 2015. **13**: p. 347-351.

28. Briscoe, W.H., et al., *Applying grazing incidence X-ray reflectometry (XRR) to characterising nanofilms on mica.* Journal of Colloid and Interface Science, 2007. **306**(2): p. 459-463.

29. Giri, R.P., Chakrabarti, A., and Mukhopadhyay, M.K., *Cholesterol-induced structural changes in saturated phospholipid model membranes revealed through X-ray scattering technique.* Journal of Physical Chemistry B, 2017. **121**(16): p. 4081-4090.

30. Speranza, F., et al., *Quiescent bilayers at the mica-water interface.* Soft Matter, 2013. **9**(29): p. 7028-7041.

31. Sironi, B., et al., *Structure of lipid multilayers via drop casting of aqueous liposome dispersions.* Soft Matter, 2016. **12**(17): p. 3877-3887.

32. Jeong, S.J., et al., *Thickness scaling of atomic-layer-deposited HfO2 films and their application to wafer-scale graphene tunnelling transistors.* Scientific Reports, 2016. **6**: p. 20907.

33. Kalbac, M., Vales, V., and Vejpravova, J., *The effect of a thin gold layer on graphene: a Raman spectroscopy study.* Rsc Advances, 2014. **4**(105): p. 60929-60935.

34. Emery, J.D., et al., *Structural analysis of PTCDA monolayers on epitaxial graphene with ultra-high vacuum scanning tunneling microscopy and high-resolution X-ray reflectivity.* Surface Science, 2011. **605**(17-18): p. 1685-1693.

35. Emery, J.D., et al., *Structural consequences of hydrogen intercalation of epitaxial graphene on SiC(0001).* Applied Physics Letters, 2014. **105**(18): p. 161602.

36. Conrad, M., et al., *Structure and evolution of semiconducting buffer graphene grown on SiC(0001).* Physical Review B, 2017. **96**(19): p. 195304.

37. Stobinski, L., et al., *Graphene oxide and reduced graphene oxide studied by the XRD, TEM and electron spectroscopy methods.* Journal of Electron Spectroscopy and Related Phenomena, 2014. **195**: p. 145-154.

38. Stankovich, S., et al., *Synthesis of graphene-based nanosheets via chemical reduction of exfoliated graphite oxide.* Carbon, 2007. **45**(7): p. 1558-1565.

39. Li, X.S., et al., *Transfer of large-area graphene films for high-performance transparent conductive electrodes.* Nano Letters, 2009. **9**(12): p. 4359-4363.

40. Unarunotai, S., et al., *Transfer of graphene layers grown on SiC wafers to other substrates and their integration into field effect transistors.* Applied Physics Letters, 2009. **95**(20): p. 202101.

41. Caldwell, J.D., et al., *Technique for the dry transfer of epitaxial graphene onto arbitrary substrates.* Acs Nano, 2010. **4**(2): p. 1108-1114.

42. Suk, J.W., et al., *Transfer of CVD-grown monolayer graphene onto arbitrary substrates.* Acs Nano, 2011. **5**(9): p. 6916-6924.

43. Lin, Y.C., et al., *Graphene annealing: how clean can it be?* Nano Letters, 2012. **12**(1): p. 414-419.

44. Yan, R.S., et al., *Determination of graphene work function and graphene-insulator-semiconductor band alignment by internal photoemission spectroscopy.* Applied Physics Letters, 2012. **101**(2): p. 022105.

45. Greiner, M.T., et al., *Universal energy-level alignment of molecules on metal oxides.* Nature Materials, 2012. **11**(1): p. 76-81.

46. Fang, C.S.A. and Maloney, C.E., *The effect of substrate work function on work function reduction of Re/W alloy-coated impregnated cathodes.* Applied Physics a-Materials Science & Processing, 1990. **50**(6): p. 603-607.

47. Liu, W., et al., *Synthesis of high-quality monolayer and bilayer graphene on copper using chemical vapor deposition.* Carbon, 2011. **49**(13): p. 4122-4130.

48. Hibino, H., et al., *Dependence of electronic properties of epitaxial few-layer graphene on the number of layers investigated by photoelectron emission microscopy.* Physical Review B, 2009. **79**(12): p. 125437.

49. Datta, S.S., et al., *Surface potentials and layer charge distributions in few-layer graphene films.* Nano Letters, 2009. **9**(1): p. 7-11.

50. Nemes-Incze, P., et al., *Anomalies in thickness measurements of graphene and few layer graphite crystals by tapping mode atomic force microscopy.* Carbon, 2008. **46**(11): p. 1435-1442.

51. Sidorov, A.N., et al., *Electrostatic deposition of graphene.* Nanotechnology, 2007. **18**(13): p. 135301.

52. Chen, Z.H., et al., *Graphene nano-ribbon electronics.* Physica E-Low-Dimensional Systems & Nanostructures, 2007. **40**(2): p. 228-232.

53. Schelling, P.K. and Keblinski, R., *Thermal expansion of carbon structures.* Physical Review B, 2003. **68**(3): p. 035425.

54. Islam, M.Z., Mahboob, M., and Lowe, R.L., *Characterization of the thermal expansion properties of graphene using molecular dynamics simulations.* Journal of Physics D-Applied Physics, 2013. **47**(46): p. 435302.

55. Yoon, D., Son, Y.W., and Cheong, H., *Negative thermal expansion coefficient of graphene measured by Raman spectroscopy* Nano Letters, 2011. **11**(8): p. 3227-3231.

56. Deng, S.K. and Berry, V., *Wrinkled, rippled and crumpled graphene: an overview of formation mechanism, electronic properties, and applications.* Materials Today, 2016. **19**(4): p. 197-212.

57. Bao, W.Z., et al., *Controlled ripple texturing of suspended graphene and ultrathin graphite membranes.* Nature Nanotechnology, 2009. **4**(9): p. 562-566.

Chapter 4

Graphene surface structure in aqueous media

(A manuscript based on this chapter, as attached in Appendix VII, has been submitted to Carbon and is currently under review [Manuscript Number: CARBON-D-18-03004])

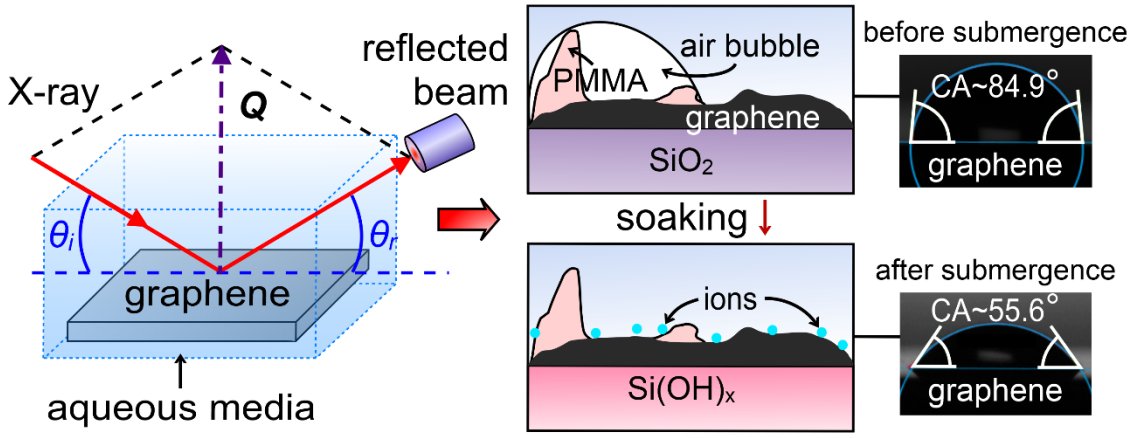

Understanding graphene surface structure in aqueous media is essential for its biotechnological applications. Here, using synchrotron X-ray reflectivity (energy 14 keV), AFM imaging, and contact angle measurements, we have investigated the surface structure of CVD graphene on SiO_2/Si in water and phosphate buffered saline (PBS) at 25 - 60 ºC. We found a diffuse layer immediately adjacent to graphene with a scattering length density (SLD) of 6.72 × 10^{-6} Å^{-2}, attributed to the presence of air bubbles on graphene under water. AFM imaging was indicative of interfacial inhomogeneity, but did not provide conclusive topography information on the bubble-covered graphene-water interface. The diffuse layer diminished after the graphene was submerged in water for 24 h at 25 ºC. This is also evident from its enhanced wettability, with the water contact angle on graphene decreasing from 84.9 ± 0.4° to 55.6 ± 0.4° after submergence. An additional layer atop graphene appeared after soaking, with a thickness 10.1 Å, and a higher SLD of 19.5 × 10^{-6} Å^{-2} at 25 ºC, which increased to 11.8 Å and 21.8 × 10^{-6} Å^{-2} at 60 ºC in PBS, respectively. We discuss this observation in terms of ion mobility, possible formation of a silanol layer on the SiO_2 substrate, and water structure disruption at higher temperatures. The results provide useful information for the interpretation of the morphologies of the lipids adsorbed on graphene in Chapter 5.

4.1 Introduction

With a large active surface area, one-atom thickness, and delocalised π electrons, graphene enables the detection of changes in the surrounding environment with molecular level sensitivity [1], *e.g.* for sensing gases [1], humidity [2], and biomolecules [3]. Potential bioanalytic applications of graphene have also attracted a wide attention. For these applications, graphene often needs to be exposed to or in contact with aqueous systems. Therefore, it is important to understand the structure of graphene in water, since the physical properties of graphene are influenced by its structure (*i.e.* thickness [4, 5], lattice order [6, 7], defects [8, 9], and impurities [10]) and that of the underlying substrate [11].

Several investigations have been reported on the effects of water on graphene and its derivatives. Using contact angle (CA) measurements, it has been shown that the structure (such as thickness and layer stacking) and charge transfer between graphene and its surrounding environment could influence the interaction between water and graphene [2], although the mechanism remains unclear. Specifically, it has been reported that the hydrophobicity of graphene on a copper foil [2] and a SiC wafer [12] increased with the number of graphene layers. Molecular dynamic simulations showed that free-standing graphene was hydrophobic [12, 13], due to the hydrogen bond network within a water double layer formed on the graphene surface.

However, CA only provides limited macro structural information at the graphene-liquid interface. X-Ray reflectivity (XRR) is a rigorous and quantitative technique for probing structural features of nanofilms at buried interfaces [14-18] with sub-Ångström resolution. Previously, it has been used to study epitaxial graphene on SiC in air [19, 20] and in water [12]. In this chapter, synchrotron XRR has been used to investigate the graphene-water interface at different temperatures (25 - 60 °C), complemented by AFM imaging and contact angle measurements at room temperature (RT). In addition, the effect of phosphate buffered saline (PBS) on the graphene surface structure has also been probed, which lays a base for the interpretation of the XRR study on the interaction between liposomes and graphene (Chapter 5). This was motivated by a previous report that soaking graphene in water for 24 h facilitated lipid *bilayer* formation in PBS solutions [21], instead of *monolayers* without soaking [22]. In this work, the structure of graphene was studied by XRR before and after submergence in Milli-Q® water for 24 h.

4.2 Experimental

4.2.1 Materials

Graphene used in this study was purchased from the same supplier as that used in Chapter 3. In Chapter 3, the graphene is described as few layer graphene (FLG) as respect to it thickness of ~ 13.0 ± 1.0 Å. However, here the focus of discussion is on the surface chemistry of the graphene samples, where FLG (with 3 - 10 number of layers) has been considered and described as a type of graphene in previous research [2, 23]. Therefore, we describe the FLG as *graphene* in this and the following chapters. Ultrapure Milli-Q® water with resistivity of 18.2 MΩ cm and a total organic content (ToC) of 3 - 4 ppb at 25 ºC and 0.01 M PBS (0.0027 M KCl and 0.137 M NaCl, pH = 7.4, at 25 °C, Sigma-Aldrich®) were used for solution preparation.

4.2.2 Methods

Synchrotron XRR, AFM, and water CA measurements have been used to study the structure and the composition of commercially available graphene samples. The experimental setups of the techniques are given in Chapter 2.

To investigate the influence of submerging graphene in water on its surface structure, XRR curves were collected on graphene within 10 min after it was exposed to Milli-Q water, which was the time required for sample alignment. The graphene then remained submerged under water for a further 23 - 24 h before XRR measurements were made again. Subsequently, water was replaced by PBS, and the XRR curves were collected at 25 °C, 40 °C and 60 °C, after which the samples were cooled back to 25 °C to compare with the initial stage. As a control, bare graphene that had not been submerged in water was also measured in PBS at RT. Each heating and cooling step took ~ 10 min and ~ 20 min, respectively, with a further 10 min allowed for thermal equilibrium before the measurement was made.

A consideration for XRR measurements in aqueous media is the absorption of X-rays by water. The liquid thickness in the custom-designed XRR cell (*cf.* Figure 2.1) was 1 cm, permitting ~ 20% transmission at 14 keV X-ray energy, which is sufficient for XRR measurements [24].

Reflectivity curves with mild fringes were plotted as RQ^4 *vs.* Q instead of log$R$ *vs.* Q, as shown in Figure 4.1b and Figure 4.5a, to show more clearly the Kiessig fringes, since the

reflectivity decays roughly proportional to $\boldsymbol{Q}^{-4}$ above the critical edge [25]. In total, 12 XRR measurements on 3 graphene samples were studied in 2 separate synchrotron experiments, and the results shown below are representative of these measurements. The XRR curves collected from different graphene samples were reproducible.

4.3 Results and Discussion

4.3.1 XRR of the graphene-water interface

XRR data fitting used a Slab Model, with ρ_n, t_n, and $R_{a,n}$ the SLD, thickness, and roughness of the n^{th} slab/layer as defined in Figure 4.1a. This yielded fits ($\chi^2 < 0.0012$) for the reflectivity curves of the graphene samples in different conditions. Figure 4.1b shows example XRR curves for bare graphene in air (circles) and water (triangles), and the soaked graphene in water (squares), with the fitted reflectivity curves shown as continuous lines. The XRR intensity oscillations (Kiessig fringes [26]) damped (*i.e.* became less pronounced) in water compared to air due to reduced SLD contrast with graphene.

From the fitted SLD profile of graphene in air shown in Figure 4.1c, the interfacial structure of the sample consisted of a graphene layer (represented as **Gr** in Figure 4.1a) with a contaminant layer comprising graphene multilayers and PMMA residues atop. The latter layer exhibited a thickness $t_c = 11.8 \pm 1.2$ Å and an SLD $\rho_c = 9.80 \times 10^{-6}$ Å^{-2} [27]. After the injection of water or PBS in the XRR liquid cell (*cf.* Figure 2.1), the contaminant layer on the graphene sample seemed undetectable, substituted by a diffuse layer at the interface with an SLD profile which gradually increased from $\rho_d = \sim 6.7 \times 10^{-6}$ Å^{-2} to $\rho_{water} = 9.44 \times 10^{-6}$ Å^{-2} of the bulk water. The SLD of this diffuse layer was smaller than that of graphene ($\rho_g = 18.20 \times 10^{-6}$ Å^{-2}) or PMMA ($\rho_{PMMA} = 10.81 \times 10^{-6}$ Å^{-2}), and was between that of air ($\rho_{air} = 0$ Å^{-2}) and water, whilst the high roughness $R_{a,d}$ (> 30 Å) value indicates a highly heterogenous interfacial structure (fitted values shown in Table 4.1). We suggest that this reduced SLD of the interfacial layer could be attributed to the formation of flattened air bubbles of nonuniform coverage on the graphene surface, as shown schematically in Figure 4.1a.

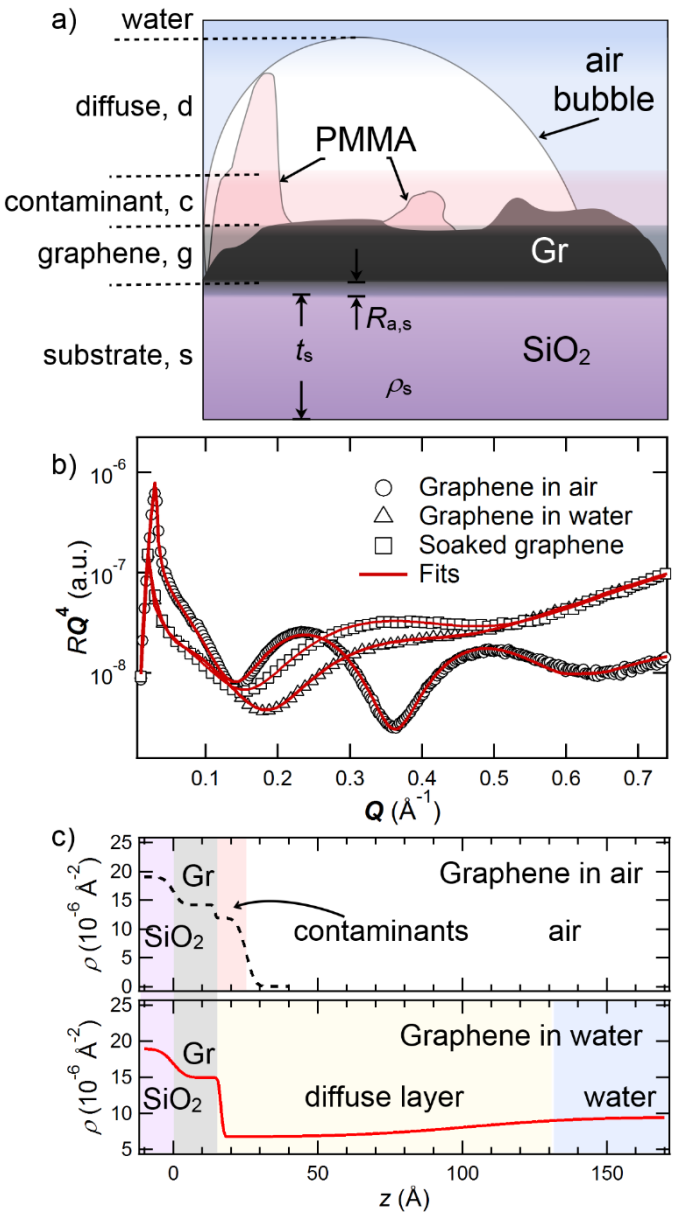

Figure 4.1. a) Physical model used to fit the XRR curves of graphene in water. b) The experimental (open symbols) and fitted (solid lines) XRR curves plotted as RQ^4 vs. Q for graphene in air (circles), in water (triangles), and 24 h-water soaked graphene (squares). The complete fitting parameters are listed in Table S6 in Appendix V). c) The fitted SLD ρ_n of the graphene sample in air (dashed line) and in water (solid line), plotted against z, the distance from the SiO_2 surface, with the SLD variations highlighted in different coloured regions across the interfaces of the graphene sample in air and in water. Each coloured region, with the width representing t_n, represents a modelled layer as defined in

a). The contaminant layer on graphene (represented as **Gr**) in air [27] is highlighted in pink, and a diffuse layer is present on the graphene in water.

To better address this observation, we have calculated the fraction of air in this diffuse layer (ϕ_{air}) from the fitted SLD of the diffuse layer (ρ_{mix}). The mixed SLD (ρ_{mix}) of a binary mixture can be calculated as,

$$\rho_{mix} = \phi_i \rho_i + (1 - \phi_i)\rho_j \,, \qquad \text{Equation 4.1}$$

where ϕ_i and ρ_i are the volume fraction and the SLD of constituent *i*, respectively. In this case, the diffuse layer was not strictly a binary mixture, instead, it had a more complicated structure consisted of graphene multilayers, PMMA residues, air, and water, as shown schematically in Figure 4.1a. However, if we assume the diffuse layer is composed by two segments: a bubble layer (with ρ_b and t_b) that was comprised by air and water and a contaminant layer (with ρ_c and t_c, which were obtained from the fitted XRR data of bare graphene in air), and assume that the fraction of the contaminant layer ϕ_c equals to the ratio of its thickness t_c and the thickness of the diffuse layer t_d, the SLD of the bubble layer ρ_b can be the calculated from can be obtained from Equation 4.1. Once ρ_b was obtained, ϕ_{air} could then be calculated, as the SLD of water and air were both known. The calculated ϕ_{air} is ~30 % as shown in Table 4.1.

Such an SLD reduction has been previously observed on a rough polystyrene surface [28]. Further AFM imaging suggested that this diffuse layer was a consequence of both the contaminant and the air bubbles present on the surface [29].

Table 4.1. Fitting parameters for the XRR data collected from graphene in air, in water, in PBS, and 24 h water-soaked graphene in water at 25 ºC.

Sample	**Layers in the Slab Model**	t_n **(Å)**	ρ_n **(10^{-6} Å^{-2})**	$R_{a,n}$ **(Å)**	ϕ_{air} **(%)**	χ^2 **(10^{-3})**
Graphene in air at 25°C	Contaminants	10.8	11.87	2.4	100	1.11
	Graphene	14.4	14.13	0.4		
	SiO_2	3000	19.01	2.4		
Graphene in water at 25°C	Diffuse layer	84.9	6.72	31.9	36.7	0.47
	Graphene	16.5	14.93	0.7		
	SiO_2	3000	18.91	3.4		
Graphene in PBS at 25 °C	Diffuse layer	118.3	6.75	49.3	30.9	0.71
	Graphene	15.4	19.71	4.5		
	SiO_2	3000	18.91	3.5		
Soaked graphene in water at 25°C	Ion adsorbed layer	10.1	19.45	1.0	0	0.19
	Graphene	5.0	14.91	2.3		
	silanol	78.9	21.32	4.6		
	SiO_2	3000	18.96	69.7		

4.3.2 AFM imaging at the graphene-water interface

AFM topological images (Figure 4.2a) have also been collected to reveal the morphology of the graphene-water interface and were processed using the *NanoScope Analysis* software. The topological image of the graphene sample in air was comprised of the SiO_2 substrate, graphene, and the defects (marked as 1, 2, 3 in Figure 4.2a-b) that consisted of PMMA and multilayer graphene flakes [27] (*cf.* Figure 3.2c). A water droplet of ~ 5 mm in size was then displaced to create the aqueous environment. In water, the graphene surface became rougher as shown in the section profile (Figure 4.2b). A larger elevated area (4 in Figure 4.2a), which is most likely to be described as a nanobubble was observed.

However, it was a lot more challenging to obtain good quality, reproducible images under water, which is probably ascribable to a more complicated structure with inhomogeneous coverage. In addition, the presence of soft air bubbles could make it difficult for the AFM scanning tip to engage with surface. As a result, the AFM images of the graphene-water interface did not provide conclusive supporting evidence for the presence of the bubbles.

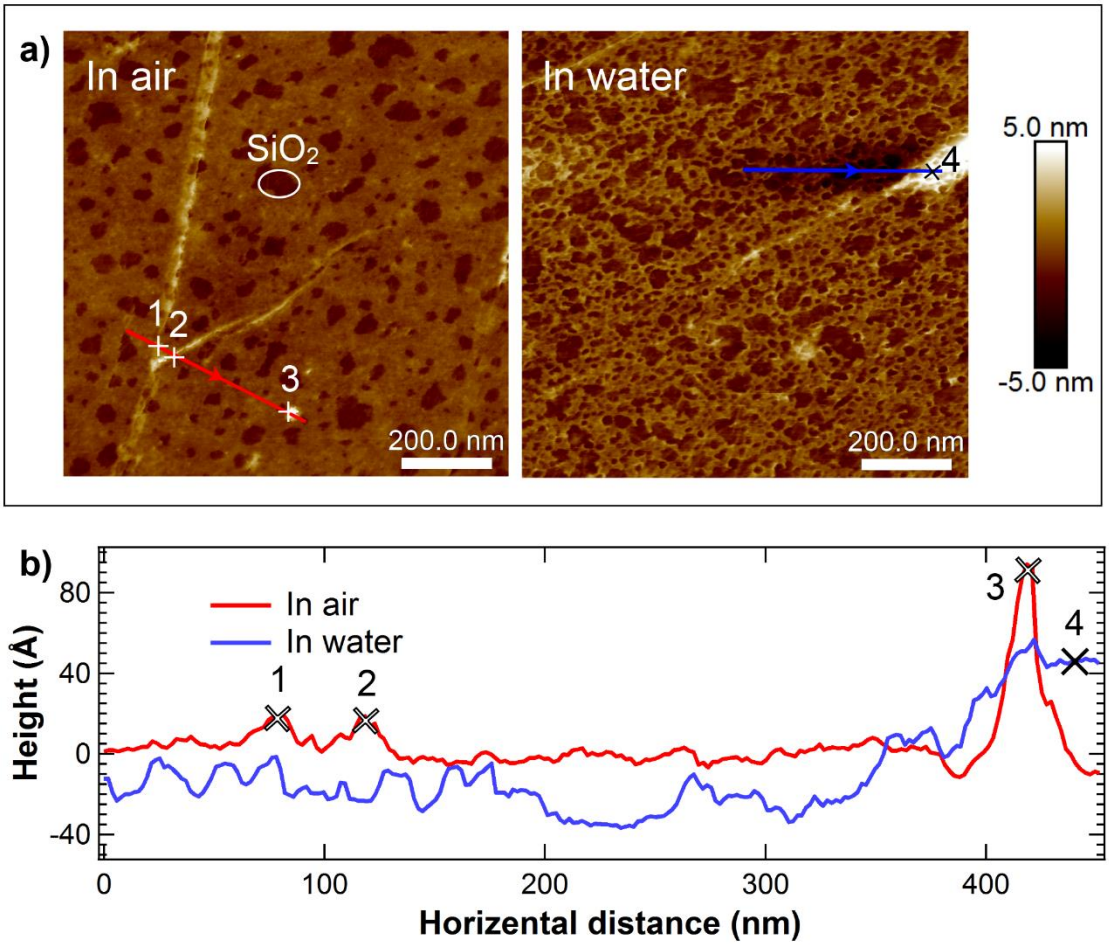

Figure 4.2. a) Example AFM topological images on a 1 μm × 1 μm area indicating graphene defects (1 and 2), PMMA residues (3), and air bubbles (4) on a continuous graphene layer with holes (white circle). b) Plotted line-profiles following the direction of the coloured arrow lines in a).

For the example under-water 3D image shown in Figure 4.3a, the maximum difference in the height, Δh_{max}, increased by ~ 11 Å compared to air (Table 4.2). Meanwhile, the graphene roughness given by the height deviation R_{ave} and height root-mean square R_{sq} also increased, consistent with a more inhomogeneous interface caused by the formation of air bubbles.

Table 4.2. The maximum difference in the relative height, Δh_{max}, the root-mean square average, R_{sq}, and the arithmetic average values of height deviations, R_{ave}, of the surface height deviations in the AFM topological images of graphene in air and in water following the plane fitting.

	Δh_{max} (Å)	R_{sq} (Å)	R_{ave} (Å)
In air	124	6.61	4.68
In water	135	10.8	8.37

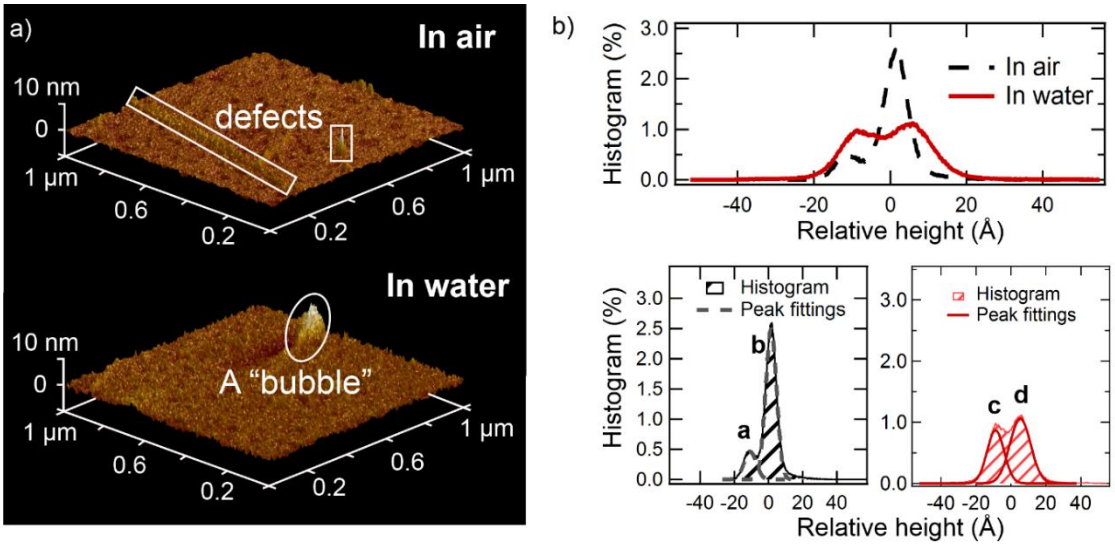

Figure 4.3. a) Example AFM 3D topological images of graphene in air and in water, showing a possible bubble (indicated by an oval) appear after the adding of water; and b) the corresponding histograms of height distributions on the sample surface with the Gaussian peak fittings for the measurements in air (left) and in water (right).

It can be observed from the Gaussian peak fittings shown in Figure 4.3b that the height distribution on the solid-water interface (with FWHM values of peaks **c** and **d** 11.5 Å and 10.6 Å, respectively) was broader than that at the air-water interface (with peaks **a** and **b** possessing FWHM values 8.4 Å and 7.5 Å, respectively), suggesting the existence of more inhomogeneous structures on the graphene-water interface compared to air. Particularly, as indicated by an oval in Figure 4.3a, a bubble-like area of size ~ 189 nm (length) × 88 nm (width) × 10 nm (height) was detected. The air bubble layer from XRR

fitting (*cf.* Table 4.1) has a smaller thickness (t_d = 84.9 Å) but a higher roughness ($R_{a,d}$ = 31.9 Å). One possible reason for the differences is that the XRR measures and thus gives the average value of a surface layer over a much larger footprint (~ 255 μm × 1 cm), whilst AFM measures a much smaller sample area (~ a few μm^2) and thus reflects a much more localized structure [27]. It should be borne in mind that a more complex structure could be present on graphene, including residual PMMA contaminants and graphene multilayers, which could not be distinguished by topological images only. Although AFM imaging did not provide conclusive topography information on graphene under water, it indicated that the interfacial structure was different from that in air. It was also qualitatively consistent with the XRR results which were indicative of an inhomogeneous interface. Further effort with AFM imaging remains a focus of our future work.

4.3.3 Effect of submerging CVD graphene on Si/SiO_2 under water

The sessile drop water contact angles (CAs) of graphene before and after soaking graphene in water for 24 h are shown in Figure 4.4b. For the soaked graphene samples, the water residues were removed by two methods: drying naturally or using an Ar flow to dry the surface gently. A noticeable reduction of graphene water CA was observed with both methods. The results (described in detail in Appendix III,

Table S4) showed that the water CA on graphene decreased from 84.9 ± 0.4° to 55.6 ± 0.4° after it had been submerged under water for 24 h, indicating that the graphene sample became more hydrophilic. Whether graphene is hydrophobic or hydrophilic is still somewhat controversial in the literature. Graphene was once believed to have similar wettability to graphite (water CA = ~ 80 - 100°), while some CA measurements suggested it was hydrophobic, and even superhydrophobic [23]. More recent studies showed that the interaction between water and graphene was affected by the graphene surface structure and related parameters, such as the graphene layer thickness [12, 30], the presence of defects [12, 23] and adsorbates [13, 23], underlying substrates [31], and the doping of graphene [32]. Both the surface energy and the topological features should contribute to the observed wettability of such a heterogeneous material. Thus, it is possible that graphene hydrophobicity reflects its various surface roughness and related chemical inhomogeneities due to different fabrication methods [23, 30].

It has been reported that trapped air bubbles could form at the solid-liquid interface particularly when nanotextures or multi-scale roughness were present at the interface, resulting in the Cassie–Baxter wetting state, which would then lower the solid-liquid adhesion and manifest in apparent higher hydrophobicity [33, 34]. If water permeates the surface textures, transforming the wettability from the Cassie-Baxter state to the Wenzel state [35], the hydrophobicity of the material would decrease, consistent with our observation of the decreased CA after 24 h water submergence. In addition, the SLD profile in Figure 4.4a indicates that no diffuse air-bubble layer was present on top of graphene after water-soaking, and that water had fully spread on the surface, as shown schematically in Figure 4.4c. The fitted graphene thickness $t_{g(water)}$ = 5.0 Å with ρ_g = 14.91×10^{-6} Å^{-2}, decreased appreciably after soaking, compared with the graphene thickness $t_{g(air)}$ = 14.4 Å detected in air. In the meantime, an additional layer appeared, with a higher SLD $\rho_a = 19.5 \times 10^{-6}$ Å^{-2}, and thickness t_a = 10.1 Å. The total thickness $t_{total} = t_{g(water)} + t_a$ = 15.1 Å is very similar to $t_{g(air)}$, and we attributed this observation to the adsorption of ions within the defect structures on graphene, which will be discussed below in section 4.3.4.

Furthermore, the SLD of the underlying substrate increased from $\rho_s = 18.91\times10^{-6}$ Å^{-2} before water soaking, a value matching the theoretical SLD of SiO_2, to $\rho_s = 21.32\times10^{-6}$ Å^{-2} after soaking (*cf.* Table 4.1). We attributed this to the formation of $Si(OH)_x$ by the rehydration of the amorphous silica, as the SLD of silanol is $\rho = 28.72 \times 10^{-6}$ Å^{-2}. Water

molecules can permeate through graphene lattices and interact with the silica substrate [36], leading to a higher electron density due to the formation of hydroxyl groups on the surface. The silica substrate is usually stable in water, and the formation of a silanol layer is not considered in most of the cases, because of the low diffusion rate of water molecules (only 6 Å per 1000 min at 25 ºC) in bulk silica. However, molecular diffusion can be accelerated by increasing temperature [37]. We thus postulate that the prolonged submergence of the sample in water and subsequent increased temperature during XRR measurements led to the formation of detectable silanol groups.

The fitted thickness of the silanol layer is t_s = ~ 75 Å, a value much higher than the theoretical one (8.64 Å after soaking in water for 24 h [37]), and the ρ_s profile also decreased gradually towards the bulk silica. Meanwhile, the fitted roughness of the silica substrate is also high $R_{a,silica}$ = ~ 65 Å. It is possible for water to penetrate the amorphous silica, leading to a relatively thick and rough interfacial layer. The observation of this silanol layer underneath graphene has important implications, as the acidity of silanol could lead to high affinity for ions and biomolecules [38]. It has also been reported that the presence of silanol on the SiO_2 substrate underlying graphene could change the electric properties of graphene, due to the electric dipoles possessed by the adsorbed water [39].

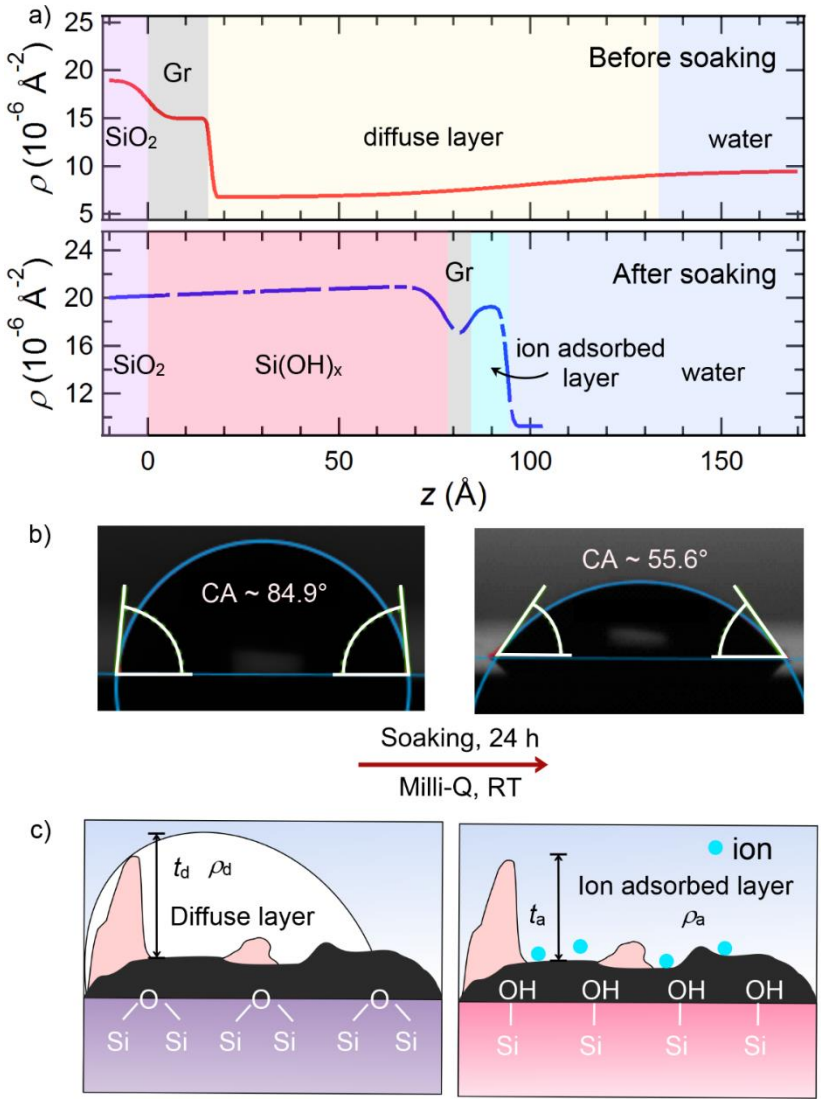

Figure 4.4. a) Fitted XRR SLD profiles in water of the un-soaked graphene (red solid line) and soaked graphene (blue dashed line), with the coloured regions representing different layers in the Slab Model used to fit the data. b) The water CA = 84.9º of a bare graphene sample reduced to CA = 55.6º after soaking in Milli-Q for 24 h. The diminishing of the air bubble layer, the hydration of the SiO_2 substrate, and the formation of the ion adsorbed layer upon soaking are schematically illustrated in (c).

4.3.4 Effect of temperature and PBS on CVD graphene on Si/SiO$_2$

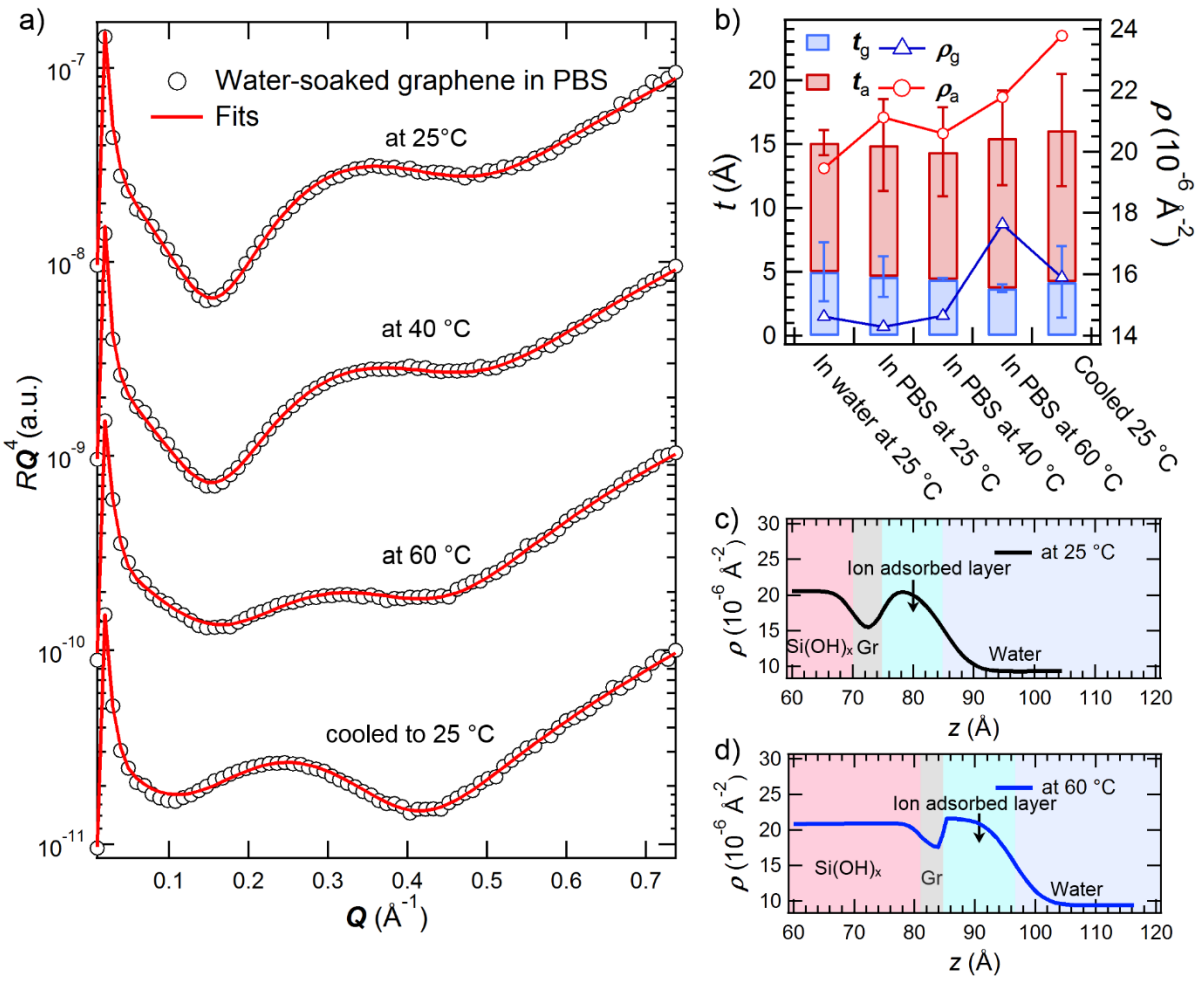

Figure 4.5. a) The experimental (open circles) and fitted (solid lines) XRR curves (offset vertically for clarity) of water-soaked graphene in PBS at different temperatures, with the fitting parameters (t_n, ρ_n and $R_{a,n}$) tabulated in Table S6. The fits show that the graphene thickness t_g remained at ~ 4.2 Å at all temperatures; while its SLD was relatively constant at ρ_g ~ 15 × 10^{-6} Å^{-2} at lower temperatures, it increased to ρ_g = 17.6 × 10^{-6} Å^{-2} at 60 °C. Similarly, the SLD and thickness of the ion adsorbed layer ρ_a and t_a increased at 60 °C, and the increment remained after cooling back to RT as shown in b). The SLD profiles of graphene samples at 25 °C and 60 °C are shown in (c) and (d), respectively, which show that the thickness of the silanol layer also increased at 60 °C, with the interface between graphene and the ion adsorbed layer becoming smoother.

Figure 4.5a shows XRR curves of water-soaked graphene in PBS, at 25 °C, 40 °C, 60 °C, and then cooled back down to 25 °C. The change in the Kiessig fringes is noticeable upon heating and cooling, and the XRR profiles are also different from those in pure water (*cf.*

Figure 4.1c). The fitting parameters and SLD profiles for these XRR curves are given in Table S6 and Figure S6 in Appendix V, respectively. The thickness t_a and SLD ρ_a of the ion adsorbed layer atop graphene (as illustrated in Figure 4.4c in section 4.3.3) increased after water was replaced with PBS at RT. In addition, as listed in Table 4.1, the fitted SLD value $\rho_g = 19.17 \times 10^{-6}$ Å^{-2} of un-soaked graphene is also higher in PBS than that in air ($\rho_g = 14.93 \times 10^{-6}$ Å^{-2}). This again is consistent with the assumption of ion adsorption on graphene. It has been shown by molecular dynamics simulations that graphene could attract, due to π-conjunction and polarizability, both cations [40-42] and anions [43, 44], such as Na^+ ($\rho = 86.75 \times 10^{-6}$ Å^{-2}) and K^+ ($\rho = 55.06 \times 1\ 0^{-6}$ Å^{-2}) in PBS to the graphene-water interface. Furthermore, the fitted SLD profiles to the XRR curves of the soaked graphene in PBS at 25 °C (Figure 4.5c) and 60 °C (Figure 4.5d) also show that ion adsorption was promoted upon heating. The thickness and SLD of the ion adsorbed layer increased to $t_a = 11.8$ Å, and $\rho_a = 21.8 \times 10^{-6}$ Å^{-2}, with respective increment $\Delta\rho_a = 0.7 \times 10^{-6}$ Å^{-2} and $\Delta t_a = 1.5$ Å compared with 25 °C), whilst the graphene thickness $t_g = 4.2$ Å (*cf.* the theoretical thickness of a monolayer graphene of 3.35 Å) remained constant, with the fitted SLD in PBS $\rho_g = \sim 15 \times 10^{-6}$ Å^{-2} also comparable to that in air.

The interfacial roughness $R_{a,g}$ between graphene and the ion adsorbed layer decreased at higher temperatures (Figure 4.5b), which could be due to the ions residing in the defects and on the contaminants of the graphene surface and reducing the apparent roughness. The thickness t_s of the silanol layer also increased upon heating (Figure 4.5d), thereby promoting ion adsorption to the substrate [38]. The effect of temperature on the ion adsorption can be triggered by the enhanced mobility of ions at higher temperatures [45]. In addition, the structure of graphene itself can also play an important role in response to the temperature-dependent ion adsorption. A simulation study has reported that water could form an ice-like double layer structure on free standing graphene, preventing the interaction between graphene and the bulk solution [13]. This interfacial water structure was found disrupted at 340 K (67 °C), which is close to where we observed enhanced ion adsorption.

4.4 Conclusions

In this study, we have applied synchrotron XRR to characterise the surface structure of graphene in water and PBS. The surface structure of graphene submerged under water for 24 h was also studied. AFM imaging provided inconclusive topological morphology of

graphene under water, due to the intrinsic experimental difficulties associated with the technique while imaging a soft, bubble-covered surface. The surface roughness data however was consistent with a much more inhomogeneous graphene-water interface compared to air. Fitting the SLD to the XRR curves on graphene indicated the presence of an air bubble layer (ρ_d = 6.72×10^{-6} Å^{-2}, t_d = 84.9 Å, and $R_{a,d}$ = 31.9 Å) on top of graphene when firstly immersing it in water. AFM imaging also revealed the presence of isolated bubbles (*e.g.* ~189 nm (length) × 88 nm (width) × 10 nm (height)) on graphene. These bubbles of a few nm in height with a flattened morphology diminished after the graphene sample was submerged under water for a prolonged period. Concurrently, the water contact angle on graphene decreased from 84.9±0.4° (before soaking) to 55.6±0.4° (after soaking), indicating a decrease in its hydrophobicity, which is consistent with the XRR evidence for the diminishment of the air bubble layer. XRR results also suggested that, after water soaking, a silanol layer formed on the SiO_2/Si substrate, which could alter the electric properties of the graphene/silica sample [39]. Furthermore, ion adsorption was inferred from the increased SLD of the layer atop graphene observed on water-soaked graphene in PBS, with the fitted interfacial structure consisting of an additional ion adsorbed layer. The ion adsorption was enhanced by heating the solution to 60 ºC, which was retained after cooling. We attributed this change to the higher ion mobility, the higher ion affinity of the formed silanol layer on the substrate, and the disruption of the ordered water structure at high temperatures as reported previously [13]. These unprecedented results are relevant to bioanalytic and nanotechnological applications of graphene in which its structure at the interface between water and electrolyte solutions is an important consideration to the efficacy and functionality of the devices or the processes. The capability of XRR to detect the air bubbles exist on the hydrophobic interfaces can be also utilized on examining the wettability of a surface with sub-micrometer precision, compared with CA measurements that only provide the bulk wetting.

References

1. Leenaerts, O., Partoens, B., and Peeters, F.M., *Adsorption of H(2)O, NH(3), CO, NO(2), and NO on graphene: a first-principles study.* Physical Review B, 2008. **77**(12): p. 125416.
2. Melios, C., et al., *Water on graphene: review of recent progress.* 2D Materials, 2018. **5**(2): p. 022001.
3. Wang, Y., et al., *Graphene and graphene oxide: biofunctionalization and applications in biotechnology.* Trends in Biotechnology, 2011. **29**(5): p. 205-212.
4. Xu, M.S., et al., *Auger electron spectroscopy: a rational method for determining thickness of graphene films.* Acs Nano, 2010. **4**(5): p. 2937-2945.
5. Jang, W.Y., et al., *Thickness-dependent thermal conductivity of encased graphene and ultrathin graphite.* Nano Letters, 2010. **10**(10): p. 3909-3913.
6. Rutter, G.M., et al., *Scattering and interference in epitaxial graphene.* Science, 2007. **317**(5835): p. 219-222.
7. Aitken, Z.H. and Huang, R., *Effects of mismatch strain and substrate surface corrugation on morphology of supported monolayer graphene.* Journal of Applied Physics, 2010. **107**(12): p. 123531.
8. Robertson, A.W., et al., *Spatial control of defect creation in graphene at the nanoscale.* Nature Communications, 2012. **3**: p. 1144.
9. Banhart, F., Kotakoski, J., and Krasheninnikov, A.V., *Structural defects in graphene.* Acs Nano, 2011. **5**(1): p. 26-41.
10. Lin, Y.C., et al., *Graphene annealing: how clean can it be?* Nano Letters, 2012. **12**(1): p. 414-419.
11. Ni, Z.H., et al., *On resonant scatterers as a factor limiting carrier mobility in graphene.* Nano Letters, 2010. **10**(10): p. 3868-3872.
12. Zhou, H., et al., *Understanding controls on interfacial wetting at epitaxial graphene: experiment and theory.* Physical Review B, 2012. **85**(3): p. 035406.
13. Akaishi, A., Yonemaru, T., and Nakamura, J., *Formation of water layers on graphene surfaces.* Acs Omega, 2017. **2**(5): p. 2184-2190.

14. Briscoe, W.H., et al., *Applying grazing incidence X-ray reflectometry (XRR) to characterising nanofilms on mica.* Journal of Colloid and Interface Science, 2007. **306**(2): p. 459-463.

15. Speranza, F., et al., *Quiescent bilayers at the mica-water interface.* Soft Matter, 2013. **9**(29): p. 7028-7041.

16. Sironi, B., et al., *Structure of lipid multilayers via drop casting of aqueous liposome dispersions.* Soft Matter, 2016. **12**(17): p. 3877-3887.

17. Wlodek, M., et al., *Interfacial and structural characteristics of polyelectrolyte multilayers used as cushions for supported lipid bilayers.* Soft Matter, 2017. **13**(43): p. 7848-7855.

18. Dane, T.G., et al., *Structured oligo(aniline) nanofilms via ionic self-assembly.* Soft Matter, 2012. **8**(10): p. 2824-2832.

19. Conrad, M., et al., *Structure and evolution of semiconducting buffer graphene grown on SiC(0001).* Physical Review B, 2017. **96**(19): p. 195304.

20. Emery, J.D., et al., *Structural consequences of hydrogen intercalation of epitaxial graphene on SiC(0001).* Applied Physics Letters, 2014. **105**(16): p. 161602.

21. Ang, P.K., et al., *A bioelectronic platform using a graphene-lipid bilayer interface.* Acs Nano, 2010. **4**(12): p. 7387-7394.

22. Yamazaki, K., Kunii, S., and Ogino, T., *Characterization of interfaces between graphene films and support substrates by observation of lipid membrane formation.* Journal of Physical Chemistry C, 2013. **117**(37): p. 18913-18918.

23. Ashraf, A., et al., *Spectroscopic investigation of the wettability of multilayer graphene using highly ordered pyrolytic graphite as a model material.* Langmuir, 2014. **30**(43): p. 12827-12836.

24. Briscoe, W.H., et al., *Synchrotron XRR study of soft nanofilms at the mica-water interface.* Soft Matter, 2012. **8**(18): p. 5055-5068.

25. Porod, G., *Die Röntgenkleinwinkelstreuung von dichtgepackten kolloiden systemen.* Kolloid-Zeitschrift and Zeitschrift Fur Polymere, 1951. **124**(2): p. 83-114.

26. Als-Nielsen, J. and McMorrow, D., *Elements of modern X-ray physics*. 2011, Wiley,: Hoboken. p. xii, 419 pages.

27. Zhou, L., et al., *Surface structure of few layer graphene.* Carbon, 2018. **136**: p. 255-261.

28. Howse, J.R., et al., *Adsorbed surfactant layers at polymer/liquid interfaces: a neutron reflectivity study.* Physical Chemistry Chemical Physics, 2001. **3**(18): p. 4044-4051.

29. Steitz, R., et al., *Nanobubbles and their precursor layer at the interface of water against a hydrophobic substrate.* Langmuir, 2003. **19**(6): p. 2409-2418.

30. Melios, C., et al., *Effects of humidity on the electronic properties of graphene prepared by chemical vapour deposition.* Carbon, 2016. **103**: p. 273-280.

31. Rafiee, J., et al., *Wetting transparency of graphene.* Nature Materials, 2012. **11**(3): p. 217-222.

32. Ashraf, A., et al., *Doping-induced tunable wettability and adhesion of graphene.* Nano Lett, 2016. **16**(7): p. 4708-4712.

33. Tuteja, A., et al., *Designing superoleophobic surfaces.* Science, 2007. **318**(5856): p. 1618-1622.

34. Nosonovsky, M. and Bhushan, B., *Superhydrophobic surfaces and emerging applications: non-adhesion, energy, green engineering.* Current Opinion in Colloid & Interface Science, 2009. **14**(4): p. 270-280.

35. Sbragaglia, M., et al., *Spontaneous breakdown of superhydrophobicity.* Physical Review Letters, 2007. **99**(15): p. 156001.

36. Wehling, T.O., Lichtenstein, A.I., and Katsnelson, M.I., *First-principles studies of water adsorption on graphene: the role of the substrate.* Applied Physics Letters, 2008. **93**(20): p. 202110.

37. Doremus, R.H., *Internal hydroxyl groups near surface of silica.* Journal of Physical Chemistry, 1971. **75**(20): p. 3147-3148.

38. Hassanali, A.A. and Singer, S.J., *Model for the water-amorphous silica interface: the undissociated surface.* Journal of Physical Chemistry B, 2007. **111**(38): p. 11181-11193.

39. Sabio, J., et al., *Electrostatic interactions between graphene layers and their environment.* Physical Review B, 2008. **77**(19): p. 195409

40. Sun, M.L., et al., *First-principles study of the alkali earth metal atoms adsorption on graphene.* Applied Surface Science, 2015. **356**: p. 668-673.

41. Bostwick, A., et al., *Quasiparticle dynamics in graphene.* Nature Physics, 2007. **3**(1): p. 36-40.

42. Malyi, O.I., et al., *A computational study of Na behavior on graphene.* Applied Surface Science, 2015. **333**: p. 235-243.

43. McCaffrey, D.L., et al., *Mechanism of ion adsorption to aqueous interfaces: graphene/water vs. air/water.* Proceedings of the National Academy of Sciences of the United States of America, 2017. **114**(51): p. 13369-13373.

44. Shi, G.S., Ding, Y.H., and Fang, H.P., *Unexpectedly strong anion-p interactions on the graphene flakes.* Journal of Computational Chemistry, 2012. **33**(14): p. 1328-1337.

45. Tabrizchi, M. and Rouholahnejad, F., *Comparing the effect of pressure and temperature on ion mobilities.* Journal of Physics D-Applied Physics, 2005. **38**(6): p. 857-862.

Chapter 5

Adsorption morphology of lipids on graphene surface

(A manuscript is under preparation based on the results described in this chapter.)

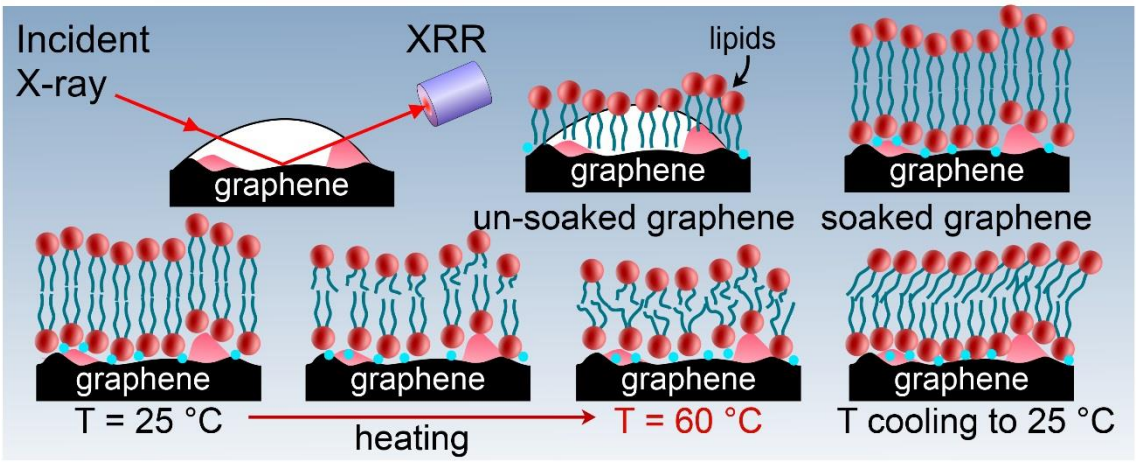

Graphene has shown its potential as bio-sensing devices, but its cytotoxicity restricts its applications. One method to solve the biocompatibility issue is to functionalise graphene with biomolecules such as lipids. Therefore, understanding the adsorption of lipids on graphene becomes crucial. In this study, we have applied synchrotron X-ray reflectivity (XRR) to investigate the interaction between the CVD graphene on Si supports (with 300 nm SiO_2 layer) and the 1,2-dioleoyl-sn-glycero-3-phosphocholine (DOPC) or 1,2-dipalmitoyl-sn-glycero-3-phosphocholine (DPPC) liposomes. The adsorption morphologies of DOPC and DPPC was compared at different temperatures (at 25 °C, 40 °C, 60 °C and cooling to 25 °C), and on graphene that had or had not been processed with water submergence. The results suggested the fusion of liposomes on graphene in phosphate buffered saline, but not in Milli-Q, which could be a result of the electrostatic repulsion between the liposomes and graphene. Both DOPC and DPPC have been observed to form monolayers on the un-soaked graphene, but bilayers on the soaked graphene, due to the increased graphene hydrophilicity after soaking. Our results provide a new understanding on the morphology of lipid membranes on graphene and proved the capability of XRR to probe the surface and interfacial structures of graphene coated with biomolecules.

5.1 Introduction

Graphene has gained wide interests since its discovery, especially for applications such as drug delivery and bio-sensing [1, 2]. Its unique structure brings special physical and chemical properties that benefit its usage in biological areas: the tailorable hydrophilicity from surface functionalization provides chances for graphene to adsorb various biomolecules, the large surface area provides graphene with abundant reactive regions to interact with biomolecules, and its special electronic properties (for example charge carrier density and mobility) that are sensitive to the surrounding environments enable graphene to detect the adsorption of different biomolecules [1-7]. Although graphene is promising in bionanotechnology, there are still obstacles to overcome before its actual application, and the bio-incompatibility issue is one of them, as described in section 1.3. Increasing numbers of studies have been carried out on the toxicity of graphene, not only on improving the biocompatibility of graphene, but also on utilizing graphene derivatives as antibacterial agents with comparatively mild cytotoxicity [8-10].

To enable the application of graphene *in vivo*, it becomes crucial to reduce its health risk. Based on the mechanism described in section 1.3, the interaction with cells can be influenced by the graphene properties such as functionalization, size, surface structure (*e.g.* roughness), and wettability [11]. Therefore, one path to increase the biocompatibility of graphene is to alter its physical properties, biological surface modification is one of the most studied methods. By encapsulating or coating graphene with biomolecules, the probability of graphene to contact biomolecules directly can be minimized, and one example that can be used to modify graphene is lipid [12]. The ability of graphene field-effect transistor (FET) coated with lipid membranes for use in biosensing has been determined, and the Dirac point of graphene remained, regardless of the adsorbed lipids [7, 13]. However, the morphology of the lipid adsorbed on graphene is still a controversy. Figure 5.1 illustrates 4 possible models of lipid or liposome adsorption on graphene [14], the formation of monolayer [13, 15, 16], bilayer [7, 15, 17], trilayer [18], and intact liposomes [13, 15] all have been observed, depending on the preparation method of the lipid layer and the graphene surface character. To be specific, on hydrophobic graphene surfaces, the hydrocarbon tails of lipids were found to attach to the graphene surface, forming monolayer and trilayer structures, whilst on graphene treated to have increased wettability, lipid bilayer membranes tend to form.

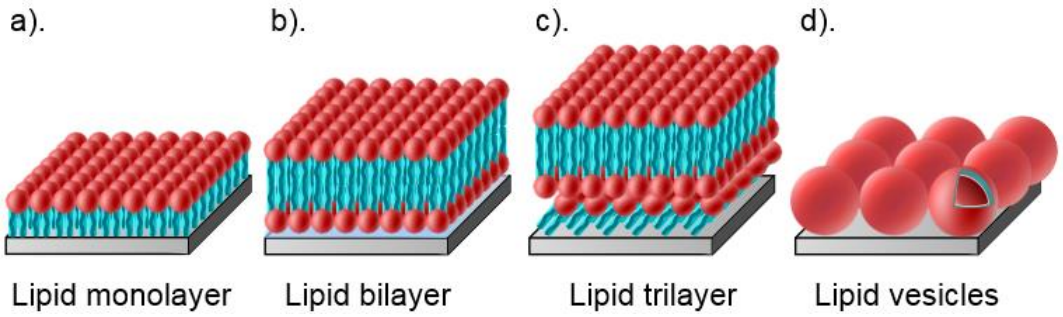

Figure 5.1. 4 models of the lipid adsorption morphologies on graphene that have been reported. Monolayers (a) and trilayers (with a tilted monolayer sandwiched between graphene and the lipid bilayer) (c) were observed to form on hydrophobic graphene, whereas bilayers were found to form with a trapped water layer sandwiched between the substrate and the membrane. Intact liposomes (d) were also detected in the primary stage after deposition.

The interaction between graphene and lipids had been investigated by various techniques. For instance, atomic force microscopy (AFM) [7, 17-19], internal reflection fluorescence correlation spectroscopy [7], and quartz crystal microbalance with dissipation monitoring technique [13, 15, 17] are among the most commonly used methods to investigate the deposition of biomolecules and the quality of the adsorbed membranes on graphene.

However, information provided by these methods is not sufficient when it comes to the study of the buried substrate interface. It is worthy to explore the new techniques to compensate the deficiency, and thus enhancing our understanding on the mechanism of the formation of lipid membranes with different morphologies atop graphene. X-Ray reflectivity (XRR), as mentioned in precious chapters, is a robust technique that can be used to monitor the structural change of materials *in situ* in different conditions on the interface [20, 21]. In this chapter, synchrotron XRR has been performed to probe the interactions between 1,2-dioleoyl-sn-glycero-3-phosphocholine (DOPC) and 1,2-dipalmitoyl-sn-glycero-3-phosphocholine (DPPC) liposomes and the graphene supports at different temperatures (25 - 60 °C). The influence of the wettability of graphene as well as the effect of ions (ions provided by phosphate buffered saline (PBS)) on the fusion of liposomes and the morphology of the adsorbed lipid membranes have been discussed. Our results provide useful information on the morphologies of lipid membrane formed on graphene from vesicle fusion, and the roles of ions and graphene surface structure in

this interaction, which could benefit the future studies on improving the biocompatibility of graphene *via* biofunctionalization.

5.2 Experimental

5.2.1 Materials

Chemical vapour deposited (CVD) graphene sheets on 1 cm × 1 cm silicon wafers with 300 nm oxide layer were purchased from the same supplier as those studied in Chapter 3 and Chapter 4. PBS with a pH of 7.4 at 25 °C, was purchased from Sigma Sigma-Aldrich®, DOPC and DPPC lipids (>99% purity) were purchased from Avanti® Polar Lipids. The structure, molecular formula and physical properties of the lipids are given in section 2.1.3, Figure 2.5 and Table 2.2. Ultrapure Milli-Q® water with resistivity of 18.2 MΩ cm and a total organic content (ToC) of ~ 3 ppb, chloroform ($CHCl_3$, ≥99.8%) from VWR Chemicals, and pressurised nitrogen from Air Liquide were used throughout the sample preparation.

5.2.2 Sample preparation

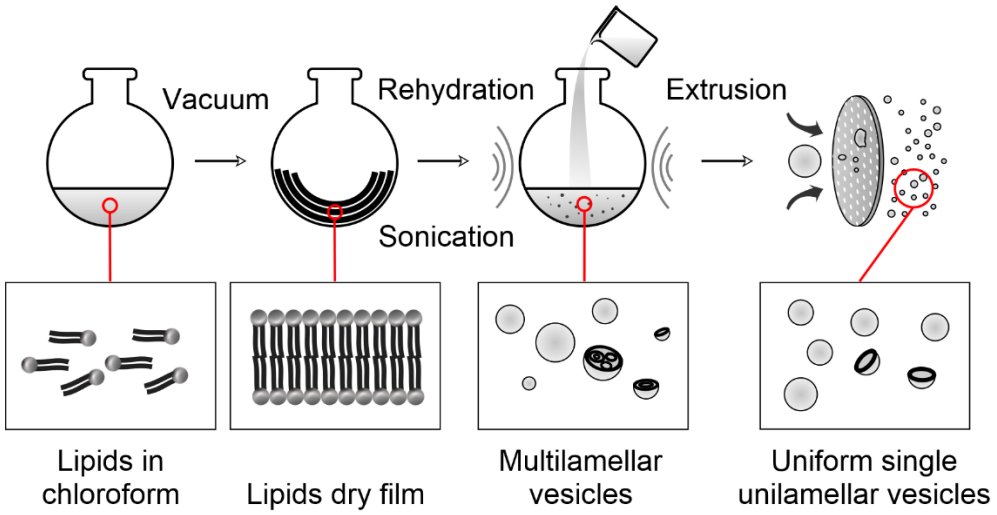

Figure 5.2. Illustration of the preparation procedure of the liposomes.

Phospholipid stock solutions in $CHCl_3$ (25 mg mL^{-1}) purchased from Avanti® Polar Lipids were used to make liposome suspensions without further purification. As shown schematically in Figure 5.2, unilamellar vesicles (ULV) were prepared from the conversion of multilayer vesicles (MLV) [22], the latter were obtained by rehydrating dry lipid films of stacked bilayers. The $CHCl_3$ solvents were firstly removed by N_2 flows to form a crystal-free lipid film in a 30 mL vial, which was then left in a vacuum oven to

dry solvent residues for 1 h. The used vials were cleaned in acid bath (10% HNO_4), washed with Milli-Q water, and dried before use. If crystallisation happened during the drying procedure, the lipid films would be dissolved in $CHCl_3$ and the drying procedure would be repeated until uniform lipid films were obtained. Milli-Q water or PBS were then added into the vial and sonicated for 30 min to make 2 mM MLV suspensions. In order to make ULV liposomes, the MLVs were sequentially extruded through polycarbonate membranes with 0.2 μm and 0.1 μm pore-size (Avanti® Polar Lipids Inc., Alabaster, Alabama), 8 times each, using a LIPEX™ 10 mL Thermobarrel Extruder (Northern Lipids Inc., Burnaby, Canada) under ~ 20 bar pressure provided by N_2. During the sample preparation, lipids were processes at a temperature at least 10 °C above their transition temperatures (T_m), which is T_m = - 17 °C [23, 24] for DOPC and T_m = 41 °C [25] for DPPC. The extruded liposome suspensions were diluted to 0.5 mM before being injected on the graphene surfaces. A lipid multilayer sample was prepared from drop casting DOPC liposome suspension (2 mM) in water on graphene, followed by drying in vacuum for 40 mins at room temperature (RT). The samples were kept in sealed containers at 4 °C before the experiments.

5.2.3 Dynamic light scattering

Prior to the measurement, the lipid concentration was diluted to 0.1 mg mL^{-1}, all measurements were performed at 25 °C with 120 s for equilibration. The DPPC dispersion in water was also measured at 55 °C after a 5-min thermal equilibration. The obtained data were then processed using the method described in section 2.5, and the average hydrodynamic diameter (D_z) of the studied DOPC and DPPC liposomes were ~ 120 nm and ~ 100 nm at 25 °C, respectively with a narrow size distribution (PDI < 0.1), as listed in Table S5 (Appendix IV).

5.2.4 X-Ray reflectivity

The graphene substrates were fixed by two small plates on a sample stage in the liquid chamber, where the soaking procedure of graphene and the incubation of liposomes were performed. Lipid membranes formed by vesicle fusion method in PBS and in water were studied at the liquid-solid interface (Figure 5.3), whilst the sample prepared by drop casting was studied at the air-solid interface. The measurements were taken on graphene that had or hadn't been soaked in Milli-Q water for 24 h at 25 °C, as our previous study suggested the wettability of graphene was promoted by the submergence procedure. This

was attributed to the presence of air bubbles on graphene, which could be removed simply by soaking in water, and the formation of a silanol ($Si(OH)_x$) layer atop the amorphous SiO_2 substrate. In the vesicle fusion method, the liposome suspensions were incubated on graphene sequentially at 25 °C, 40 °C and 60 °C. For the measurements conducted on the soaked graphene, the incubations at 60 °C were prolonged to 3 h, followed by cooling back to 25 °C and replacing the suspension by PBS for 5 times to remove excessive lipids or liposomes, XRR scans were performed about 10 min after each procedure and repeated until no changes were observed.

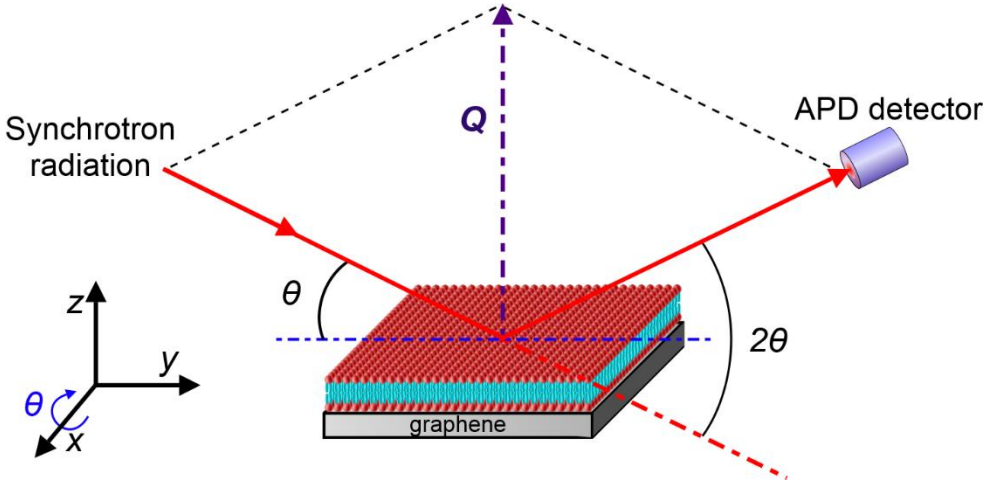

Figure 5.3. Schematic of the XRR setup with an incident synchrotron X-ray beam hitting the supported lipid bilayer (SLB), which generates specular reflections from the interfaces of the measured sample to the APD, where the data can be collected.

5.3 Results and Discussion

5.3.1 Influence of graphene wettability on the morphology of the adsorbed lipids

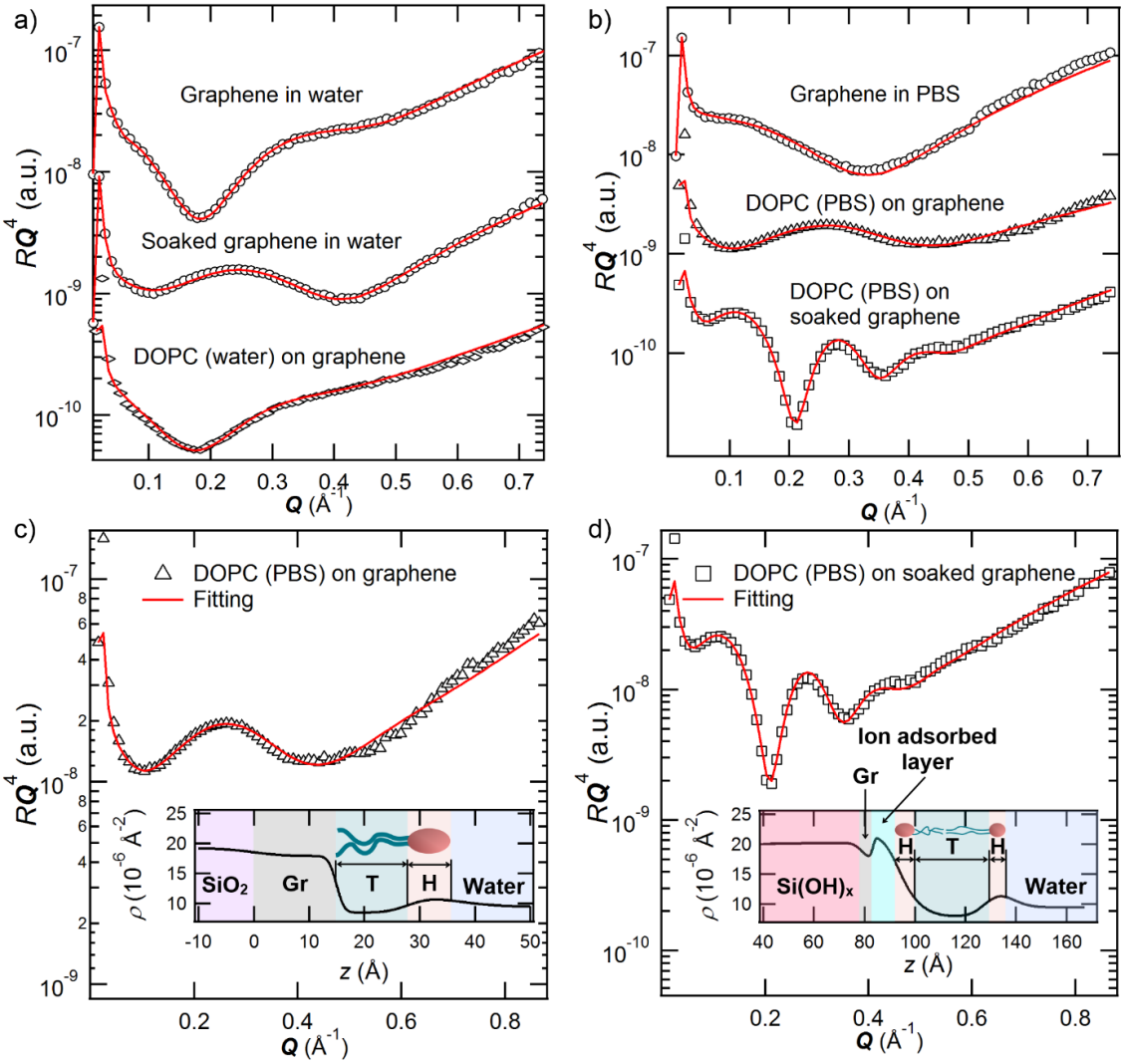

Figure 5.4. XRR data points (open markers) and the fittings (solid lines) of graphene incubated in DOPC suspensions in water (a) or in PBS (b), in comparison to the corresponding XRR curves of graphene in aqueous medias, plotted on RQ^4 against Q (with curves offset vertically for clarity). The fitted XRR curves of DOPC suspensions in PBS on un-soaked graphene and soaked graphene are shown in (c) and (d), respectively, with their SLD profiles shown as insets. On the SLD profiles, the modelled slabs are highlighted with different colours across the interfaces of the DOPC layer on graphene (Gr), with the DOPC structure divided to two regions: the headgroup (H) that possesses higher electron density and the hydrocarbon tail (T). The complete fitting parameters of the curves are listed in

Table S7 in Appendix V.

The XRR curves and fittings of the DOPC liposomes dispersed in water and PBS interacting with the soaked or un-soaked graphene are shown in Figure 5.4a and b, comparing to the bare graphene measured in water and PBS. These curves were collected at RT after the samples had been heated to 60 °C and rinsed with the respective solvents at RT as described in section 5.2.4. Due to the reduced SLD contrasts in water, the reflectivity intensity oscillations, which are also known as Kiessig fringes [26], became less pronounced. The reflectivity curves were therefore plotted as RQ^4 vs. Q, where R is the reflectivity intensity, to magnify the amplitude of the fringes, since the reflectivity decays roughly proportional to Q^{-4} above the critical edge [27]. Different lipid membrane morphologies on graphene have been observed by XRR depending on the incubating environment of the liposomes, and were concluded in

Table 5.1: no significant sign of lipid adsorption on the un-soaked graphene in water (even after incubating sequentially at 25 °C, 40 °C, 50 °C and 60 °C for at least 20 min at each temperature), whereas in PBS, the liposomes showed adsorption behaviour on both the un-soaked and soaked graphene substrates. Moreover, as revealed by the SLD profiles (*cf.* insets in Figure 5.4c and d), the DOPC liposomes in PBS ruptured and form supported monolayer and bilayer membranes on the un-soaked and soaked graphene, respectively. The SLD profiles shown in this study were derived from the corresponding simulated reflectivity curves, and are plotted against *z*, the relative vertical distance to the SiO_2 surface. To fit the data of the formed lipid monolayers on the un-soaked graphene, a 3-slab model has been used (Figure 5.4c), which consists of a graphene (Gr) layer, a lipid hydrocarbon tail (T) layer, and a phosphocholine (PC) headgroup (H) layer, in the order starts from the 300 nm SiO_2. For the fitting of lipid bilayer samples on the soaked graphene, an 8-slab model (Figure 5.4d) has been used, with an extra $Si(OH)_x$ layer presenting atop the SiO_2 substrate and an ion adsorbed layer between the graphene layer and the lipid membrane (a model based on our previous study). The structure of graphene underlying the adsorbed DPPC bilayers showed similarity upon temperature to the bare graphene, as shown in Figure 5.9, which consolidates the proposed slab structure. Also, in this model, the bilayer was separated to 4 sections: an inner headgroup layer (i-H), an inner tail layer (i-T), an outer tail layer (o-T), and an outer headgroup layer (o-H), so that the inner (proximal to the substrate) and outer (distal to the substrate) leaflets of could be considered separately, since they were reported to exhibit different thermodynamic behaviours because of the lipid-substrate interaction [25, 28].

It has been reported that the formation of lipid membranes on a solid support can be influenced by the properties of the substrate and the surrounding environments for a given liposome composition and size, and that the formation of the membrane on a support requires the adding of salts and a certain surface density of vesicles [14, 29]. Although various of intramolecular forces could maintain the adhesion of liposomes on graphene, the lack of liposomes attracted to graphene surface restricted the adsorption of vesicles and their fusion to membranes. Despite the fact that the PC lipids are zwitterionic, their liposomes exhibit a negative surface charge [30]. Similarly, CVD graphene on a silica substrate has also been estimated to be negatively charged, with the near graphene electrostatic potential between -10 mV to -15 mV [31]. Therefore, the interaction between the PC liposomes and graphene was limited in Milli-Q at low ionic strength, but increased

in PBS, as the electrostatic repulsions were screened by the added electrolytes [31], which is in agreement with our observation of the solvent selective membrane formation. An explanation for the formation of the different lipid membrane morphologies on graphene can be the increased hydrophilicity after soaking. Our previous study suggested that the wettability of graphene changed from slightly hydrophobic (water contact angle ~ 84.9°) to hydrophilic (water contact angle ~ 55.6°) simply after 24 h water submergence. This phenomenon was attributed to the presence of air bubbles trapped in the nanotextures on graphene, which diminished after soaking and the formation of silanol layer on the surface of silica substrate probed by XRR at the liquid-solid interface. Lipids tend to assemble into bilayer membrane on hydrophilic surface, but into monolayer membrane on hydrophobic surface [14, 15, 32]. Additionally, the hydrated silica underneath graphene could increase the affinity of the substrate to ions and to the PC group [33, 34], thus triggering the formation of lipid bilayer.

Table 5.1. Membrane morphologies formed on graphene in water or PBS.

lipid	solvent	substrate	lipid morphology
DOPC	water	un-soaked graphene	no adsorption
	PBS	un-soaked graphene	monolayer
		soaked graphene	bilayer
DPPC	PBS	un-soaked graphene	monolayer
		soaked graphene	bilayer

Similar membrane structures were detected on graphene with the deposition of DPPC liposomes in PBS (

Table 5.1). In the case of un-soaked graphene, for better fittings (shown in section 5.3.1 Figure 5.5b), an extra diffuse layer (air-bubble layer) with an SLD, ρ_d = ~ 4.5 × 10^{-6} Å^{-2} was applied in the slab model between the graphene layer and the DPPC layer (Figure 5.5d). The diffuse layer has a thickness t_d = ~ 26.3 Å and a roughness $R_{a,d}$ = ~ 23.3 Å, implying a highly heterogeneous interface. This is consistent with our slab model for the un-soaked bare graphene in water but with smaller ρ_d, t_d, and $R_{a,d}$, comparing to those parameters of the bare graphene, where ρ_d = 6.72 × 10^{-6} Å^{-2}, t_d = 84.9 Å, and $R_{a,d}$ = 31.9 Å. However, this thick diffuse layer was not observed in the case of DOPC, instead, at 25 °C, a very thin diffuse layer (ρ_d = 0.98 × 10^{-6} Å^{-2}, t_d = 2.5 Å, and $R_{a,d}$ = 0.0 Å) was obtained from the fitting, which would be better described as flattened air bubbles. Moreover, the fusion of DOPC liposomes on un-soaked graphene was only captured by XRR after heating to 40 °C without the detection of the thin diffuse layer (*cf.* Figure 5.5a and c), the influence of temperature will be discussed later in section 5.3.2. Despite of the different structures of the diffuse layer, the monolayer morphologies of the two lipids followed a similar scenario with the hydrocarbon tails attached to the graphene surface or in the air bubbles. This is probably why the thin diffuse layer became undetectable after the DOPC monolayer formed on graphene. It is also worth pointing out that the XRR measurements of DOPC and DPPC were conducted on graphene substrates produced in two different batches with different surface characters, which could lead to a different structure of the diffuse layer.

In terms of the bilayer structure formed on soaked graphene, the fitted parameters suggest a larger bilayer thickness, t_{bi}, of DPPC (t_{bi} = 49.4 Å) than that of DOPC (t_{bi} = 43.2 Å), as given in Table 5.2. Although the full length of the DOPC hydrophobic tails (C18:1) should be larger than the DPPC tails (C16:0), the compared measurements were collected at 25 °C, where DPPC tails should be fully extended in gel phase, whilst DOPC tails were fluid and disordered in the liquid crystalline phase. Consequently, it is conceivable that the DPPC exhibited a higher bilayer thickness. A summary of our fitted bilayer and monolayer lipid thickness compared with values obtained from literature is listed in Table 5.5 The fitted volume fractions of the lipid headgroups (ϕ_H) are larger than those of the tails (ϕ_T) for most of the samples, because of the larger distance between the two adjacent lipid headgroups than tails [24, 35], similar ϕ_H has been observed in previous neutron researches on SLB [36, 37]. Besides, the volume fraction discussed in this study of the considered molecule in the respective slab is calculated from an assumption that the lipid

layer was only comprised by lipids and water, ϕ_n could then be calculated from the fitted SLD of the mixture, using Equation 4.1 that was described earlier in section 4.3.1.

However, this method could be inaccurate if there were more than two components in the slab. For example, with air bubbles on the graphene surface, the coverage of the hydrocarbon tails of DOPC ($\rho_{DOPC,\,T} = 7.74 \times 10^{-6}$ Å^{-2}) and DPPC tail ($\rho_{DPPC,\,T} = 8.27 \times 10^{-6}$ Å^{-2} below 41 °C, $\rho_{DPPC,\,T} = 7.48 \times 10^{-6}$ Å^{-2} above 41 °C) could be overestimated, but that of the phosphocholine headgroup ($\rho_H = 14.52 \times 10^{-6}$ Å^{-2}) could be underestimated.

Table 5.2. Fitted bilayer structures of DPPC and DOPC formed on graphene. t_n, $R_{a,n}$, and ϕ_n denote the thickness, the roughness, and the lipid volume fraction of the n^{th} slab, respectively. The bilayers were prepared via vesicle fusion in PBS on the soaked graphene, and the data were collected at 25 °C after incubating at 60 °C for 3 h and rinsing with PBS at 25 °C.

	slab	t_n (Å)	$R_{a,n}$ (Å)	ϕ_n (%)
DPPC	o-H	8.9	7.0	41.0
	o-T	12.6	10.1	89.4
	i-T	20.2	0.0	90.9
	i-H	7.5	4.9	71.4
	bilayer	49.4		
DOPC	o-H	7.1	6.6	87.6
	o-T	15.7	5.0	88.9
	i-T	13.2	7.7	85.2
	i-H	7.3	6.5	73.9
	bilayer	43.2		

5.3.2 Influence of temperature on thickness and coverage of the lipid membrane

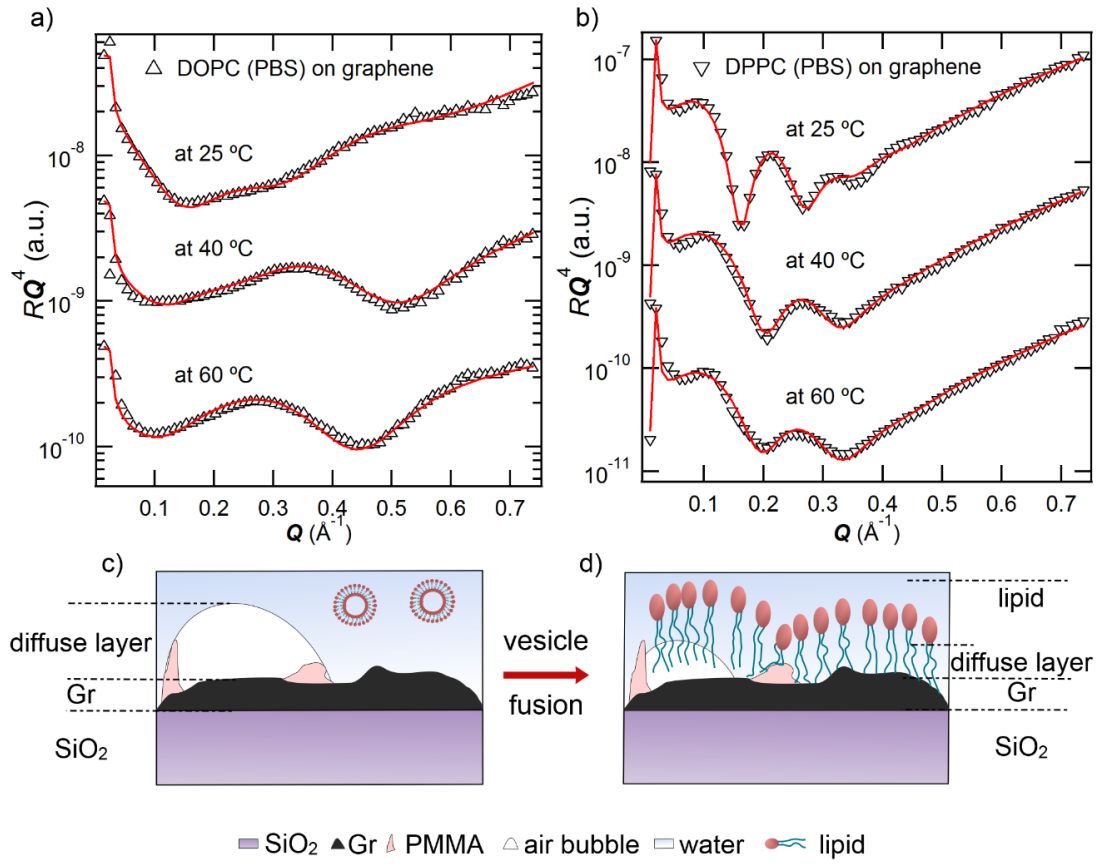

Figure 5.5. XRR data points (open markers) and the fittings (solid lines) of DOPC (a) and DPPC (b) liposomes suspended in PBS incubating on the un-soaked graphene at 25 °C, 40 °C, and 60 °C, plotted as RQ^4 against Q. The XRR curves collected at different temperatures were offset vertically for clarity. The fitted SLD profiles (*cf.* Figure 5.6) of the XRR curves in (a) and (b) suggest that both DOPC and DPPC liposomes have fused into monolayer membrane on un-soaked graphene. c) and d) illustrate the graphene surfaces before and after the vesicle fusion, respectively.

The XRR data of DOPC and DPPC liposomes in PBS solutions collected at the un-soaked interface are shown in Figure 5.5, along with the fits. The samples were investigated at different temperatures to study the influence of temperature on the lipid membrane morphologies. For DOPC, the periodical fringes on the reflectivity curves that show the formation of membrane structures were only observed on the measurements above 40 °C, while the DPPC monolayer on graphene could be at all measured temperatures. The adsorption of DOPC didn't take place during the initial measurement and the repeat at RT, which took about 20 min in total (*cf.* 5.2.2 Sample preparation). One can expect an

enhanced liposome fusion upon heating, since the possibility of vesicles approaching the graphene surface increases with temperature [38]. However, counting the time required by heating and alignment (incubating at 25 °C for 20 min, heating for 10 min, and incubating for 5 min at 40 °C before the scan), by the time when the measurement at 40 °C started, the DOPC liposomes had been injected into the liquid cell for 45 min. Therefore, the equilibrium of the adsorption procedure should also be taken into consideration for the observation of lipid monolayer. Unlike that of DOPC, the adsorption of DPPC liposomes on un-soaked graphene started at 25 °C. In principle, the formation of homogeneous lipid membranes should be more difficult when the lipid is in the gel phase, yet the vesicle fusion of DPPC liposomes into high quality SLBs on mica [25, 28, 36] at RT has been observed before. In fact, the fusion of DPPC has been reported to be favoured below its T_m, promoted by the structural defects that could reduce the potential barrier of the fusion procedure [38]. Our XRR fittings (*cf.*

and Table 5.4) also suggest that DPPC liposomes formed membranes on graphene below its T_m.

Except for assisting the liposome fusion on graphene, temperature was also found to have influence on the morphology of the formed lipid membranes on the un-soaked (

) and soaked graphene (Table 5.4), suggested by the fitted XRR parameters. Based on the slab model (*cf*. Figure 5.4c) described before, the SLD profiles (Figure 5.6a) of the DOPC samples showed a slight expansion at 60 °C in the hydrocarbon tail thickness, t_T, increasing from 10.9 Å at 40 °C to 13.6 Å, while the thickness of the headgroup held at around t_H = ~ 6.8 Å. Likewise, the hydrocarbon tail of DPPC mildly extended by Δt_T = 0.6 Å after heating from 40°C to 60 °C. The phase transition of the graphene-supported DPPC bilayer from gel to liquid-crystalline phase occurred before running the measurement at 40 °C, evident from the collapse of the DPPC tail layer from t_T = 18.9 Å at RT to t_T = 13.2 Å, with the roughness going up from $R_{a,H}$ = 4.5 Å to $R_{a,H}$ = 5.7 Å. In addition, the ϕ_T and ϕ_H calculated from Equation 4.1 for both DOPC and DPPC lipids decreased with the increasing temperature. This temperature triggered thinning behaviour of lipid membrane is consistent with previous researches on lipid bilayers [24, 39], and has also been captured for DOPC multilayers captured from XRR (Appendix V). The decreased ϕ_T, and ϕ_H could be attributed to promoted lipid mobility at higher temperature. However, it is also important to bear in mind that because of the presence of the diffuse

layer, the calculated ϕ_T generally was larger than the realistic. The trend of lipid structure obtained by the fitted monolayer results, therefore, is not conclusive.

Table 5.3. Fitted parameters of the lipid membranes for XRR curves shown in Figure 5.5. t_H, $R_{a,H}$, ϕ_H, and t_T, $R_{a,T}$, ϕ_T are the thickness, roughness, the coverage of the lipid headgroup (H) and hydrocarbon tails (T), respectively. The total thickness of the monolayer membrane is represented by t_{mono}.

sample		t_H (Å)	$R_{a,H}$ (Å)	ϕ_H (%)	t_T (Å)	$R_{a,T}$ (Å)	ϕ_T (%)	t_{mono} (Å)
DOPC in PBS	at 40 °C	6.8	3.3	52.2	10.9	2.5	90.8	17.7
	at 60 °C	6.7	3.6	41.9	13.6	2.0	60.6	20.3
DPPC in PBS	at 25 °C	7.3	2.8	77.3	18.9	4.5	93.6	26.2
	at 40 °C	6.7	1.9	51.9	13.2	5.9	90.6	19.9
	at 60 °C	6.7	4.0	30.9	13.8	6.4	85.0	20.5

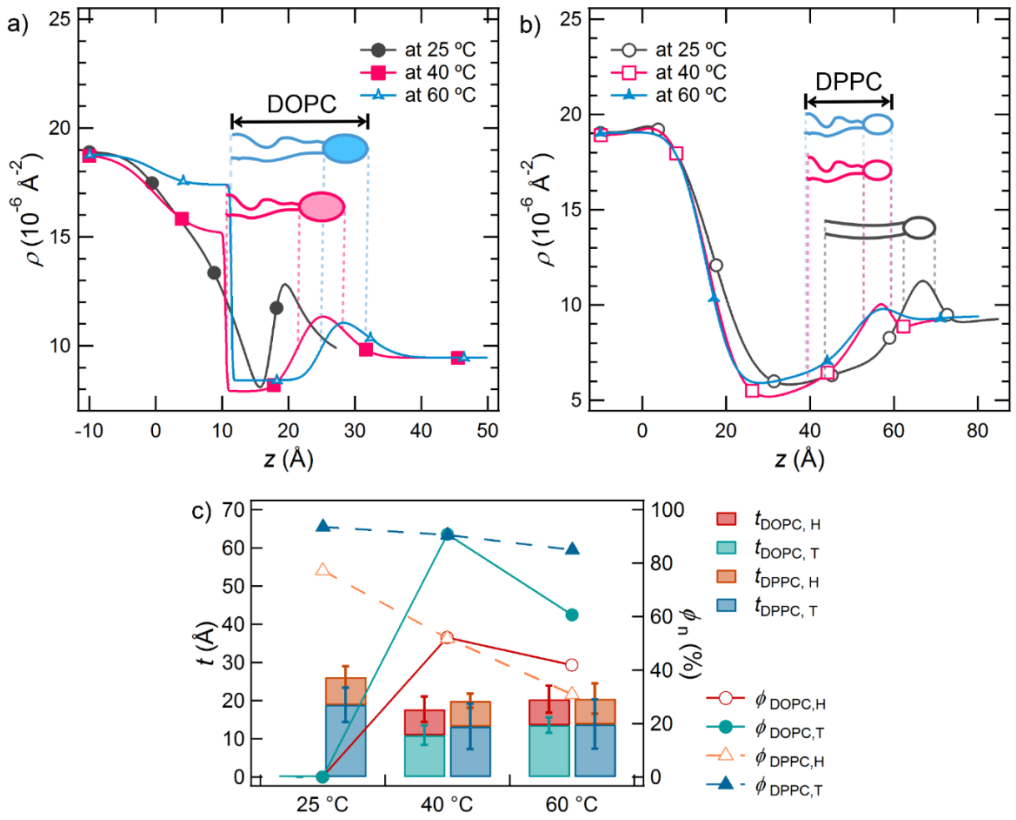

Figure 5.6. SLD profiles of DOPC (a) and DPPC (b) samples on un-soaked graphene collected at diffeent temperatures with the inset cartoons of lipid showing the possible morphologies. The thickness (categories), t, rougness (error bars), R_a, and the coverage (markers and lines), ϕ, of each slabs are compared in (c).

The morphology of the DPPC bilayer formed on the soaked graphene surface has also been studied at different temperatures, where similar decline of lipid membrane thickness during heating has been observed. As shown schematically in Figure 5.7, The DPPC liposomes fused into bilayers with fully-extended hydrocarbon tails at RT (b), melted into shorter bilayers with disordered fluid tails after heating (c). The fitted XRR parameters (Table 5.4) suggest that the t_{bi} of DPPC decreased gradually from 59.1 Å at 25 °C, to 52.0 Å at 40 °C, and to 48.6 Å after the 3-h incubation at 60 °C. Intriguing, the slab structure of the DPPC proximal leaflet was found to be more defined than the distal one. To be specific, the distal leaflet exhibited much larger roughness on the outer headgroup ($R_{a,\ o\text{-}H}$) and hydrocarbon tails ($R_{a,\ o\text{-}T}$) interfaces, as shown in the fitted parameters shown in Table 5.4. After the incubation, the morphology of the outer leaflet became especially chaotic, as the headgroup expanded to $t_{o\text{-}H}$ = 12.0 Å, a value much larger comparing to that before the incubation (this is still in the range of PC headgroup thickness reported in literature, from 4.95 Å to 13.0 ± 1.0 Å [24, 32, 36, 39, 40]), with a roughness as high as

$R_{a,\,o\text{-}H}$ = 10.0 Å. This highly heterogeneous layer structure had also led to miscalculations of the volume fractions, as described in section 5.3.1.

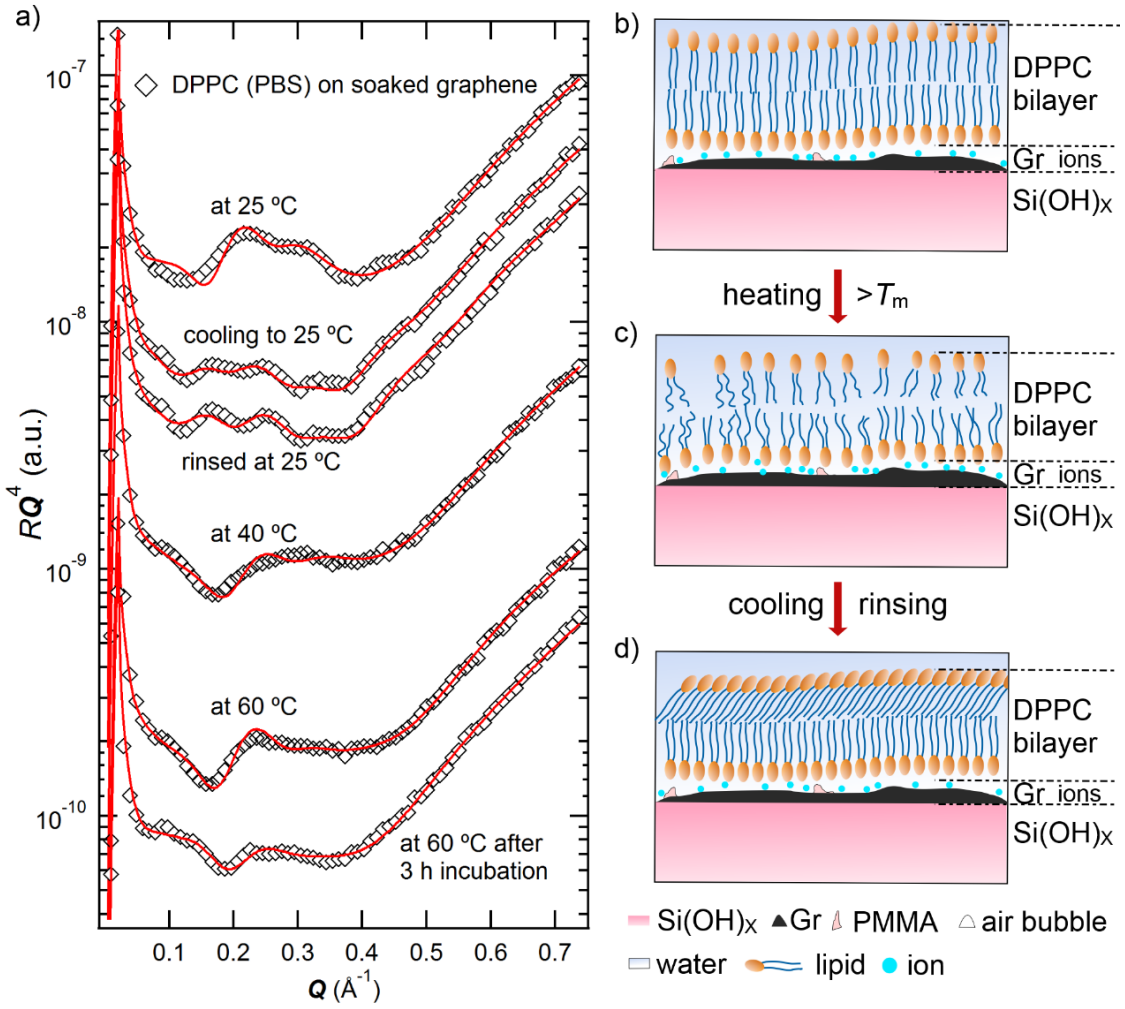

Figure 5.7. DPPC bilayer formed on the soaked graphene *via* vesicle fusion (b) and its thinning (c) and extending (d) behaviour upon heating and cooling suggested by fittings (solid lines) of the XRR results (open markers) shown in (a). The XRR curves were offset vertically for clarity. The DPPC bilayer has been investigated in PBS at 25 °C, 40 °C, 60 °C, after 3 h incubating at 60 °C, cooling back to 25 °C, and rinsing with PBS.

We have also observed that the structure of the DPPC bilayer was not reversible when the sample was cooled back to 25 °C after heating, as illustrated in Figure 5.7d. Even though the thickness of the outer hydrocarbon tail recovered to $t_{i\text{-}T}$ = 20.9 Å, the outer leaflet became more disordered. A more defined structure appeared after rinsing the membrane with PBS, which showed an analogous structure to the sample before heating, but with halved thickness of the outer hydrocarbon tail $t_{i\text{-}T}$ and coverage of the outer headgroup, $\phi_{o\text{-}H}$. suggesting a tilted distal leaflet. The rinsing procedure could remove the

excessive lipids and liposomes existed in the outer layer membrane, thus increasing the membrane homogeneity.

Regardless the chaotic outer leaflet, the 3-h incubation also led to an improved lipid packing. Comparing to the freshly deposited DPPC bilayer at 25 °C, the volume fractions of the inner ($\phi_{i\text{-}T}$) and outer hydrocarbon tails ($\phi_{o\text{-}T}$) after incubating increased from $\phi_{i\text{-}T}$ = 55.7% and $\phi_{o\text{-}T}$ = 80.3% to $\phi_{i\text{-}T}$ = 83.5% and $\phi_{o\text{-}T}$ = 89.9%, respectively, as shown in Figure 5.8c. This relatively compact DPPC chain structure retained after cooling the sample back to 25 °C and rinsing with PBS. Similar well-packed lipid structure was observed in the DOPC bilayer that had been treated in the same procedure as described in section 5.2.4, with $\phi_{i\text{-}T}$ = 88.9% and $\phi_{o\text{-}T}$ = 85.2%. It has been reported that the lateral thermal expansivity of the lipid, could benefit the formation of bilayers with better quality [28, 36, 41], which is in consistency with our results.

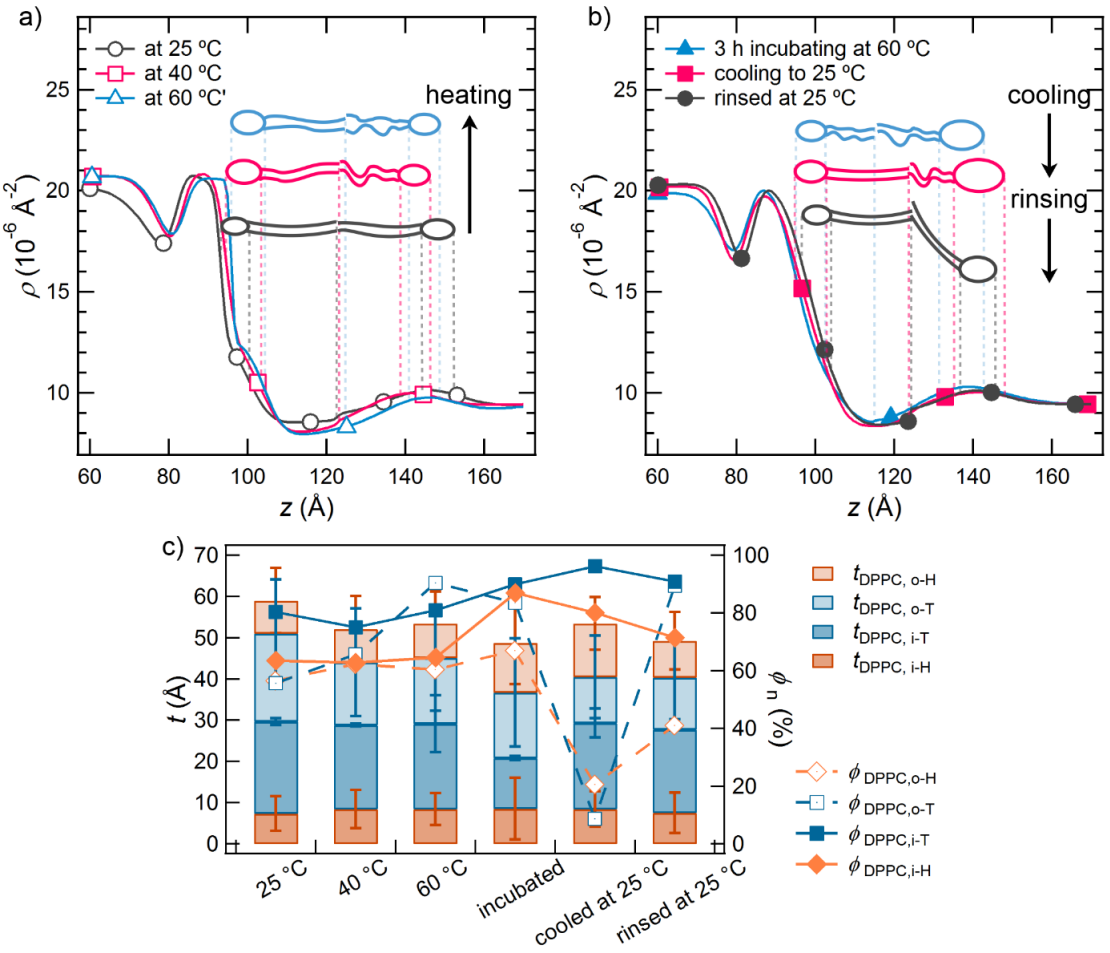

Figure 5.8. Illustration of the DPPC bilayer structure as insets in (a) and (b) at different temperatures suggested by their fitted SLD profiles of the XRR data (*cf.* Figure 5.7a). The thickness (categories), *t*, rougness (error bars), R_a, and the coverage (markers and lines),

ϕ, of the DPPC proximal and distal leaflets are compared in (c). The interfacial roughness between the inner and outer layer hydrocarbon tails remained <0.8 Å, except for the measurements at 60 °C and at 25 °C after cooling, suggesting the two chains exhibits different states of phase during the two measurements.

Moreover, as given by the fitted parameters in Table 5.4, the two leaflets of the DPPC bilayer exhibit very different structures and responses to temperature. The interfacial roughness of the distal leaflet, including $R_{a,o\text{-}H}$ and $R_{a,o\text{-}T}$, were found to be larger than those of the proximal leaflet, $R_{a,i\text{-}H}$ and $R_{a,i\text{-}T}$ at all temperatures, which means the latter was more homogeneous. Besides, before heating to 40 °C, the packing of DPPC proximal layer became more compact than the distal one, suggested by its higher fitted volume fraction and small $R_{a,i\text{-}T}$ (<0.8 Å). In addition, the temperature-dependent thinning behaviour of DPPC bilayer was found to initiate from the distal leaflet. After reaching 40 °C, the thickness of the inner hydrocarbon tails, $t_{i\text{-}T}$, only decreased by 1.9 Å, with the roughness, $R_{a,i\text{-}T}$, reduced by 0.5 Å, whilst the thickness of the outer hydrocarbon tails, $t_{o\text{-}T}$, sharply dropped to 15.2 Å from 21.4 Å at RT, with a reduction of ~ 29.0%. To this stage, the structure of the proximal leaflet of DPPC still seemed to be isolated from the influence of temperature. However, at 60 °C, despite that $t_{i\text{-}T}$ = 20.7 Å, t_{bi} = 53.4 Å remained similar to those at 40 °C, the $R_{a,i\text{-}T}$ increased to 6.9 Å, indicating a heterogenous interface caused by the enhanced chain mobility of the proximal leaflet. The change on $t_{i\text{-}T}$ was only to be observed after the 3-h incubation, when the sample had been kept at 60°C for 3.5 h in total. In summary, the "melting" procedure of DPPC bilayer on graphene happened in two steps: (1) the distal leaflet melts while the proximal leaflet remained in gel phase; (2) the proximal leaflet melts. Similar step-by-step phase transition of DPPC SLB has been systematically studied previously [25, 28, 42]. As reported by Wu *et al.* [25] and Keller *et al.* [42], the enthalpy required for melting the inner leaflet of DPPC bilayer on a solid support has been found to be ~ 3 times larger than that of the outer leaflet, showing the stronger interaction between the substrate and the inner layer. As a consequence, the phase transition of DPPC SLB on graphene was detected to happen in a temperature range. This "melting" procedure can be described using a "crack phase model", in which the membrane would partially melt into a "crack phase" near T_m before the complete phase transition [14, 42].

Table 5.4. Summary of the t_n, $R_{a,n}$, and ϕ_n of the slabs comprising the DPPC bilayer at different temperatures, obtained from fitting the XRR curves shown in Figure 5.7.

		at 25 °C			at 40 °C			at 60 °C		
	slab	t_n (Å)	$R_{a,n}$ (Å)	ϕ_n (%)	t_n (Å)	$R_{a,n}$ (Å)	ϕ_n (%)	t_n (Å)	$R_{a,n}$ (Å)	ϕ_n (%)
during heating	o-H	8.0	7.9	56.4	8.1	8.0	62.2	8.3	7.8	60.3
	o-T	21.4	13.1	55.7	15.2	13.0	65.6	16.0	12.9	90.4
	i-T	22.3	0.8	80.3	20.4	0.3	75.0	20.7	6.9	80.9
	i-H	7.3	4.2	63.4	8.4	4.6	62.8	8.4	3.9	64.6
	bilayer	59.1			52.0			53.4		
after 3 h incubation at 60 °C	o-H	12.9	6.4	20.6				12.0	10.0	66.9
	o-T	11.2	10.0	8.7				15.9	13.1	83.5
	i-T	20.9	3.5	96.2				12.3	0.5	89.9
	i-H	8.4	4.3	80.1				8.5	7.5	86.9
	bilayer	53.5						48.6		
after rinsing with PBS	o-H	8.9	7.0	41.0						
	o-T	12.6	10.1	89.4						
	i-T	20.2	0.0	90.9						
	i-H	7.5	4.9	71.4						
	bilayer	49.2								

It should be noted that in the case of DOPC liposomes in water on the un-soaked graphene, although the fitted SLDs of the diffuse layer for this sample measured at 40 °C ($\rho_d = 10.1 \times 10^{-6}$ Å^{-2}) and 60 °C ($\rho_d = 9.7 \times 10^{-6}$ Å^{-2}) are higher than that of water ($\rho_{water} = 9.44 \times 10^{-6}$ Å^{-2}), the fitted XRR profiles didn't show the formation of organised lipid membrane layer. This can also be distinguished directly from the respective XRR curve (*cf.* Figure 3a in ms section 3.1), where no prominent Kiessig fringes can be observed except for those from bare graphene.

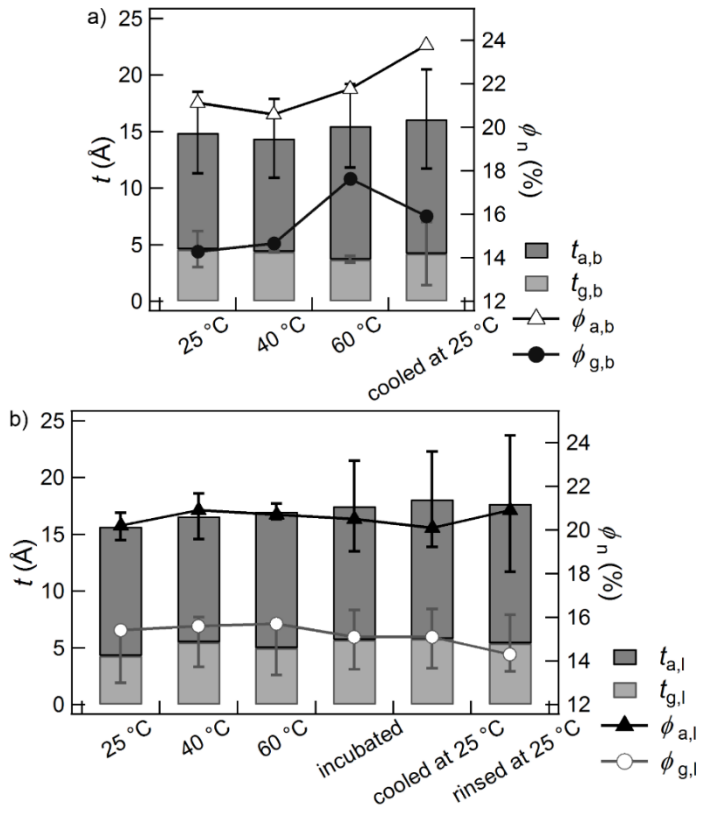

Figure 5.9. Comparison of the thickness t_n (categories) with the corresponding roughness shown as error bars and the coverage ϕ_n (markers and lines) between the graphene layer (g) and the ion adsorbed layer (denoted as a) of the bare graphene (denoted as g) and the lipid adsorbed graphene (denoted as l).

One of the advantages of XRR is that it can probe the structure of the buried interfaces. For example, we can compare the structure of the lipid adsorbed graphene to the bare graphene sample in PBS at different temperatures, as shown in Figure 5.9. The structure of both studied graphene followed a similar trend upon heating and cooling. The thickness of the bare graphene and the lipid adsorbed graphene layer fluctuated around $t_{g,b}$ = 4.2 Å (Figure 5.9a) and $t_{g,l}$ = 5.3 Å (Figure 5.9b) during the experiment, respectively. Whilst the thickness of ion adsorbed layer, t_i, slightly increased upon heating and the expanded thickness retained after cooling. We have attributed the increase in t_i to the enhanced ion adsorption on graphene surface, which was caused by the promoted ion mobility at higher temperatures. The higher rate of ion adsorption also led to the increasing SLDs of the graphene and the ion adsorbed layer, but the SLD increments from 25 °C to 60 °C of the bare graphene sample ($\Delta\rho_{g,b}$ = 3.3 ×10^{-6} Å^{-2} and $\Delta\rho_{i,b}$ = 0.7 ×10^{-6} Å^{-2}) were larger than those of the lipid adsorbed graphene ($\Delta\rho_{g,l}$ = 0.3 ×10^{-6} Å^{-2} and $\Delta\rho_{i,l}$ = 0.5 ×10^{-6} Å^{-2}). A

prolonged equilibrium of the ion adsorption on graphene time could be expected for the lipid adsorbed graphene, as the diffusion of ions and small molecules like water could be restricted by the bilayer structure [40, 43]. However, it has to be pointed out that during the XRR experiment of the bare graphene, the incubating and rinsing procedure were not performed, which could lead to a difference on the compared interfaces.

Table 5.5. Comparison between the lipid membrane thickness obtained from our results and in literature.

	substrate	solvent	temperature (°C)	thickness (Å)	technique	Ref.
DOPC monolayer	CVD graphene on SiO_2	PBS (pH = 7.4)	40	17.7	XRR	this work
			60	20.3		
			at 25 °C after cooling	20.3		
DOPC monolayer	mechanical exfoliated graphene on sapphire	10 mM HEPES*, 150 mM KCl, and 1 mM $CaCl_2$ (pH = 7.4)	RT	23	AFM	[16]
DOPC bilayer	soaked CVD graphene on SiO_2	PBS (pH = 7.4)	at 25 °C after cooling	43.2	XRR	this work
POPC/POPG bilayer	soaked CVD graphene on SiO_2	PBS (pH = 7.4)	at 25 °C after cooling	50 ± 10	AFM	[18]
DOPC trilayer	reduced graphene oxide pm SiO_2	100 mM KCl, 25 mM HEPES (pH 7.4) and $CaCl_2$ (10mM)	-	48	AFM	[28]
DOPC bilayer	mica	water	22	55 ± 1	AFM	[24]
			37 - 40	46 ± 1		
DOPC bilayer stacks	SiO_2	air	15	37.6	X-ray diffuse scattering	[24]
			30	36.1		
			45	36.1		
DOPC multilayer	mica	air	25	49.1	XRR	[20]
	polyethylenimine-coated mica		25	45.0		
	stearic trimethylammonium iodide-coated mica		25	47.8		

Table 5.5 (continued)

DPPC monolayer	CVD graphene on SiO_2	PBS (pH = 7.4)	25	26.2	XRR	this work
			40	19.9		
			60	20.5		
DPPC bilayer	soaked CVD graphene on SiO_2	PBS (pH = 7.4)	25	59.1	XRR	this work
			40	52		
			60	48.6		
			at 25 °C after cooling	49.2		
DPPC bilayer	mica	water	25	58	XRR	[32]
			55	57.2		
			at 25 °C after cooling	57.1		
			25	~ 30.0	AFM	
DPPC bilayer	mica	PBS (pH = 7.4)	50	41.6 ± 6	NR	[36]
			at 25 °C after cooling	50.7 ± 6		
			25	50.1 ± 6		
			25	60	AFM	
DPPC bilayer	mica	PBS (pH = 6.8)	22	48 ± 3	AFM	[28]
			42-52	42 ± 4		
			> 52	33 ± 3		
			at 22 °C after cooling	48 ± 3		
DPPC bilayer	mica	water	22	55 ± 0.2	AFM	[28]
			42 - 52	44 ± 0.2		
			> 52	36 ± 0.3		
DPPC bilayer	mica	Tris-buffer pH = 8.9	25	50	AFM	[25]
			41.5	44		
			49	38		

**HEPES is the abbreviation of N-2 hydroxyethylpiperazine-N'-2- ethanesulfonic acid.*

The size of lipids we obtained from XRR on graphene is largely in consistency with the values reported in literature as shown in Table 5.5. It should be noted that in the case of DOPC liposomes in water on the un-soaked graphene, although the fitted SLDs of the diffuse layer for this sample measured at 40 °C ($\rho_d = 10.1 \times 10^{-6}$ Å^{-2}) and 60 °C ($\rho_d = 9.7 \times 10^{-6}$ Å^{-2}) are higher than that of water ($\rho_{water} = 9.44 \times 10^{-6}$ Å^{-2}), the fitted XRR profiles

didn't show the formation of organised lipid membrane layer. This can also be distinguished directly from the respective XRR curve (*cf.* Figure 5.4a), where no prominent Kiessig fringes can be observed except for those from bare graphene.

5.4 Conclusions

In this study, we have reported the formation of lipid monolayer, bilayer, and multilayer membranes and their structural response to temperature. Synchrotron XRR has been applied to investigate structural characters of the lipid membranes, including thickness, interfacial roughness, and volume fraction (coverage). The XRR results suggest that DOPC and DPPC liposomes would fuse into membranes on graphene with the presence of PBS, while no adsorption was detected from the DOPC liposomes prepared in Milli-Q water. We attribute this observation to the electrostatic repulsions between the liposomes and graphene surface in deionised water, which could be screened by the adding of electrolytes [31]. Furthermore, we have found that the lipids exhibited a different adsorption morphology on graphene that had been soaked in water at RT for 24 h: both DOPC and DPPC liposome formed monolayer membrane on the un-soaked graphene, but bilayer on the soaked graphene. Our previous study showed that the water submergence could reduce the air bubbles present in the textures on graphene surface and cause the hydration of the underlying SiO_2 to $Si(OH)_x$, thus resulting an increase in the graphene hydrophilicity and affinity to ions and biomolecules. The observation that lipids form bilayer on hydrophilic graphene derivatives and monolayer on hydrophilic graphene substrates are in consistency with literature [13, 15]. The lipid membrane structures have been studied at 25 °C, 40 °C, 60 °C and cooling to 25 °C. Regardless the transition temperature, all the samples showed an increase in the lipid mobility, evident from the increased interfacial roughness of the lipid layer, the decreased lipid density, and the membrane thinning behaviour that was observed in few samples. The DPPC bilayer was found to be more compact, with the distal leaflet slightly tilted, after incubating at 60 °C for 3 h, followed by cooling to RT. With the alternation of temperature around its transition temperature, DPPC bilayer showed a step-by-step phase transition upon heating and cooling, with a higher lipid mobility of the distal leaflet due to the interaction between the proximal leaflet and the graphene substrate [25, 28, 42]. The formation of highly disordered lipid multilayer prepared from drop-casting has also been detected by XRR at air-solid interface. Despite the heterogeneous structure, the multilayer showed a similar

structural dependence upon heating as the lipid monolayers and bilayers (in Appendix VI).

In addition, the structure of graphene buried by DPPC followed a similar scenario as that of bare graphene that we have observed previously, proving the potential of XRR to probe the structure of the adsorbed biomolecule as well as the graphene substrate concurrently. These unprecedented results are important for the understanding of the interfacial adsorption of biomolecules on graphene, and is relevant to the development of graphene bioanalytical devices and the application of graphene in biosensing.

Reference

1. Novoselov, K.S., et al., *A roadmap for graphene.* Nature, 2012. **490**(7419): p. 192-200.
2. Wang, Y., et al., *Graphene and graphene oxide: biofunctionalization and applications in biotechnology.* Trends in Biotechnology, 2011. **29**(5): p. 205-212.
3. Novoselov, K.S., et al., *Electric field effect in atomically thin carbon films.* Science, 2004. **306**(5696): p. 666-669.
4. Castro Neto, A.H., et al., *The electronic properties of graphene.* Reviews of Modern Physics, 2009. **81**(1): p. 109-162.
5. Leenaerts, O., Partoens, B., and Peeters, F.M., *Adsorption of H(2)O, NH(3), CO, NO(2), and NO on graphene: a first-principles study.* Physical Review B, 2008. **77**(12): p. 125416.
6. Khatayevich, D., et al., *Selective detection of target proteins by peptide-enabled graphene biosensor.* Small, 2014. **10**(8): p. 1505-13, 1504.
7. Ang, P.K., et al., *A bioelectronic platform using a graphene-lipid bilayer interface.* Acs Nano, 2010. **4**(12): p. 7387-7394.
8. Hegab, H.M., et al., *The controversial antibacterial activity of graphene-based materials.* Carbon, 2016. **105**: p. 362-376.
9. Titov, A.V., Kral, P., and Pearson, R., *Sandwiched graphene-membrane superstructures.* Acs Nano, 2010. **4**(1): p. 229-234.
10. Liu, S.B., et al., *Antibacterial activity of graphite, graphite oxide, graphene oxide, and reduced graphene oxide: membrane and oxidative stress.* Acs Nano, 2011. **5**(9): p. 6971-6980.
11. Sanchez, V.C., et al., *Biological interactions of graphene-family nanomaterials: an interdisciplinary review.* Chemical Research in Toxicology, 2012. **25**(1): p. 15-34.
12. Pinto, A.M., Goncalves, I.C., and Magalhaes, F.D., *Graphene-based materials biocompatibility: a review.* Colloids and Surfaces B-Biointerfaces, 2013. **111**: p. 188-202.

13. Tabaei, S.R., et al., *Controlling the formation of phospholipid monolayer, bilayer, and intact vesicle layer on graphene.* Acs Applied Materials & Interfaces, 2016. **8**(18): p. 11875-11880.

14. Richter, R.P., Berat, R., and Brisson, A.R., *Formation of solid-supported lipid bilayers: an integrated view.* Langmuir, 2006. **22**(8): p. 3497-3505.

15. Melendrez, D., et al., *Adsorption and binding dynamics of graphene-supported phospholipid membranes using the QCM-D technique.* Nanoscale, 2018. **10**(5): p. 2555-2567.

16. Yamazaki, K., Kunii, S., and Ogino, T., *Characterization of interfaces between graphene films and support substrates by observation of lipid membrane formation.* Journal of Physical Chemistry C, 2013. **117**(37): p. 18913-18918.

17. Frost, R., et al., *Graphene oxide and lipid membranes: interactions and nanocomposite structures.* Nano Letters, 2012. **12**(7): p. 3356-3362.

18. Tsuzuki, K., et al., *Reduced graphene oxide as the support for lipid bilayer membrane.* Asia-Pacific Interdisciplinary Research Conference 2011 (Ap-Irc 2011), 2012. **352**: p. 012016.

19. Lei, H.Z., et al., *Morphology change and detachment of lipid bilayers from the mica substrate driven by graphene oxide sheets.* Langmuir, 2014. **30**(16): p. 4678-4683.

20. Sironi, B., et al., *Structure of lipid multilayers via drop casting of aqueous liposome dispersions.* Soft Matter, 2016. **12**(17): p. 3877-3887.

21. Giri, R.P., Chakrabarti, A., and Mukhopadhyay, M.K., *Cholesterol-induced structural changes in saturated phospholipid model membranes revealed through X-ray scattering technique.* Journal of Physical Chemistry B, 2017. **121**(16): p. 4081-4090.

22. Patil, Y.P. and Jadhav, S., *Novel methods for liposome preparation.* Chemistry and Physics of Lipids, 2014. **177**: p. 8-18.

23. Ulrich, A.S., Sami, M., and Watts, A., *Hydration of DOPC bilayers by differential scanning calorimetry.* Biochimica Et Biophysica Acta-Biomembranes, 1994. **1191**(1): p. 225-230.

24. Pan, J., et al., *Temperature dependence of structure, bending rigidity, and bilayer interactions of dioleoylphosphatidylcholine bilayers.* Biophysical Journal, 2008. **94**(1): p. 117-124.

25. Wu, H.L., et al., *Phase transition behaviors of the supported DPPC bilayer investigated by sum frequency generation (SFG) vibrational spectroscopy and atomic force microscopy (AFM).* Physical Chemistry Chemical Physics, 2016. **18**(3): p. 1411-1421.

26. Als-Nielsen, J. and McMorrow, D., *Elements of modern X-ray physics*. 2nd ed. 2011, Oxford: Wiley-Blackwell. xii, 419 p.

27. Porod, G., *Die Röntgenkleinwinkelstreuung von dichtgepackten kolloiden systemen.* Kolloid-Zeitschrift and Zeitschrift Fur Polymere, 1951. **124**(2): p. 83-114.

28. Leonenko, Z.V., et al., *Investigation of temperature-induced phase transitions in DOPC and DPPC phospholipid bilayers using temperature-controlled scanning force microscopy.* Biophysical Journal, 2004. **86**(6): p. 3783-3793.

29. Lind, T.K. and Cardenas, M., *Understanding the formation of supported lipid bilayers via vesicle fusion-A case that exemplifies the need for the complementary method approach (Review).* Biointerphases, 2016. **11**(2): p. 020801.

30. Chibowski, E. and Szczes, A., *Zeta potential and surface charge of DPPC and DOPC liposomes in the presence of PLC enzyme.* Adsorption-Journal of the International Adsorption Society, 2016. **22**(4-6): p. 755-765.

31. Chen, A.W., et al., *Evidence for negative charge near large area supported graphene in water: a study of silica microsphere interactions.* Journal of Colloid and Interface Science, 2017. **492**: p. 15-24.

32. Sironi, B., *Lipid adsorption at interfaces: a synchrotron X-ray reflectivity study.*, in *School of Chemistry*. 2016, University of Bristol: Bristol, UK.

33. Sabio, J., et al., *Electrostatic interactions between graphene layers and their environment.* Physical Review B, 2008. **77**(19): p. 195409

34. Hassanali, A.A. and Singer, S.J., *Model for the water-amorphous silica interface: the undissociated surface.* Journal of Physical Chemistry B, 2007. **111**(38): p. 11181-11193.

35. Nagle, J.F. and Tristram-Nagle, S., *Structure of lipid bilayers.* Biochimica Et Biophysica Acta-Reviews on Biomembranes, 2000. **1469**(3): p. 159-195.

36. Lind, T.K., Cardenas, M., and Wacklin, H.P., *Formation of supported lipid bilayers by vesicle fusion: effect of deposition temperature.* Langmuir, 2014. **30**(25): p. 7259-7263.

37. de Ghellinck, A., et al., *Probing the position of resveratrol in lipid bilayers: a neutron reflectivity study.* Colloids and Surfaces B-Biointerfaces, 2015. **134**: p. 65-72.

38. Nir, S., et al., *Aggregation and fusion of phospholipid-vesicles.* Progress in Surface Science, 1983. **13**(1): p. 1-124.

39. Tarek, M., et al., *Molecular dynamics simulations of supported phospholipid/alkanethiol bilayers on a gold(111) surface.* Biophysical Journal, 1999. **77**(2): p. 964-972.

40. Eicher, B., et al., *Joint small-angle X-ray and neutron scattering data analysis of asymmetric lipid vesicles.* Journal of Applied Crystallography, 2017. **50**: p. 419-429.

41. Garcia-Manyes, S., Oncins, G., and Sanz, F., *Effect of temperature on the nanomechanics of lipid bilayers studied by force spectroscopy.* Biophysical Journal, 2005. **89**(6): p. 4261-4274.

42. Keller, D., et al., *Decoupled phase transitions and grain-boundary melting in supported phospholipid bilayers.* Physical Review Letters, 2005. **94**(2): p. 025701.

43. Mathai, J.C., et al., *Structural determinants of water permeability through the lipid membrane.* Journal of General Physiology, 2008. **131**(1): p. 69-76.

Chapter 6

Conclusions and future work

6.1 Conclusion

The structure of graphene is relevant to its physical properties, such as its 2D electronic properties that are essential for its applications [1, 2]. Methods of determining the structure of graphene have been established, applying techniques such as Raman Spectroscopy [3-7] and atomic force microscopy (AFM). However, such techniques are restricted when graphene is covered by other molecules, thereby lacking the ability to probe the graphene surface in an interaction.

In this study, we have used synchrotron X-ray reflectivity (XRR), to study the structure of commercially available graphene (prepared via chemical vapour deposition and marketed as graphene monolayers) on SiO_2/Si in different environments, and established a 3-slab model for the curve fittings. XRR is a rigorous technique that can be used to monitor the structural change of materials *in situ* in different conditions on the interface [8, 9]. Firstly, together with X-ray photoelectron spectroscopy, photoemission electron microscopy and AFM, the composition and morphology of the studied graphene samples have been evaluated. Then XRR, AFM, and contact angle measurements have been used to study the graphene in contact with aqueous systems. Finally, XRR has been applied to investigate the interaction between graphene and liposomes of 1,2-dioleoyl-sn-glycero-3-phosphocholine (DOPC) or 1,2-dipalmitoyl-sn-glycero-3-phosphocholine (DPPC). The formation and the structural characters of lipid monolayer, bilayer, and multilayer (shown in Appendix VI) membranes, including thickness, interfacial roughness, and the lipid volume fraction (coverage) are reported.

The results indicate that the graphene samples we characterised consisted of 3 - 4 layers of graphene monolayer, which should be described as few layer graphene, with a "contaminant" layer, comprising polymethylmethacrylate (PMMA) and graphene multilayers atop. Furthermore, tentative results have been described on the effect of temperature on the thickness of the graphene layer (t_g): at 25 ºC, t_g given by XRR was 13.0 ± 1.0 Å, in agreement with that obtained from AFM (13.9 ± 0.7 Å), upon heating to 60 ºC, t_g expanded to 13.8 Å, which further increased to 14.3 Å when cooling to 25 ºC.

This temperature dependent thickness is attributed to the out-of-plane rippling of graphene as previously reported [10, 11] in this study.

When displacing graphene in water, a diffuse layer was found to immediately adjacent to graphene with a scattering length density (SLD) of 6.72×10^{-6} $Å^{-2}$, which can be a result of the presence of air bubbles on graphene under water. An elevated area with the shape of a bubble has also been captured by AFM imaging. The diffuse layer diminished after the graphene was submerged in water for 24 h at 25 ºC, with the wettability increased spontaneously indicated by decreased water contact angle of graphene from 84.9 ± 0.4° to 55.6 ± 0.4° after submergence. The increased hydrophilicity can be attributed to the disappearance of the air bubbles and the rehydration of the silica substrate. Similar to that measured in air, the graphene measured in aqueous systems also exhibits a temperature dependent structural change, but this phenomenon is more likely to be associated with the enhanced adsorption of ions at higher temperatures.

Knowing that the addition of ions, temperature, and the water submergence have influences on the surface structure and chemistry of the graphene substrates, it can be foreseen that the interaction between the liposomes and graphene can be influenced by these factors. Indeed, the fusion of liposomes on graphene in this study has only been observed in phosphate buffered saline, but not in Milli-Q, which could be a result of the electrostatic repulsion between the liposomes and graphene [12]. In addition, the results suggest that lipids tend to form monolayers on the un-soaked graphene, but bilayers on the soaked graphene, possibly due to the promoted graphene hydrophilicity after soaking [13, 14]. Moreover, the studied lipid membranes all showed structural responses to temperature, which were comparable with lipid membranes on other substrates [15-17] and the temperature dependent thickness of bare graphene in this study.

Overall, this study provides a new understanding on the morphology of lipid membrane on graphene and demonstrate the capability of XRR to probe the surface and interfacial structures graphene coated with biomolecules, which is relevant to the development of graphene bioanalytical devices and the application of graphene in biosensing.

6.2 Future Work

As mentioned earlier in the results and discussion chapters, because of the limited number of studied samples, some of the interesting observations presented in this work, such as the tentative results that show a temperature dependent thickness variation, require further

investigation. In addition, in this work, the interpretation of the results predominantly relied on the XRR experiments. Even though XRR is a powerful characterisation method, it would be useful compare it with few more techniques that are commonly used in graphene structural characterisation and interaction with biomolecules, such as Raman spectroscopy [3-7] and quartz crystal microbalance with dissipation monitoring [13, 14, 18].

In addition, as the hydrophobicity of the un-soaked graphene is likely to be brought by the heterogenous surface structures, it will be useful to compare the structure (*i.e.* thickness, roughness and coverage) of graphene before and after annealing at 450 °C in air and in aqueous systems. Without the PMMA residues, the calculation of the graphene coverage will be more straightforward for both XRR and AFM analysis. In terms of the graphene-lipid interaction, further kinetic studies on the liposome fusion can also be performed to optimise the experimental conditions of the lipid coating on graphene.

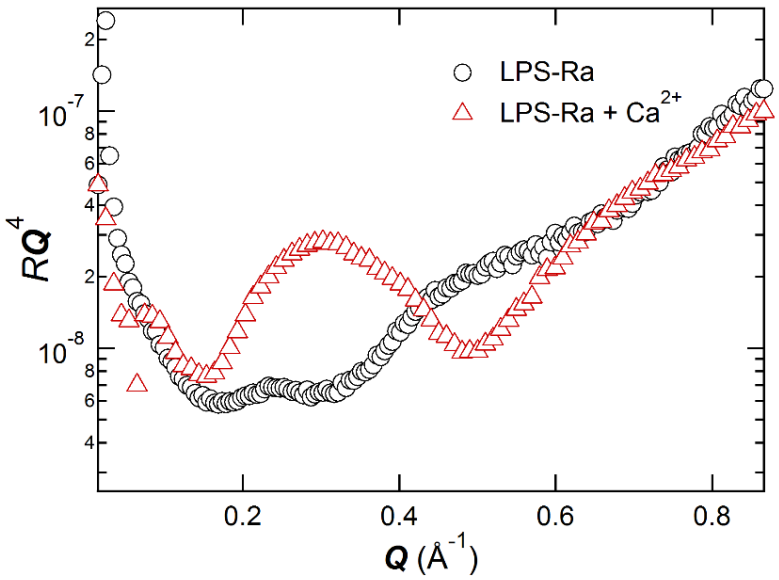

Figure 6.1 XRR curves of the possible LPS-Ra adsorption on graphene, in water and in the presence of 10 mM $CaCl_2$.

Among all the techniques that have been used to probe the structure of graphene and its interaction with biomolecules, XRR is a relatively new technique, little can be found in literature. Hence, it would be useful to document the structural information provided by XRR measurements on other related systems. For example, the adsorption of lipopolysaccharide (LPS) on graphene. LPS, a type of endotoxins, is the major component (up to 90%) of the outer leaflet of the gram-negative bacteria. Its adsorption behaviour in

presence of Ca^{2+} on the DOPE-coated mica wafers has been observed by XRR and AFM[1]. The interaction between LPS and graphene has also been investigated by XRR, which can benefit the interpretation of the antibacterial activities of graphene. As shown in Figure 6.1, Kiessig fringes appeared on the XRR curve after the adding of Ca^{2+}, which can be a result of the LPS adsorption. However, further data analysis is needed for a comprehensive conclusion.

[1] Islas L *et al.*, in preparation.

Reference

1. Xu, M.S., et al., *Auger electron spectroscopy: a rational method for determining thickness of graphene films.* Acs Nano, 2010. **4**(5): p. 2937-2945.
2. Jang, W.Y., et al., *Thickness-dependent thermal conductivity of encased graphene and ultrathin graphite.* Nano Letters, 2010. **10**(10): p. 3909-3913.
3. Ferrari, A.C., et al., *Raman spectrum of graphene and graphene layers.* Physical Review Letters, 2006. **97**(18): p. 187401.
4. Casiraghi, C., et al., *Raman spectroscopy of graphene edges.* Nano Letters, 2009. **9**(4): p. 1433-1441.
5. Das, A., Chakraborty, B., and Sood, A.K., *Raman spectroscopy of graphene on different substrates and influence of defects.* Bulletin of Materials Science, 2008. **31**(3): p. 579-584.
6. Huang, M.Y., et al., *Phonon softening and crystallographic orientation of strained graphene studied by Raman spectroscopy.* Proceedings of the National Academy of Sciences of the United States of America, 2009. **106**(18): p. 7304-7308.
7. Hao, Y.F., et al., *Probing layer number and stacking order of few-layer graphene by Raman spectroscopy.* Small, 2010. **6**(2): p. 195-200.
8. Sironi, B., et al., *Structure of lipid multilayers via drop casting of aqueous liposome dispersions.* Soft Matter, 2016. **12**(17): p. 3877-3887.
9. Giri, R.P., Chakrabarti, A., and Mukhopadhyay, M.K., *Cholesterol-induced structural changes in saturated phospholipid model membranes revealed through X-ray scattering technique.* Journal of Physical Chemistry B, 2017. **121**(16): p. 4081-4090.
10. Bao, W.Z., et al., *Controlled ripple texturing of suspended graphene and ultrathin graphite membranes.* Nature Nanotechnology, 2009. **4**(9): p. 562-566.
11. Yoon, D., Son, Y.W., and Cheong, H., *Negative thermal expansion coefficient of graphene measured by Raman spectroscopy* Nano Letters, 2011. **11**(8): p. 3227-3231.

12. Chen, A.W., et al., *Evidence for negative charge near large area supported graphene in water: a study of silica microsphere interactions.* Journal of Colloid and Interface Science, 2017. **492**: p. 15-24.

13. Melendrez, D., et al., *Adsorption and binding dynamics of graphene-supported phospholipid membranes using the QCM-D technique.* Nanoscale, 2018. **10**(5): p. 2555-2567.

14. Tabaei, S.R., et al., *Controlling the formation of phospholipid monolayer, bilayer, and intact vesicle layer on graphene.* Acs Applied Materials & Interfaces, 2016. **8**(18): p. 11875-11880.

15. Leonenko, Z.V., et al., *Investigation of temperature-induced phase transitions in DOPC and DPPC phospholipid bilayers using temperature-controlled scanning force microscopy.* Biophysical Journal, 2004. **86**(6): p. 3783-3793.

16. Wu, H.L., et al., *Phase transition behaviors of the supported DPPC bilayer investigated by sum frequency generation (SFG) vibrational spectroscopy and atomic force microscopy (AFM).* Physical Chemistry Chemical Physics, 2016. **18**(3): p. 1411-1421.

17. Keller, D., et al., *Decoupled phase transitions and grain-boundary melting in supported phospholipid bilayers.* Physical Review Letters, 2005. **94**(2): p. 025701.

18. Frost, R., et al., *Graphene oxide and lipid membranes: interactions and nanocomposite structures.* Nano Letters, 2012. **12**(7): p. 3356-3362.

Appendix

I. XPS Fittings and PEEM Results

The photoemission lines are fitted by the programme package *Multipeak* in *Igor Pro*. The annealing procedure was observed to be more efficient at higher temperatures as shown in Figure S1. After annealing the sample at 200 ºC, there was no prominent decrease on the carbon oxide peaks, while after annealing at 400 ºC, the C-OH peak disappeared, and the intensity of all the oxide structures decreased, indicating PMMA was burnt off by the procedure. The binding energy of the fitted peaks and corresponding structures [1, 2] of graphene samples before and after annealing are shown in Table S1. The slight shifts of peaks after annealing is probably a mathematic artefact. Similarly, the work function maps of the sample annealed at 400 ºC and 450 ºC for 1 h also showed fewer PMMA structures after annealing at the higher temperature (Figure S2).

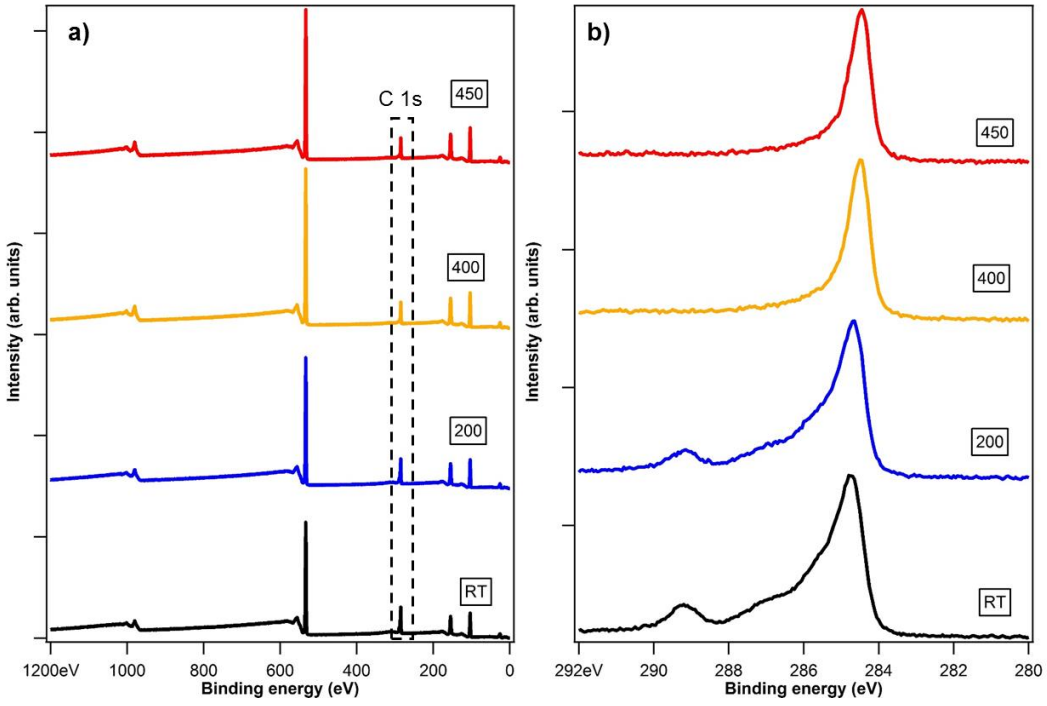

Figure S1. a) The XPS surveys for a CVD graphene sample measured at RT (black), after annealed at 200 °C (blue), after further annealed at 400 °C (yellow) and at 450 °C (red). b) shows the C 1s photoemission region highlighted in the dashed rectangle in a).

Table S1. Peak fittings of XPS results.

	Binding energy (eV)	Possible structure
Before annealing	284.7	C sp^2
	285.2	C sp^3
	286.7	C-OH
	289.2	O-C=O
After annealed at 450 °C	284.5	C sp^2
	285.0	C sp^3
	288.8	O-C=O

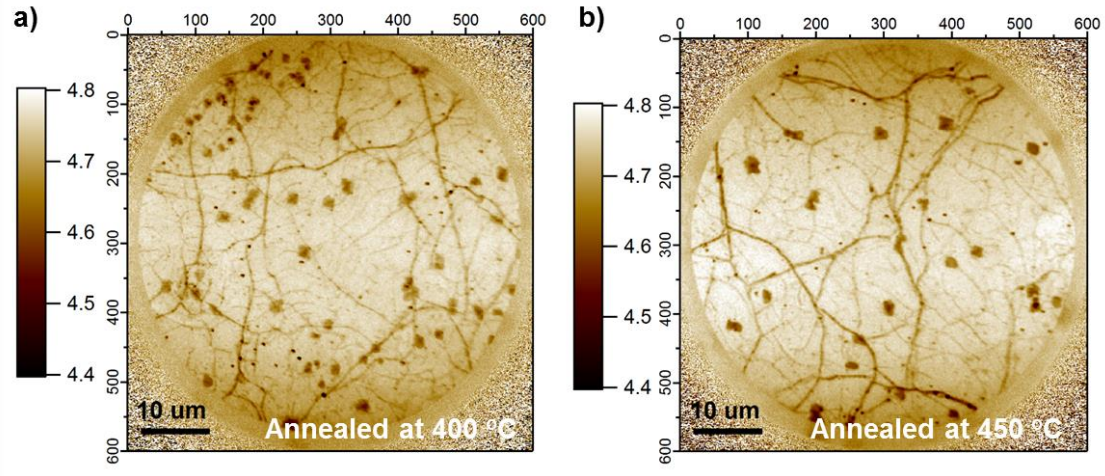

Figure S2. The work function maps of graphene samples annealed at 400 ºC for 1 h (a) and at 450 ºC for a further 20 min. Additional annealing reduced PMMA contaminants on the graphene surface.

II. Histogram Analysis of AFM Results

To estimate the thickness (t_g) and the coverage of the graphene samples (ϕ_g) from the AFM images, the histograms of five 1 μm^2 areas (red squares in Figure S3a.) were fitted with two Gaussian peaks, the results are shown in Table S2. The two fitted peak positions represent the average height scales of the silica substrate (h_s) and of the graphene/contaminants layer (h_g). The spacing (Δh) between h_s and h_g, is equal to t_g, the calculated t_g by AFM topological images is, therefore, 13.9 ± 0.7 Å. In addition, the integrations of each peak show ϕ_g = 85.1 ± 2.1 % of the corresponding regions. The exposed silica substrates below h_s = -12.2 ± 0.8 Å are highlighted in Figure S3b, using the *NanoScope Analysis* software. Similarly, the contaminants, composed by multilayer graphene and PMMA residues above h_g = -1.7 ± 1.0 Å is shown in Figure S3c.

Table S2. Peak fittings for the histograms of the selected areas shown in Figure S3a, showing the peak height scales of the silica (h_s) substrate and graphene (h_g), the difference between the two peaks (Δh), and the coverage of graphene (ϕ_g).

No	h_S **(Å)**	h_g **(Å)**	Δh **(Å)**	ϕ_g **(%)**
1	-11.0	2.7	13.7	82.7
2	-11.9	1.9	13.9	85.5
3	-13.0	0	13.0	84.7
4	-12.2	1.7	13.9	84.3
5	-12.9	2.0	14.9	88.5
Mean (Å)	-12.2	1.7	13.9	85.1
Deviation (Å)	0.8	1.0	0.7	2.1

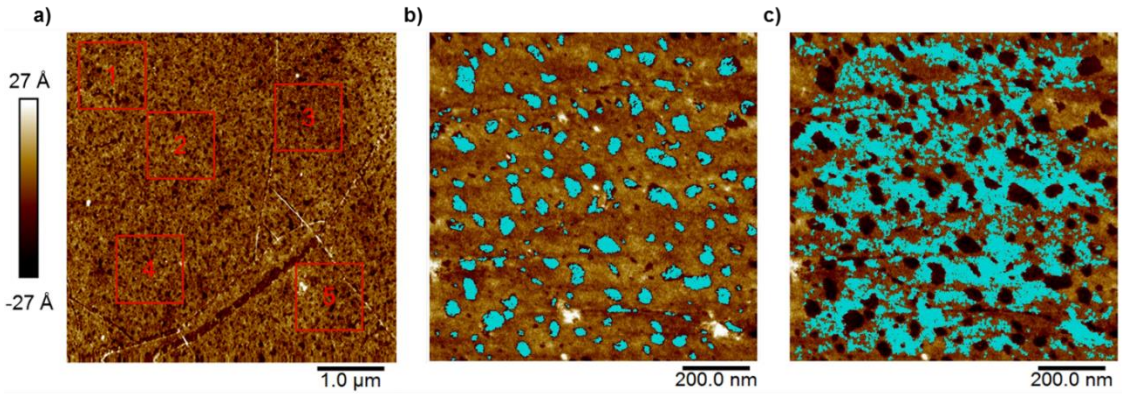

Figure S3. a) AFM topological image on a 5 µm × 5 µm scale. The squares (1-5) are the selected area for the histogram analysis of the graphene sample. The highlighted regions in b) and c) attributed to the silica substrate and contaminants (graphene multilayers and PMMA) from the analysis, respectively.

III. Contact Angle Measurement

Contact angle measurements of graphene were taken at 26.3 ºC using the Sessile drop method on a KRÜSS® DSA100 instrument Angle measurement was carried out using the proprietary image analysis software, as shown in Figure S6. The average contact angle of graphene is 76.77 º ± 0.53º as shown in Table S3, which shows graphene is somewhat hydrophilic.

Figure S4. A contact angle measurement of graphene, the droplet is water.

Table S3. Contact angle measurements of graphene at 26.3 ºC.

No	Contact angle (mean) [˚]
1	76.78
2	76.44

3	77.51
4	76.13
5	76.97
Mean	76.77 ± 0.53

Water contact angle (WCA) measurements of graphene were taken in ambient condition using the Sessile drop method on a KRÜSS® DSA100 instrument. Contact angle measurements were carried out using the proprietary image analysis software. The analysed WCAs of graphene before and after soaking in Milli-Q water for 24 h at room temperature are shown in

Table S4 which suggests the wettability of graphene changed after soaking. The volume of the droplet was 0.5 µL, and the photos (Figure S5) were taken within 20 s after casting the water drop onto the surface.

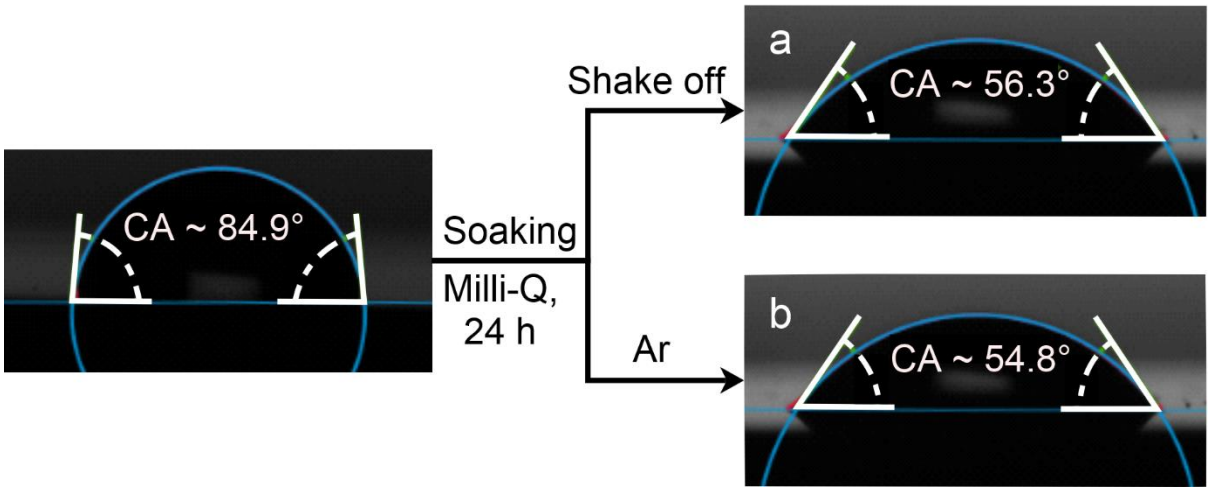

Figure S5. WCA of graphene, before and after soaking.

Table S4. WCA of graphene before and after soaking. After soaking, the graphene samples were dried by two methods: (i) shaking the water off, and letting it dry naturally[a], or (ii) using an argon flow to dry the surface carefully[b].

No.	WCA before soaking (°)	WCA after soaking[a](°)	WCA after soaking[b] (°)
1	84.8	56.7	55.2
2	85.4	56.6	55.1
3	84.7	56.6	54.9
4	84.6	56.2	54.9
5	84.4	56.2	54.4
6	85.4	55.8	54.6
7	84.9	55.9	54.3
Mean	84.9	56.3	54.8
Standard deviation	0.39	0.36	0.35
Temperature (°C)	23.8	19.3	19.2

IV. DLS Results

As described in section 2.5, the obtained $D_{t,ave}$ from DLS is the intensity weighted diffusion coefficient, the given average hydrodynamic diameter (often expressed as the "z-average size") should be the intensity weighted harmonic mean size as it is inversely proportional to D_t [3]. The fitted z-average as well as the respective polydispersity index (PDI) of the studied DOPC and DPPC liposomes that were measured right after their preparation and after a 1-week storage at 4 °C, and the results are listed in Table S5.

Table S5. The fitted D_z and PDI of the liposomes that had been used in the synchrotron experiments.

	solutions	DOPC-PBS	DOPC-water	DPPC-PBS	
	T (°C)	25	25	25	55
freshly made	z-average (nm)	121.1	120.6	98.3	124.3
	PDI	0.065	0.073	0.086	0.158
after 1 week	z-average (nm)	124.5	117.4	110.6	
	PDI	0.075	0.080	1.193	

V. XRR Data Fitting

The complete XRR data fittings for bare graphene measured in aqueous systems and interacted with liposomes are listed in Table S6 and

Table S7, respectively.

Table S6. Best fits for the studied XRR data in aqueous systems.

Sample	Layers	t_n (Å)	ρ_n (10^{-6} Å^{-2})	$R_{a,n}$ (Å)	χ^2 (10^{-3})
Graphene in air at 25 °C	Contaminants	10.8	11.9	2.4	1.11
	Graphene	14.4	14.1	0.4	
	SiO_2	3000	19	2.4	
Graphene in water at 25 °C	Diffuse layer	84.9	6.7	31.9	0.47
	Graphene	16.5	14.9	0.7	
	SiO_2	3000	18.9	3.4	
Graphene in PBS at 25 °C	Diffuse layer	118.3	6.75	49.3	0.7
	Graphene	15.4	19.71	4.5	
	Graphene	3000	18.91	3.5	

Table S6 (continued)

Soaked graphene in water at 25 °C	Ion adsorbed layer	10.1	19.5	1	0.19
	Graphene	5	14.9	2.3	
	silanol	78.9	21.3	4.6	
	SiO_2	3000	19	69.7	
Soaked graphene in PBS at 25 °C	Ion adsorbed layer	10.3	21.1	3.6	0.24
	Graphene	4.6	14.3	1.6	
	silanol	70.2	20.9	2.1	
	SiO_2	3000	19.1	69.2	
Soaked graphene in PBS at 40 °C	Ion adsorbed layer	10	20.6	3.5	0.14
	Graphene	4.4	14.6	0.1	
	silanol	70.1	20.2	2.6	

	SiO_2	3000	19	69.3	
Soaked graphene in PBS at 60 °C	Ion adsorbed layer	11.8	21.8	3.7	0.16
	Graphene	3.7	17.6	0.3	
	silanol	81	21.2	1.6	
	SiO_2	3000	18.8	55.9	
Soaked graphene in PBS cooled at 25 °C	Ion adsorbed layer	11.9	23.8	4.4	0.19
	Graphene	4.2	15.9	2.8	
	silanol	75.8	20.6	3.6	
	SiO_2	3000	18.8	58.9	

From the fitting of our results (Table S6), the thickness and the SLD of the adsorbed ion layer increased upon heating the sample to 60 °C, and was retained after cooling it back to 25 °C. This trend was also seen in the SLD of the corresponding XRR curves. It can be seen in Figure S6 that at 40 °C the interface between graphene and the adsorbed ion layer became smoother, which we attributed to the adsorbed ions filling any gaps and holes that existed on the graphene surface. The ρ_a also increased slightly, implying that the density of electrons of this layer increased. At 60 °C, not only did t_a and ρ_{aI} increased significantly, but also ρ_g, ρ_s, and t_s. Although the thickness expansion of the ion adsorbed layer remained after cooling, the interfacial roughness between graphene and the ion adsorbed layer, $R_{a,g}$, increased spontaneously, suggesting that the ion adsorption was favoured at higher temperature.

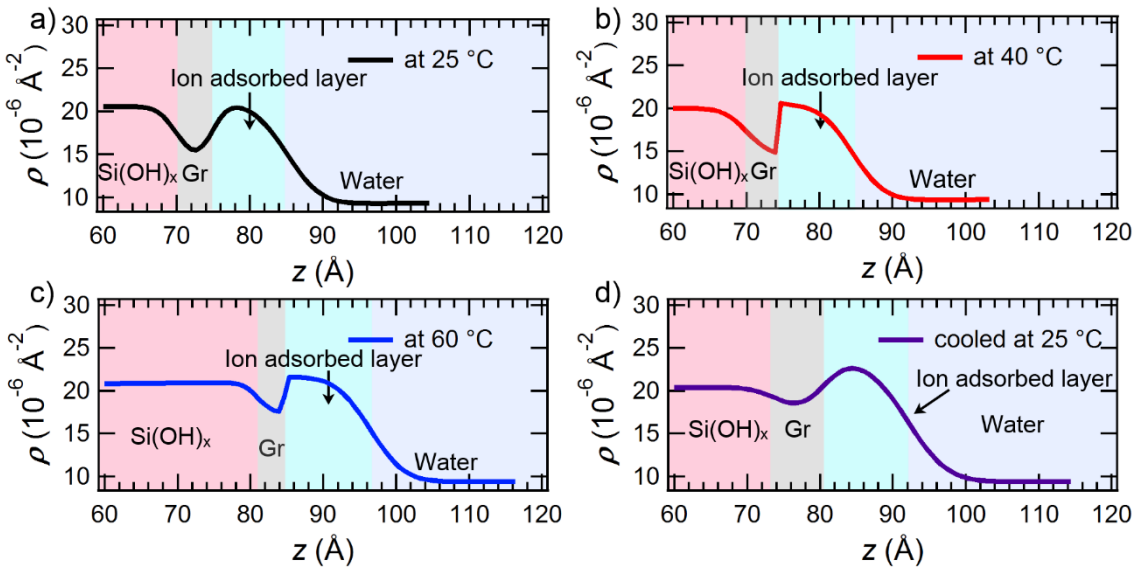

Figure S6. The SLD profiles of soaked graphene in PBS at 25 °C (a), 40 °C (b), 60 °C (c), and after cooling back to 25 °C (d). The modelled slabs are highlighted in boxes, the height and width of each box represents the represents the ρ_n, and the t_n of the n^{th} layer, respectively.

Table S7. Best fits for all the collected XRR data. The fitted thickness, SLD, and roughness of the n^{th} slab are denoted by t_n, ρ_n, and $R_{a,n}$, respectively. DOPC-H, DOPC-T, DPPC-H, and DPPC-T represent the headgroup, hydrocarbon tail slabs of the DOPC and DPPC monolayers, respectively. DOPC-H (i), DOPC-T (i), DOPC-H (o), DOPC-T (o), DPPC-H (i), DPPC-T (i), DPPC-H (o), DPPC-T (o) represent the headgroup, hydrocarbon tail slabs of the DOPC inner/outer leaflets, and DPPC inner/outer leaflets, respectively.

DOPC in water on un-soaked graphene					
	Layers	t_n (Å)	ρ_n (10^{-6} Å^{-2})	$R_{a,n}$ (Å)	χ^2 (10^{-3})
at 25 °C	diffuse layer	3.4	0.0	1.0	2.1
	graphene	15.9	17.2	6.3	
	SiO_2	3000	18.9	2.1	
at 40 °C	diffuse layer	22.5	10.1	1.9	2.0
	graphene	13.7	17.4	0.3	
	SiO_2	3000	19.1	0.2	
at 60 °C	diffuse layer	24.3	9.7	2.2	1.3
	graphene	15.7	16.9	0.0	
	SiO_2	3000	19.2	3.0	
cooling to 25 °C	diffuse layer	3.7	7.4	2.4	2.4
	graphene	16.4	16.1	0.5	
	SiO_2	3000	19.2	5.6	

Table S7 (continued)

DOPC in PBS on un-soaked graphene					
	Layers	t_n (Å)	ρ_n (10^{-6} Å^{-2})	$R_{a,n}$ (Å)	χ^2 (10^{-3})
at 25 °C	diffuse layer	2.5	1.0	0.0	0.6
	graphene	14.7	5.9	15.3	
	SiO_2	3000	4.5	18.8	
at 40 °C	DOPC-H	6.8	3.3	12.1	0.7
	DOPC-T	10.9	2.5	7.9	
	graphene	10.5	0.2	15.1	
	SiO_2	3000	4.5	18.8	
at 60 °C	DOPC-H	6.7	3.6	11.6	4.6
	DOPC-T	13.6	2.0	8.4	
	graphene	11.4	0.2	17.4	
	SiO_2	3000	3.6	18.8	
cooling to 25 °C	DOPC-H	7.4	6.5	11.7	2.0
	DOPC-T	11.1	2.7	8.1	
	graphene	10.4	0.6	16.6	
	SiO_2	3000	3.9	18.8	

Table S7 (continued)

DPPC in PBS on un-soaked graphene					
	Layers	t_n (Å)	ρ_n (10^{-6} Å^{-2})	$R_{a,n}$ (Å)	χ^2 (10^{-3})
at 25 °C	DPPC-H	7.3	2.8	13.4	1.9
	DPPC-T	18.9	4.5	8.3	
	diffuse layer	23.7	24.2	4.0	
	graphene	16.9	8.2	20.0	
	SiO_2	3000	3.1	19.0	
at 40 °C	DPPC-H	6.7	1.9	12.1	1.8
	DPPC-T	13.2	5.9	7.7	
	diffuse layer	23.7	19.8	3.7	
	graphene	15.7	6.3	19.6	
	SiO_2	3000	3.3	18.9	
at 60 °C	DPPC-H	6.7	4.0	12.1	2.5
	DPPC-T	13.8	6.4	7.7	
	diffuse layer	23.7	20.0	5.0	
	graphene	15.1	5.3	19.0	
	SiO_2	3000	4.0	19.0	

Table S7 (continued)

DOPC in PBS on soaked graphene

	Layers	t_n (Å)	ρ_n (10^{-6} Å^{-2})	$R_{a,n}$ (Å)	χ^2 (10^{-3})
rinsed at 25 °C	DOPC-H (o)	7.1	6.6	13.9	2.1
	DOPC-T (o)	15.7	5.0	7.9	
	DOPC-T (i)	13.2	7.7	8.0	
	DOPC-H (i)	7.3	6.5	13.2	
	ion adsorbed layer	9.3	4.6	21.5	
	graphene	4.5	0.9	17.7	
	silanol	78.9	2.5	20.2	
	SiO_2	3000	41.4	19.0	

DPPC in PBS on soaked graphene

	Layers	t_n (Å)	ρ_n (10^{-6} Å^{-2})	$R_{a,n}$ (Å)	χ^2 (10^{-3})
at 25°C	DPPC-H (o)	8.0	7.9	12.3	0.5
	DPPC-T (o)	21.4	13.1	8.8	
	DPPC-T (i)	22.3	0.8	8.5	
	DPPC-H (i)	7.3	4.2	12.7	
	ion adsorbed layer	11.4	1.2	20.2	
	graphene	4.3	2.4	15.4	
	silanol	77.5	8.0	20.2	

	SiO_2	3000	44.5	18.9	
at 40 °C	DPPC-H (o)	8.1	8.0	12.6	0.3
	DPPC-T (o)	15.2	13.0	8.2	
	DPPC-T (i)	20.4	0.3	8.0	
	DPPC-H (i)	8.4	4.6	12.6	
	ion adsorbed layer	11.1	2.0	20.9	
	graphene	5.5	2.2	15.9	
	silanol	77.8	5.0	21.0	
	SiO_2	3000	57.8	18.8	
at 60 °C	DPPC-H (o)	8.3	7.8	12.5	0.5
	DPPC-T (o)	16.0	12.9	7.7	
	DPPC-T (i)	20.7	6.9	7.9	
	DPPC-H (i)	8.4	3.9	12.7	
	ion adsorbed layer	12.0	0.7	20.7	
	graphene	5.0	2.4	15.7	
	silanol	78.8	5.0	21.0	
	SiO_2	3000	59.4	18.8	

Table S7 (continued)

at 60 °C after incubating for 3 h	DPPC-H (o)	12.0	10.0	12.8	0.4
	DPPC-T (o)	15.9	13.1	7.8	
	DPPC-T (i)	12.3	0.5	7.7	
	DPPC-H (i)	8.5	7.5	13.9	
	ion adsorbed layer	11.8	4.0	20.5	
	graphene	5.7	2.6	15.1	
	silanol	76.8	4.6	20.0	
	SiO_2	3000	50.2	18.7	
cooling to 25 °C	DPPC-H (o)	12.9	6.4	10.5	3.0
	DPPC-T (o)	11.2	10.0	9.3	
	DPPC-T (i)	20.9	3.5	8.3	
	DPPC-H (i)	8.4	4.3	13.5	
	ion adsorbed layer	12.3	4.2	20.1	
	graphene	5.8	2.6	15.1	
	silanol	76.4	3.1	20.3	
	SiO_2	3000	44.4	19.0	

Table S7 (continued)

rinsed at 25 °C	DPPC-H (o)	8.9	7.0	11.5	3.9
	DPPC-T (o)	12.6	10.1	8.4	
	DPPC-T (i)	20.2	0.0	8.4	
	DPPC-H (i)	7.5	4.9	13.1	
	ion adsorbed layer	12.6	4.8	20.5	
	graphene	5.4	2.1	14.9	
	silanol	78.6	3.8	20.5	
	SiO_2	3000	59.7	18.9	

VI. DOPC Multilayers Formed on Graphene

We have also studied the temperature triggered morphological changes of DOPC multilayers on graphene. However, the because the structures of the lipid multilayers were too disordered, the result and analysis we present here is not conclusive. Yet, it can be useful in the discussion of the interaction between lipids and graphene.

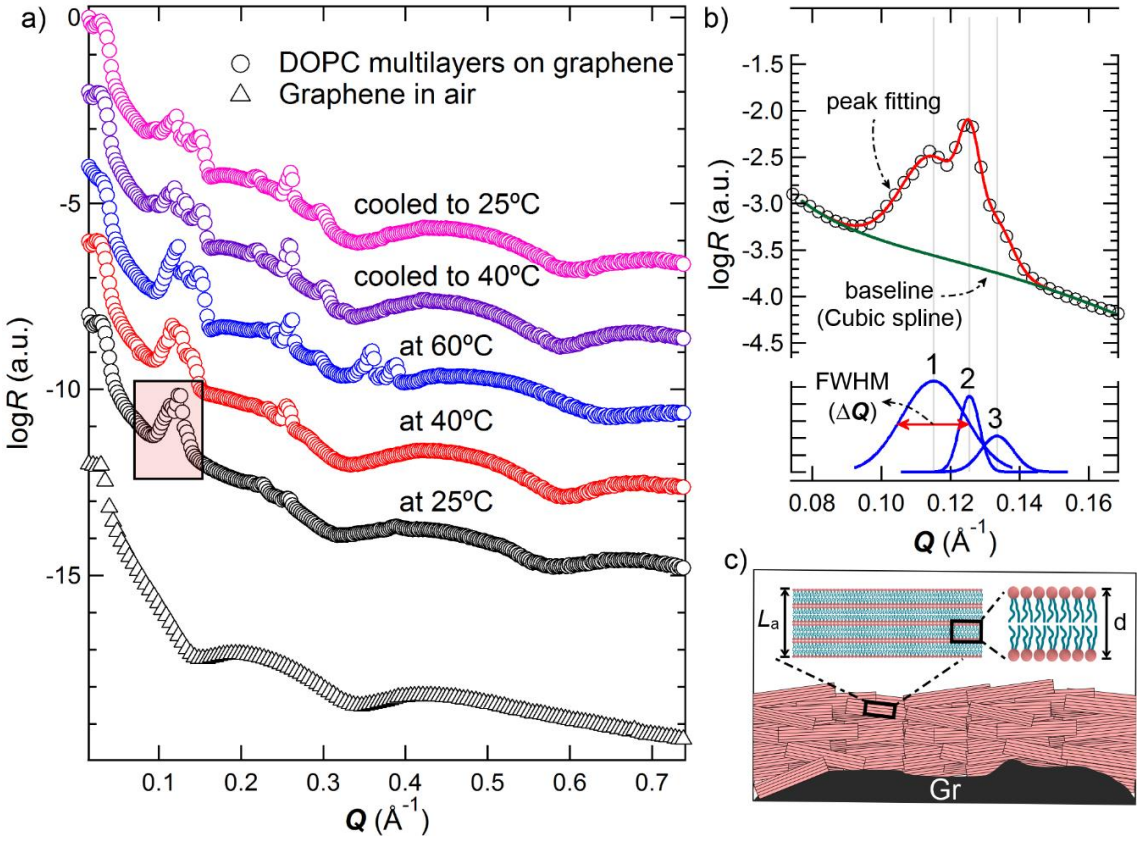

Figure S7. a) XRR curves (circles) of the drop-cast DOPC multilayer on graphene at different temperatures, in comparison to that of bare graphene (triangle), the reflectivity curves are offset for better comparison. Although the presence of Bragg peaks indicated periodic structures, the broad peak width and split peaks imply highly disordered structures. b) An example of peak fitting, showing the 1st order (n = 1) Bragg peak of the measurement at 25 °C highlighted in the rectangle in (a): the simulated Gaussian peaks (blue lines, i = 1, 2, 3) composing the fitting (red line) of the example Bragg peak (circles), and the base line (green line) fitted with a cubic spline of the vicinity. c) An illustration of the DOPC multilayer on graphene, comprised by domains (lipid bilayer) with a spacing of d and a coherence length of L_a (the mean domain size perpendicular to the substrate).

The XRR curves of the lipid multilayers on graphene at different temperatures are plotted in Figure S7. The multilayer was prepared by drop casting DOPC (dispersed in water) liposomes (D_z = ~ 120 nm) on an un-soaked bare graphene. The presence of Bragg peaks on the XRR curves (circles in Figure S7a) was a result of the diffractions from the periodical lattice planes, suggesting the formation of DOPC multilayers on graphene from drop-casting. However, according to a previous XRR study on DOPC multilayers on solid supports, in the $\boldsymbol{Q}$ range of 0 - 0.6 Å^{-1}, sharp Bragg peaks with 4th order of diffraction

(diffraction order, n = 4) have been observed [4] instead of the broad Bragg peaks with n = 3 at 60 °C, and n = 2 in other measurements, as we found on graphene. The missing Bragg peaks at higher $\boldsymbol{Q}$ range and the peak splitting can be attributed to the polymorphism of the DOPC multilayers on graphene. The existence of more than one plane distance would result in multiple Bragg angles, thus leading to peak splitting (*cf.* Figure S7b) at various of positions, $Q_{n,i}$ (i = 1,2,3…), of the n^{th} diffraction order, The magnitude of $Q_{n,i}$ with the same order, i, should be proportional to n, for example $Q_{1,1}$: $Q_{2,1}$ = 1:2. Based on the Bragg law, one can calculate the d-spacing (d), which is the distance between the smallest repeated lattice planes parallel to the substrate (*e.g* the lipid bilayer thickness in the multilayers) from

$$d = \frac{2n\pi}{Q_n}. \qquad \text{Equation 6.1}$$

$Q_{n,i}$ and its corresponding full width half maximum (FWHM ΔQ) can be obtained from the peak fitting of the Bragg peaks. The fittings were performed using the programme package *Multipeak* in *Igor Pro*. The fitted $Q_{n,i}$ and ΔQ of all the measurements are tabulated in Table S8, and $Q_{n,i}$ up to i = 7 were obtained, although some $Q_{n,i}$ could not be decomposed from the respective Bragg peak because of the insufficient angular resolution. An example of peak fitting (red lines) for the peak with n = 1 on the XRR curve collected at 25 °C is given in Figure S7b, in which the peak (circles) could be resolved to 3 Gaussian peaks (blue lines) due to the disordered multilayer structure, with the baseline (green line) fitted in the $\boldsymbol{Q}$ range of 0.08 - 0.17 $Å^{-1}$, using a Cubic spline. The $Q_{n,i}$ of the 3 fitted Gaussian peaks ($Q_{1,2}$ = 0.115 $Å^{-1}$, $Q_{1,4}$ = 0.115 $Å^{-1}$, $Q_{1,5}$ = 0.115 $Å^{-1}$, note that the 1st, 3rd, 6-7th could not be resolved at this Bragg peak), could yield 3 different d value accordingly ($d_{1,2}$ = 54.6 Å, $d_{1,4}$ = 50.1 Å, and $d_{1,5}$ = 47.1 Å) using Equation 6.1. The calculated d values roughly agree to our DOPC bilayer thickness observed in water (*cf.* Table 5.2).

Another parameter that can be used to describe the periodical structure of the DOPC multilayer is the coherent length (L_a), which is the mean crystalline domain size perpendicular to the substrate. An approximation of L_a can be calculated by Scherrer equation,

$$L_a = \frac{2\pi K}{\Delta Q}\ , \qquad \text{Equation 6.2}$$

where K is the Scherrer constant, which is related to the crystalline shape (*e.g.* for a cubic, $K \sim 0.9$, for an ellipsoidal particle, $K \sim 1.1$) [5]. In this case, we used $K = 1$, a value that has previously been used for analysing DOPC multilayers [4]. The calculated d and L_a of the DOPC multilayers on graphene at different temperatures plotted against n, are shown in Figure S8. The wide d and L_a ranges of all the measurements suggest the heterogenous DOPC multilayer structure on graphene. As discussed previously in section 5.3.1, the wettability of graphene is influenced by the nano-bubbles presented in its surface microstructure in aqueous medias. In addition, DOPC liposomes didn't show the adsorption on the un-soaked graphene. Therefore, we propose that the disordered multilayer structure was caused by the hydrophobicity and the low affinity between the un-soaked graphene and the DOPC liposomes. Because of the low attraction between DOPC liposomes and graphene, the lipid vesicles were forced by the applied vacuum to form multilayers or flattened liposome aggregates with no specific orientation on graphene. Moreover, during the drop-casting procedure, the bilayers in DOPC vesicles that were allocated near the air bubbles would need to un-zip into monolayers to spread at the air-water interface, with the hydrocarbon tails facing the graphene surface, which could lead to a smaller d-spacing and L_a, compared to those composed of intact DOPC bilayers.

In spite of the highly disordered lamellar structure, the DOPC multilayer on graphene showed a noticeable respond towards temperature, which can be directly distinguished from the XRR curves (Figure S7a) that at 60 °C an extra Bragg peak reversibly appeared around 0.35 - 0.39 $Å^{-1}$. Although, it is difficult to conclude a trend from the calculated L_a at different temperatures due to the large uncertainty (Figure S8c-d), the d-spacing, however, showed a reduction upon heating (Figure S8a). This phenomenon is largely in agreement with the "melting" behaviour we observed from the DPPC bilayer in PBS, which could be attributed to the lipid thermal expansivity at higher temperature as mentioned earlier in section 5.3.2. As the temperature went down, the d-spacing seemed to gradually expand to a level even larger than the initial (Figure S8b), and the extremely polydisperse d values indicate that the recovery of the bilayer thickness didn't happen simultaneously within the whole multilayer. However, here we have only studied a single

sample, so the XRR results of the DOPC multilayer are not conclusive, further investigation will need to be performed.

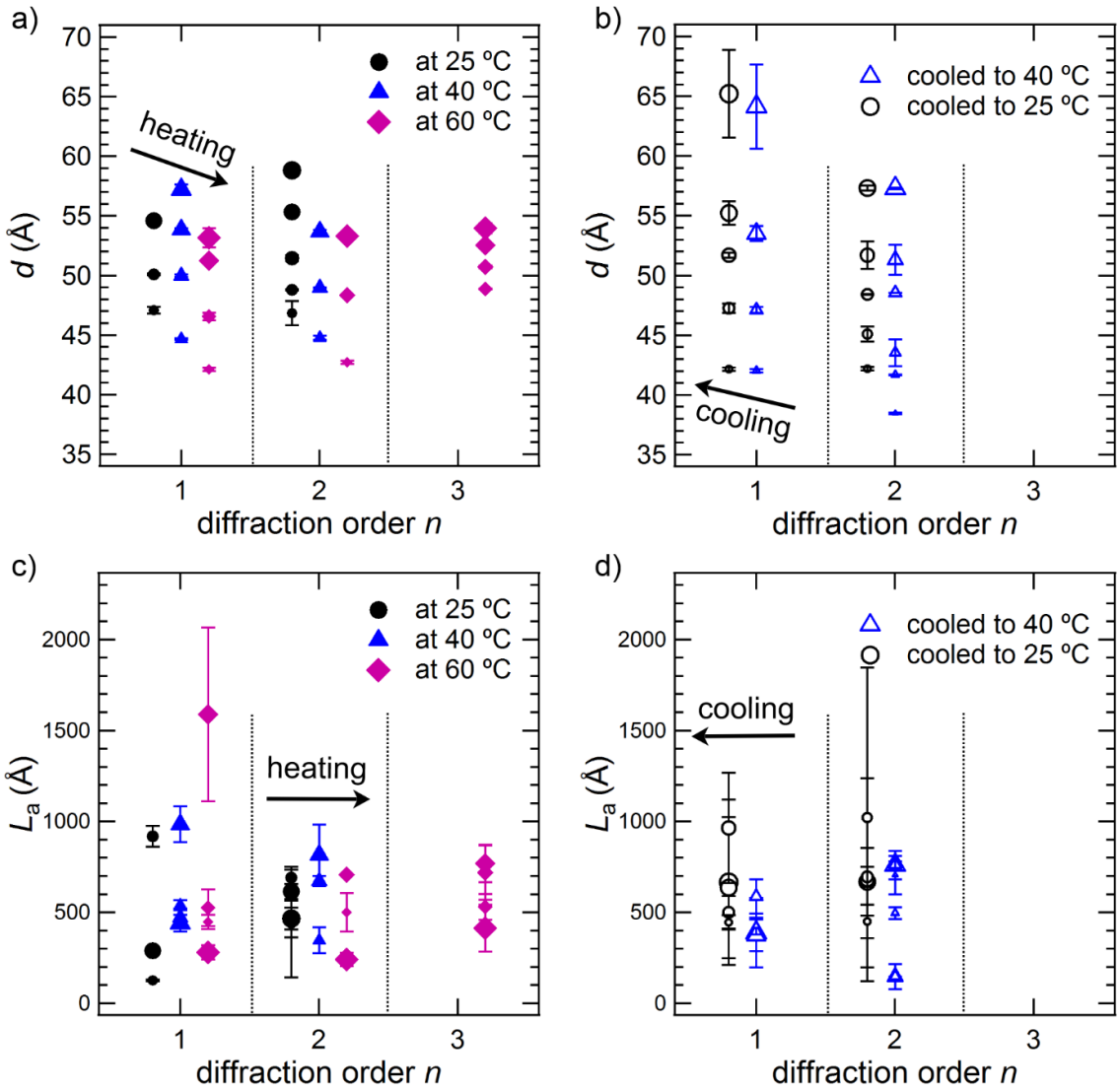

Figure S8. The calculated *d* (a and b) and L_a (c and d) of the DOPC multilayers on graphene at 25 °C (solid circles), 40 °C (solid triangles), 60 °C (solid diamonds), cooling to 40 °C (triangles), and cooling to 25 °C (circles), plotted against the diffraction order (*n*) on the same scale for comparison. Results obtained from different peak position were represented with different marker size, to access full results of the data, see Table S7 in SI-3. The large error bars can be attributed to the limited number of data points for fitting the resolved peaks.

The DOPC multilayer structure can be primarily described by the distance between the smallest repeated lattice planes parallel to the substrate (*d*-spacing, denoted as *d*) and the

mean crystalline domain size perpendicular to the substrate (coherence length, denoted as L_a), the two parameters can be calculated by Equation 6.1 and Equation 6.2 (Scherrer equation), from the peak position, $Q_{n,i}$, and the corresponding ΔQ of the i^{th} order peak decomposed from the Bragg peak of the n^{th} diffraction order, respectively. The fitted peak positions, the calculated d and L_a are listed in Table S8.

Table S8. Summary of the DOPC multilayer structure.

DOPC drop cast on graphene during heating							
	25 °C		40 °C		60 °C		
diffraction order *n*	1	2	1	2	1	2	3
$Q_{n,1}$ (Å^{-1})		0.214	0.110 ± 0.0008				
d (Å)		58.8	57.2 ± 0.4				
L_a (Å)		465.3 ± 59.1	440.7 ± 46.1				
$Q_{n,2}$ (Å^{-1})	0.115	0.227	0.117	0.234	0.118 ± 0.0018	0.236 ± 0.0013	0.349 ± 0.0028
d (Å)	54.6	55.3	53.9	53.7	53.2 ± 0.8	53.3 ± 0.3	54.0 ± 0.4
L_a (Å)	288.3 ± 12.7	615.4 ± 42.2	985.2 ± 99.5	817.8 ± 166.1	279.9 ± 38.7	240.7 ± 35.9	414.0 ± 129.2

Table S8 (continued)

$Q_{n,3}$ (Å^{-1})		0.244 ± 0.0012	0.126	0.257	0.123		0.359
d (Å)		51.4 ± 0.3	50	49	51.2		52.5
L_a (Å)		463.9 ± 100.1	473.8 ± 48.7	672.8 ± 28.6	1588.4 ± 477.0		769.8 ± 102.9
$Q_{n,4}$ (Å^{-1})	0.125	0.141	0.141	0.281		0.260	0.372
d (Å)	50.1	44.7	44.7	44.8		48.3	50.7
L_a (Å)	918.1 ± 56.8	691.6 ± 60.3	538.5 ± 27.0	347.3 ± 70.8		707.7 ± 40.4	718.5 ± 148.8
$Q_{n,5}$ (Å^{-1})	0.133 ± 0.0008	0.268 ± 0.0059			0.135 ± 0.0009		0.386
d (Å)	47.09 ± 0.3	46.8 ± 1.0			46.6 ± 0.3		48.9
L_a (Å)	126.9 ± 3.8	437.9 ± 296.2			525.5 ± 101.9		530.3 ± 71.7
$Q_{n,6}$ (Å^{-1})					0.149	0.294	
d (Å)					42.1	42.7	
L_a (Å)					447.4 ± 39.2	500.0 ± 106.6	

Table S8 (continued)

DOPC drop cast on graphene during cooling				
	cooled 25 °C		cooled 40 °C	
diffraction order *n*	1	2	1	2
$Q_{n,1}$ (Å^{-1})	0.0971 ± 0.0054		0.0989 ± 0.0054	0.219
d (Å)	65.2 ± 3.7		64.1 ± 3.5	57.3
L_a (Å)	665.0 ± 455.0		387.0 ± 191.4	759.7 ± 78.5
$Q_{n,2}$ (Å^{-1})	0.114 ± 0.0020	0.219	0.117 ± 0.0014	
d (Å)	55.2 ± 1.0	57.3	53.5 ± 0.6	
L_a (Å)	635.6 ± 388.9	668.1 ± 186.8	373.1 ± 88.1	
$Q_{n,3}$ (Å^{-1})	0.122	0.243 ± 0.0055		0.245 ± 0.0061
d (Å)	51.7	51.7 ± 1.2		51.3 ± 1.3
L_a (Å)	963.8 ± 302.3	680.0 ± 557.1		146.9 ± 69.9

Table S8 (continued)

$Q_{n,4}$ (Å^{-1})	0.133 ± 0.0011	0.26	0.133 ± 0.0007	0.259
d (Å)	47.3 ± 0.4	48.4	47.1 ± 0.2	48.6
L_a (Å)	499.8 ± 90.6	696.2 ± 54.2	587.6 ± 93.5	762.2 ± 19.1
$Q_{n,5}$ (Å^{-1})		0.279 ± 0.0039		0.289 ± 0.0074
d (Å)		45.1 ± 0.6		43.5 ± 1.1
L_a (Å)		1021.4 ± 823.9		146.4
$Q_{n,6}$ (Å^{-1})	0.149	0.298	0.15	0.302
d (Å)	42.1	42.2	42	41.7
L_a (Å)	446.0 ± 38.1	449.2 ± 92.1	424.7 ± 46.6	496.6 ± 33.2
$Q_{n,7}$ (Å^{-1})				0.327
d (Å)				38.5
L_a (Å)				703.9 ± 105.8

VII. Publications and manuscripts

Carbon 136 (2018) 255–261

Contents lists available at ScienceDirect

Carbon

journal homepage: www.elsevier.com/locate/carbon

Surface structure of few layer graphene

Liangzhi Zhou [a], Laura Fox [a, b], Magdalena Włodek [c], Luisa Islas [a], Anna Slastanova [a], Eric Robles [d], Oier Bikondoa [e, f], Robert Harniman [a], Neil Fox [a], Mattia Cattelan [a], Wuge H. Briscoe [a, *]

[a] School of Chemistry, University of Bristol, Cantock's Close, Bristol, BS8 1TS, UK
[b] Bristol Centre for Functional Nanomaterials, HH Wills Laboratory, University of Bristol, Tyndall Avenue, BS8 1TL, UK
[c] Jerzy Haber Institute of Catalysis and Surface Chemistry, Polish Academy of Sciences, Niezapominajek 8, Poland
[d] Household Care Analytical, Procter & Gamble Newcastle Innovation Centre Whitley Road, Longbenton, Newcastle, NE12 9TS, UK
[e] XMaS, The UK-CRG, European Synchrotron Radiation Facility (ESRF), 6 Rue Jules Horowitz, BP 220, 38043, Grenoble CEDEX 9, France
[f] Department of Physics, University of Warwick, Gibbet Hill Road, Coventry, CV4 7AL, UK

ARTICLE INFO

Article history:
Received 17 December 2017
Received in revised form
22 April 2018
Accepted 29 April 2018
Available online 2 May 2018

ABSTRACT

Understanding surface structure of graphene is important for its integration into composite materials. Here, we have used synchrotron X-ray reflectivity (XRR) to study the structure of commercially available graphene samples (prepared *via* chemical vapor deposition, and marketed as *graphene monolayers*) on SiO_2/Si at different temperatures. X-ray photoelectron spectroscopy, photoemission electron microscopy and atomic force microscopy (AFM) were employed to evaluate the composition and morphology of the graphene layer. Our results indicate that the samples we characterized consisted of 3–4 layers of graphene, which should thus be more accurately described as *few layer graphene* (FLG). Furthermore, a "contaminant" layer, comprising polymethylmethacrylate and graphene multilayers, was found present atop FLG. We also report tentative results on the effect of temperature on the graphene sample thickness. At 25 °C, the FLG thickness from XRR measurements was 13.0 ± 1.0 Å, in agreement with that obtained from AFM (13.9 ± 0.7 Å). Upon heating to 60 °C, the FLG thickness expanded to 13.8 Å, which further increased to 14.3 Å upon cooling to 25 °C. We attribute this temperature dependent thickness to the out-of-plane rippling of graphene as previously reported. These unprecedented results on the FLG surface structure are valuable to its potential bioanalytical applications.

1. Introduction

Graphene is a one-atom thick, flat, carbon monolayer with a hexagonal carbon aromatic structure. As one of the basic carbon allotropes, it can be transformed into other carbon materials, such as carbon nanotubes and fullerenes. Since the 1970s, studies on growing graphene monolayers on crystals have been carried out, and the first graphene was successfully exfoliated in 2004 by Novoselov and Geim [1]. The unique 2D electronic properties of graphene have since stimulated numerous studies aiming to develop its use in applications such as supercapacitors, batteries, interconnects, transistors, phonon detectors, and sensors *etc.*[2]. Concurrently, advances in the production and modification of graphene sheets have continued to stimulate interest in its potential application in biotechnology [3]. For instance, the surface charging of graphene due to ion adsorption has been exploited to monitor pH changes [4] and lipid membrane disruptions [5].

One of the most promising methods for producing high quality graphene on an industrial scale is chemical vapor deposition (CVD), which involves depositing graphitic layers atop another crystalline substrate, such as SiC [6], Ni [7], and Cu [8]. A polymethylmethacrylate (PMMA) coating is deposited atop *via* spin coating, and then the graphene can be transferred onto a desired substrate (*e.g.* SiO_2) after the original substrate is removed by chemical etching [9–12]. Graphene prepared by the CVD method has been reported to exhibit an electronic spectrum that can be described by a 2D analogue of the Dirac equation, similar to that of free-standing graphene [3]. Among all the substrates, Cu attracted particular attention. As confirmed by Raman spectroscopy, graphene deposited on Cu by the CVD method could yield over 93%

* Corresponding author.
E-mail address: wuge.briscoe@bristol.ac.uk (W.H. Briscoe).

https://doi.org/10.1016/j.carbon.2018.04.089

coverage (with the rest consisting of 2–3 layer graphene), thanks to its weak interaction with graphene which benefits 2D crystal growth, thereby generating monolayer graphene on the Cu surface [13]. However, it is known that one of the issues with the transferred CVD graphene is the residues of PMMA and etching agents [9–12].

Previous studies have shown that the physical properties of graphene materials are determined by their structure, specifically the thickness and the defects or contaminants. For example, the thermal conductivity of graphene materials increases with the layer number, with monolayer, double-layer, and *few layer graphene* (FLG) (3–10 layers) showing different 2D electronic properties [14,15]; the transport properties in epitaxial graphene are influenced by its sp^2 aromatic lattice structure, which is in turn affected by its substrate and growth conditions [16,17]; and the presence of ripples and wrinkles on graphene is expected to have a negative effect on its electronic properties [13]. Thus, a precise determination of the thickness and morphology of graphene samples under different conditions is important.

Different techniques have been employed for the structural characterisation of graphene and its derivatives, as listed and compared in Table S1 in the Supporting Information (SI). For instance, graphene on silica was first revealed by optical microscopy, scanning electron microscopy (SEM), and atomic force microscopy (AFM) [1]. Non-destructive techniques such as electron microscopy (EM), Raman/Rayleigh scattering microscopy [10], ellipsometry [11,12], and near edge X-ray absorption spectroscopy (NEXAS) [18,19] have been used to study the graphene structure and/or its adsorbates. For the in-plane structural characterisation, scanning tunnelling microscopy (STM) and scanning tunnelling spectroscopy (STS) [8,13,16,25] have been used to image the graphene lattice. X-ray photoelectron spectroscopy (XPS) and Auger electron spectroscopy (AES) [6,26,27] assisted by low energy electron microscopy (LEEM) and photoemission electron microscopy (PEEM) measurements [17,25,28–30] have also been employed for the compositional, structural and morphological characterisation of graphene on conductive substrates. AFM [20], total internal reflection fluorescence correlation spectroscopy (ITIR-FCS) [5], and quartz crystal microbalance with dissipation monitoring (QCM-D) [20] have been used to study lipid adsorption on graphene and related systems. However, these techniques have a limited capacity to probe the out-of-plane structure of the adsorbed layer.

Another powerful technique is X-ray reflectivity (XRR), which is widely used for probing buried interfaces and thin film monolayers [21], bilayers [22,23] and multilayers [24] structures. XRR has been used to study the structure of graphene coated with other popular materials in electronic devices (*e.g.* HfO_2 [25], Au [26], and perylenetetracarboxylic dianhydride (PTCDA) [27]), and exposed and buried interfacial structures of graphene grown on SiC [28,29], showing its potential to be used on the structural characterization of graphene.

In this study, commercially available graphene samples on Si/SiO_2 widely used in the studies of graphene applications have been studied using synchrotron XRR. XPS, PEEM and AFM were also used to provide complementary information on the composition and morphology of the samples. Our findings are valuable to graphene research and applications, and also demonstrat the suitability of XRR as a sensitive method for characterising the graphene surface structure, paving the way for further investigations of biomolecular structures on graphene using XRR.[1]

2. Experimental methods

2.1. Materials

Graphene samples prepared by an established CVD method were purchased from *Graphenea Inc.*[2] Briefly, the preparation process involves chemical vapor deposition of methane on a copper (Cu) foil to produce a graphene (mono)layer. Then a PMMA coating is deposited atop *via* spin coating, before the copper foil is etched away. Finally, the graphene is transferred onto a 1 cm × 1 cm Si wafer with a 300 nm SiO_2 top layer. Graphene produced is being marketed as "*monolayer graphene*", and is widely used in the studies to evaluate potential application of graphene monolayers in electronic devices.

2.2. Experiment methods

The AFM investigation was conducted in ambient conditions using a MultiMode VIII microscope with a NanoScope V controller, utilizing PeakForce feedback control (Bruker, CA, USA). The cantilever employed was SCANASYST_FLUID+ with nominal spring constant and tip radius of 0.7 N m^{-1} and 2 nm respectively.

XPS and PEEM measurements of the graphene samples were performed at the Bristol NanoESCA facility. XPS measurements of the FLG were performed with an Argus spectrometer before and after annealing at 450 °C at an ultra-high vacuum (UHV) base pressure of 4.0×10^{-11} mbar for 1 h. Core-level photoemission spectra were acquired at 45° w.r.t. the sample surface, using a monochromatic Al Kα (1486.7 eV) X-ray source with a pass energy of 20 eV at room temperature and an estimate total energy resolution of 600 meV. The relative composition of C, O, and Si can be calculated from their corresponding photoemission line intensities.

The PEEM was performed using a NanoESCA II, and the measurements were carried out at room temperature under the UHV condition with a pass energy of 50 eV, a lateral resolution of 150 nm, and an overall energy resolution of 140 meV. The energy calibration was confirmed by fitting a Fermi edge of a clean metallic substrate at the same measurement condition. A He I (21.2 eV) discharge lamp was used as excitation source, and the absolute work function measurement for a particular sample area was obtained from electronic counting of the emitted photoelectrons [30]. The work function values in the maps were obtained by fitting the 600 × 600 camera pixels spectra with an "error function". The low excitation photon energy makes PEEM extremely surface sensitive (to 2–3 atomic surface layers), and the PEEM images were acquired after cleaning by annealing to show the surface morphology.

Synchrotron XRR measurements were performed at beamline BM28-XMaS, European Synchrotron Radiation Facility (ESRF), Grenoble, France. A custom designed sample cell was used in all XRR experiments, as shown schematically in Fig. 1 [23,31]. The cell, originally designed to accommodate the "bending mica method" [21], consists of a chamber to house the sample stage for both curved and flat substrates. Temperature control in the range 10–90 °C is facilitated by two brass jackets sandwiching the chamber, one to house electrical heaters and the other connected to a water bath to provide cooling. Graphene samples were mounted on the sample stage in the XRR cell, which was sealed *via* two polyester (Mylar®) windows.

The X-ray beam energy was 14 keV (wavelength $\lambda = 0.8856$ Å), and the incident beam size defined by aperture slits was 100 μm (vertical FWHM) × 255 μm (horizontal FWHM). XRR scans were

[1] L. Zhou et al., "Evidence for air bubble formation on graphene surface in water", in preparation.

[2] https://eu.graphenea.com/.

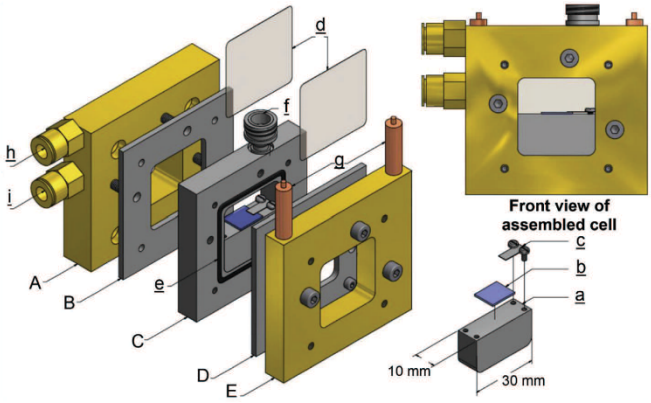

Fig. 1. Key components of the XRR cell, consisting of three stainless steel plates (B–D), and the cooling (A) and heating jackets (E). Two Mylar® windows (d) are clamped between plates B, D and plate C, creating a liquid chamber with a capacity of 5 ml. Sealing is facilitated by means of O-rings placed in grooves (e). The samples (b) 1 cm × 1 cm in size are clamped by two small plates (c), onto a stainless steel stage (a). A nozzle (f) allows *in situ* liquid/gas exchange. The heating jacket can be controlled by two heaters (g) while the cooling jacket can be connected to a water circulating bath *via* an inlet (i) and an outlet (h). (A colour version of this figure can be viewed online.)

collected at 25 °C, 40 °C and 60 °C in air, with the incident angle θ_i varying from 0.06 to 3.0°, corresponding to a **Q** range of 0.015–0.74 Å^{-1}, where the vertical momentum transfer vector $\mathbf{Q} = 4\pi\sin\theta/\lambda$. The specular reflections were detected at each angle ($\theta_r = \theta_i$) using an Avalanche Photodiode Detector (APD). XRR data fitting was performed by using *Motofit* in *Igor Pro* (WaveMetrics, Inc., Lake Oswego, OR, USA) [32]. For reflectivity data collected on a well-defined flat substrate such as silicon, the surface layer was modelled as stacked homogeneous slabs. Each layer can be described by three parameters: the scattering length density (SLD, ρ), thickness t, and inter-slab roughness R_a. These parameters were varied in the total reflectivity calculation using the Abeles matrix method, and a genetic algorithm optimisation was adopted to obtain the best fitting for the curves. This generates the same result as Parratt's Recursive method [32]. The analysis of XRR results is described in the Supporting Information (SI) section SI-2.

Ellipsometry was performed using a J.A. Wollam M-2000 ellipsometer (J.A. Woollam Company, Incorporated, Lincoln, NE, USA), to obtain the total thickness of the graphene sample, using a white light source (wavelengths of 245–1000 nm) at a fixed incident angle of 75°. The obtained data was processed and fitted using VASE 32 software from J.A. Wollam adopting a three-layer model (consisting of a silicon substrate, a silicon dioxide layer and a graphene layer). The static contact angle of a water droplet on the graphene sample was 76.77°±0.53° as measured using the Sessile drop method on KRÜSS® DSA100 (see SI-5).

It is useful to compare the footprint size of different complementary methods when interpreting the results. For XPS it was approximately an oval with major/minor axes of 3mm/2 mm; for PEEM it was 60 μm × 60 μm; for XRR it was 255 μm × 1 cm (the projection of the vertical beam size onto the sample); for ellipsometry the circular spot size was ~3 mm in diameter; for AFM, the scan size was either 5 μm × 5 μm or 1 μm × 1 μm; and for the contact angle measurement, the diameter of the water droplet was of ~3.3 mm. As such, AFM and PEEM provided localised morphological and chemical information, whilst XRR, XPS, ellipsometry, and contact angle provided average structural information across a larger sample area. It is also worth bearing in mind the different conditions for these measurements: XPS and PEEM were carried out under UHV (3×10^{-11} mbar), whilst the rest of the measurements were performed under ambient conditions.

3. Results and discussion

The XPS spectra from the survey scans of a wide bonding energy range on the FLG sample before and after annealing in UHV at 450 °C are shown in Fig. 2a. In both cases, only the presence of C, O, and Si was observed, and no metal residues from the original copper substrate and the etchant were observed on the sample. The elemental compositions estimated from the spectra show that, before annealing, the atomic composition of C, O, and Si was 32.2%, 36.7% and 31.1%, respectively; and after annealing, the percentage of C decreased to 17.4%, but those of O and Si increased to 42.6% and 40.0%, respectively. The C 1s photoemission lines before and after annealing in Fig. 2b show clear differences in their shape and relative intensity. Deconvolution of these photoemission lines (Fig. 2c and d; Table S4) indicates the presence of C 1s (sp^2 and sp^3), C-OH and O-C=O [33–35] before annealing, whereas after annealing, the intensity of the C-OH and C=O peaks dropped remarkedly.

The CVD method is known to produce graphene with an ordered structure and exceptional electronic properties. However, the substrates on which graphene can be grown are limited, and typically transition metals are used. Subsequently, epitaxial graphene often needs to be transferred from the original growth substrate, a process that could cause contamination [9,10,12]. In this case, there were four possible types of contaminants: the multilayer graphene formed on top of the single layer graphene, the PMMA used for transferring, residues due to incomplete Cu dissolution [11,36], and etchant liquid residues (typically $FeCl_3$). We ascribe the observed changes in the XPS carbon peaks in Fig. 2 to PMMA residues being removed by the annealing procedure. This explanation is consistent with the observed decreased C composition (from 32.2% to 17.4%) and C/Si ratio (from 1.03 to 0.44) after annealing. Note that the XPS detection limit was ~0.1 atomic% in our measurements.

The annealed samples were further investigated by PEEM, an extremely surface sensitive technique, to reveal their surface morphology, which also helps to identify any possible

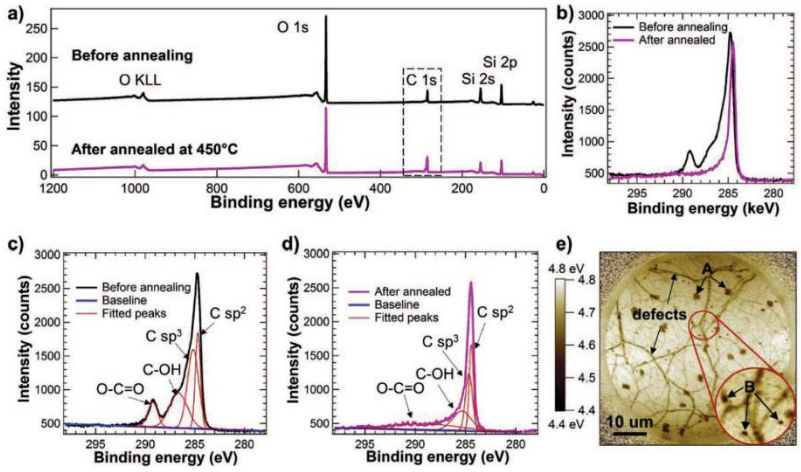

Fig. 2. a) The XPS surveys for the graphene sample measured before (black line) and after (pink line) annealing. b) shows the C 1s photoemission region highlighted in the dashed rectangle in a), and the fittings for the photoemission lines before and after annealing are shown in c) and d), respectively. The fittings suggest the existence of carbon oxides in the sample, including O-C=O and C-OH, with the peak energy values listed in Table S4 in SI-3. After annealing, the amount of the oxides decreased. e) The work function map of graphene annealed at 450 °C for 1 h, with 2 types of contaminants labelled as **A** and **B**. (A colour version of this figure can be viewed online.)

contaminants on the graphene surface due to the contrast in their work function. Work function is the energy needed to excite an electron from the Fermi level of the material to free space. An example work function map in Fig. 2e shows darkened (lower work function) lines and spots appearing on a continuous light background (higher work function). We attribute the dark lines to defects (cracks) likely caused by the transferring process [9], and the spots to two types of contaminants (examples labelled as **A** and **B** on Fig. 2e). Contaminants **A** (of size ~2 μm) were found sparsely over the sample surface, while **B** (of size ~500 nm) were found in the vicinity of the defects. The work function of annealed graphene (*i.e.* the light background in Fig. 2e) was ~4.7–4.8 eV, which is slightly larger than the reported work function of intrinsic graphene (4.56 eV) [37]. This difference could be related to the redistribution of electrons between the substrate and graphene [7,38,39]. Upon annealing, the defects and contaminants **A** remained, whereas contaminants **B** with a lower work function of ~4.3–4.6 eV gradually disappeared. We thus attribute **B** to PMMA residues from the transferring process of the graphene from its Cu substrate during fabrication. These PMMA residues were removed upon annealing at 450 °C, an interpretation consistent with a previous study which showed that PMMA was burnt off from the graphene surface at high temperatures in UHV [11,36].

The formation of multilayer graphene with a size of few micrometres on monolayer graphene grown on Cu has been previously characterised by Raman spectroscopy [8]. FLG with more than 3 graphene monolayers exhibited a work function of 4.6 eV, similar to that of graphite [7,40,41]. Thus, contaminants **A** with a work function of ~4.6 eV were likely graphene multilayers.

Fig. 3a shows a topographic AFM image on a1 μm × 1 μm scale, and three line profiles along the coloured lines (with arrows pointing towards the directions of the profiles taken) are shown in Fig. 3b shown in the corresponding colours. By analysing the topological histograms of the AFM images, the position and the thickness of the FLG layer can be obtained, as described in SI-4. The highlighted areas in the line profiles represent the position of the graphene layer from the histogram analysis, and the PMMA residues with thickness in the range of 0–57 Å were seen on top of the graphene surface. Fig. 3c shows an AFM topological image over a larger scale (5 μm × 5 μm), indicating the deposited graphene appeared continuous with a number of defects (dark holes, *i.e.* **1** in Fig. 3c) of size ~100 nm and a small number of PMMA residues appearing as elevated (lighter) spots. The PMMA residues varied in size (~10–100 nm), and two such spots (**2 and 3**) are circled in the figure. The red rectangle (**4**) in Fig. 3c highlights a crack defect on the graphene surface with PMMA partially filling the crack. This interpretation agrees with the work function map (Fig. 2e), where PMMA was detected around the defects. The apparent thickness of the graphene layer from the height histogram on a scale described in SI-4 is 13.9 ± 0.7 Å, which includes any (small) spacing between graphene and the underlying SiO_2 substrate. The graphene layer thickness points to the presence of the FLG instead of a graphene monolayer, in agreement with numerous AFM studies determining the thickness of graphene and FLG on flat substrates, with the reported thickness ranging from 3.5 Å to 15 Å, depending on the fabrication method and the AFM imaging [1,42–44].

Assuming PMMA residues existed mostly atop the measured sample, from the height histogram analysis, the graphene coverage on SiO_2 was ϕ_g 85.1 ± 2.1%, as described in SI-4. However, if the graphene did not remain intact during the transferring process, PMMA could have been transferred onto silica instead of graphene; in that case, the graphene coverage would have been overestimated, whilst that of PMMA underestimated.

The XRR curves of the graphene samples are shown in Fig. 4b. These curves were collected at 25 °C, 40 °C and 60 °C, and after the sample was cooled back down to 25 °C after heating. It is interesting to study such a temperature effect, given its relevance to potential biomedical applications of graphene. These results are representative from two separate synchrotron experiments on two different batches of samples from the same supplier. The open

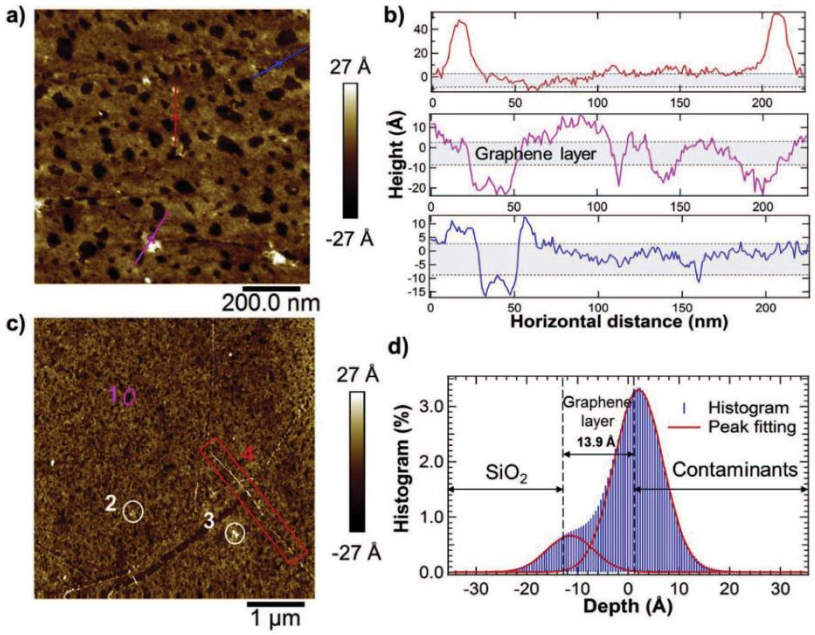

Fig. 3. a) An example AFM scale topological image on a 1 μm × 1 μm scale; b) Three line profiles followed the direction of the coloured arrow lines in a), with the grey highlighted areas attributed to the graphene layer; c) An example AFM topographic image on a 5 μm × 5 μm scale, highlighting PMMA residues (*e.g.* **2**, **3**) on a continuous graphene layer with holes (*e.g.* **1**) and defects (*e.g.* **4**) exposing underlying SiO_2; d) the corresponding histogram shows the height distribution of SiO_2, graphene, and the contaminant layer. (A colour version of this figure can be viewed online.)

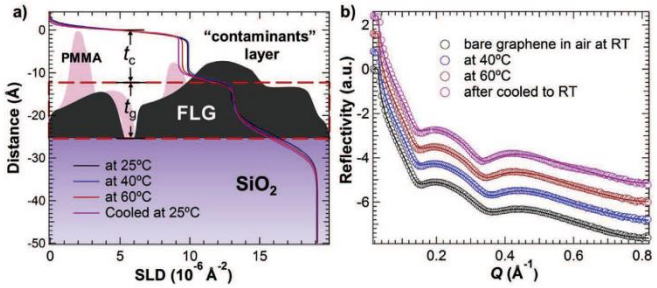

Fig. 4. a) The fitted SLD profile of the graphene sample at different temperatures with the corresponding physical model used for the fitting. Here, t_c and t_g are the thickness of the 2 slabs representing the contaminants and graphene, respectively. b) The open circles and solid lines are corresponded to the collected XRR data points and fits on a log scale of graphene plotted against **Q** at different temperatures (with the curves offset vertically for clarity). The fitting parameters are listed in Table 1. (A colour version of this figure can be viewed online.)

circles are the experimental data points, and the solid red lines the fits using a three-layer model, with the details of XRR analysis given in SI-2. The morphology and thickness measurement of graphene from AFM imaging (*cf.* Fig. 3) indicates that the graphene sample was not a graphene monolayer, but more likely FLG. PEEM (*cf.* Fig. 2) suggests that a "contaminant" layer was present atop the graphene layer, which was likely a mixture of graphene multilayers and PMMA residues. Therefore, when analysing the XRR data, we have used a three layer model (Fig. 4a): a contaminant layer (of thickness t_c) atop a graphene layer (t_g) attached to the substrate with a SiO_2 layer (t_s). The fitted thickness (t), inter-layer roughness (R_a) and SLD (ρ) are listed in Table 1. Overall, the structural information from fitting the XRR data is consistent with the observations from AFM and PEEM measurements.

Table 1
Fitting parameters for XRR results of graphene in air at different temperatures, using the three-layer model (*cf.* Fig. 4a). The SLD (ρ) of graphene and SiO_2 were fixed during fitting, and that of the contaminant layer was fitted in the range between air to graphene, since it is presumed a layer of a mixture with limited coverage instead of a homogeneous film. Also listed are the two fitted interfacial roughness values, $R_{a,c}$ for the roughness at the interface between air and the "contaminant" layer (thus the subscript c) and $R_{a,g}$ for that at the interface between the "contaminant" layer and the graphene layer.

T (°C)	t_g (Å)	$R_{a,g}$ (Å)	ρ (10^{-6} Å^{-2})	ϕ_g (%)	t_c (Å)	$R_{a,c}$ (Å)	ρ (10^{-6} Å^{-2})	χ^2 (10^{-3})
25	12.9	0.9	12.91	70.9	11.8	1.2	9.80	1.21
40	13.4	1.0	13.06	71.8	11.6	1.1	9.90	1.85
60	13.8	1.3	13.13	72.2	11.8	0.9	9.47	4.57
25 (Cooled)	14.3	1.3	13.08	71.9	11.7	0.7	9.19	9.72

The average fitted XRR thickness of four different graphene samples from two different sample batches at 25 °C was $t_g = 13.0 \pm 1.0$ Å (Table S3), slightly smaller than the AFM thickness of 13.9 ± 0.7 Å (Fig. 3d), which nonetheless is broadly consistent with the conclusion that the graphene layer was FLG with an average of 3–4 graphene monolayers. This is probably due to XRR measurements giving an average thickness over a much larger footprint (~10^6 μm^2), while AFM measures the local apparent thickness (with a footprint of ~1 μm^2) that is affected by the interaction between the tip and the surface. The total thickness of graphene and the contaminant layers from XRR fitting was ~25 Å, close to the thickness (27.1 ± 0.8 Å) obtained from the ellipsometry measurement on the same graphene samples.

The coverage of each layer can be calculated by comparing the fitted ρ with theoretical values, *i.e.* $\phi = \rho_{fitted}/\rho_{calculated}$. The fitted ρ values of each layer are shown in, the theoretical ρ of each material is listed in Table S2; the calculated SLD for graphene is $\rho_g = 1.820 \times 10^{-5}$ Å^{-2} at 14 keV. The graphene coverage at room temperature from XRR is $\phi_g = 76.3 \pm 7.0\%$, broadly consistent with the value ϕ_g ~$85.1 \pm 2.1\%$ estimated from AFM imaging, with the discrepancy again ascribable to the differences in the footprint size the two techniques probe. As such, the XRR ϕ_g value is an average over a much larger sample area, compared to the localised information from AFM imaging.

An interesting observation is that the graphene layer thickness t_g experienced a subtle expansion from 12.9 Å at 25 °C to 13.8 Å at 60 °C, and the roughness $R_{a,g}$ from 0.9 Å to 1.3 Å correspondingly. Meanwhile, the thickness of the contaminant layer remained largely constant at $t_c = 11.7$ Å, but its roughness $R_{a,c}$ decreased from 1.2 Å to 0.9 Å from 25 °C to 60 °C, suggesting a possible "curing" procedure upon heating, leading to a reduction of the roughness. The $R_{a,c}$ value continued to decrease to 0.7 Å, suggesting possible further relaxation. Furthermore, this change in the graphene layer thickness was irreversible; since after cooling to 25 °C, t_g further increased slightly to 14.3 Å. This observation might be explained by the out-of-plane motion of graphene, which may also be considered as a perpendicular thermal expansion or enhanced surface ripples. Unlike most of other materials, including SiO_2 and PMMA, graphene was demonstrated both theoretically and experimentally to have a negative in-plane thermal expansion coefficient (TEC) below ~500 K, as a consequence of decreasing phonon energies exhibited by 2D materials with smaller lattice parameters (rippled) upon heating, in contrast to increasing phonon energies in bulk materials [45–47]. In addition, the asymmetric bond length distribution of graphene caused by the delocalized p-cloud and the structural defects forces graphene to become non-planar to minimize free energy [48]. The rippling of graphene supported by Si/SiO_2 upon heating above 200 K was observed with SEM [49] and Raman spectroscopy [47]. When graphene attached to a SiO_2 substrate is heated, the graphene layer would experience an in-plane compressive stress because of its negative TEC, while SiO_2 would have experienced a tensile stress. Once the force applied on graphene exceeds the vdW attractive force between graphene and the substrate (normally at higher temperature), graphene might escape from the underling layer to enhance the amplitude of the ripples. This is also consistent with our observation that, after cooling back to room temperature, the graphene layer thickness detected by XRR further increased. This could be attributed to the tension on the graphene being smaller than the pining force, and the graphene stayed attached to the substrate, manifesting in enhanced rippling. We should acknowledge that our conclusions on the temperature dependence of the graphene sample thickness are tentative at this stage, and more measurements are needed to further verify these interesting and important observations.

4. Concluding remarks

The physical properties of graphene are intimately dependent on its thickness and surface structure. Understanding the surface structure of graphene is also important to its integration in composite materials and its bioanalytic applications. In this study, XRR was used to study the thickness of commercially sourced graphene prepared using the CVD method on Si/SiO_2 in air at different temperatures for the first time. Such graphene samples have been widely used in research and applications on monolayer graphene. Complementary techniques as AFM, XPS, and PEEM have been used to provide information on topography and chemical compositions of the graphene layer. Our XRR and AFM results show that the thickness of the graphene layer was ~13.0 ± 1.0 Å and 13.9 ± 0.7 Å, respectively, corresponding to 3–4 graphene monolayers. As such, the samples we characterized appeared to consist of 3–4 monolayers of graphene. This may suggest that other such commercial graphene samples are not of monolayer character. Given that XRR has not been previously widely used for studying the graphene structure, we hope to stimulate further investigations rather than regarding our conclusions as certainty and applicable to all commercial graphene samples. The XPS and PEEM results suggest the presence of PMMA residues from the transfer process of graphene fabrication. In addition, isolated islands of multilayer graphene were also present atop the FLG layer. We also observed a slight but detectable increase of 0.5–0.9 Å in the graphene layer thickness as it was heated from room temperature to 60 °C. This thermal expansion was irreversible, with the graphene thickness increasing a further 0.5 Å upon cooling back to room temperature. Such temperature dependent graphene thickness could be attributed to the out of plane rippling behaviour of graphene upon heating as previously reported. We should acknowledge that our conclusions on the temperature dependence of the graphene sample thickness are tentative at this stage, and more measurements are needed to further verify these interesting and important observations. These results on the FLG surface structure and chemistry are valuable to its potential bioanalytical applications where its interactions with biomolecules are an important consideration.

Acknowledgement

We acknowledge funding from the Engineering and Physical Science Research Council (EPSRC EP/H034862/1, and EP/L016648/1

through the *Bristol Centre for Functional Nanomaterials* (BCFN)), the Royal Society, Taiho Kogyo Tribology Research Foundation, the European Cooperation in Science and Technology (CMST COST) Action CM1101, the Marie Curie Initial Training Network (MC-ITN) "*Soft, Small, and Smart: Design, Assembly, and Dynamics of Novel Nanoparticles for Novel Industrial Applications (NanoS3)*" (FP7 Grant No. 290251), and the Consejo Nacional de Ciencia y Tecnologia (CONACyT) Postdoctoral Fellowship 291231. We also thank Procter & Gamble for financial support via the Bristol Final Year Industrial Project Scheme. Synchrotron X-ray access at EPSRC funded ESRF CRG XMas beamline and the support by the beamline staff is acknowledged.

Appendix A. Supplementary data

Supplementary data related to this article can be found at https://doi.org/10.1016/j.carbon.2018.04.089.

References

[1] K.S. Novoselov, A.K. Geim, S.V. Morozov, D. Jiang, Y. Zhang, S.V. Dubonos, et al., Electric field effect in atomically thin carbon films, Science 306 (5696) (2004) 666–669.
[2] K.S. Novoselov, V.I. Fal'ko, L. Colombo, P.R. Gellert, M.G. Schwab, K. Kim, A roadmap for graphene, Nature 490 (7419) (2012) 192–200.
[3] A.K. Geim, Graphene: status and prospects, Science 324 (5934) (2009) 1530–1534.
[4] P.K. Ang, W. Chen, A.T.S. Wee, K.P. Loh, Solution-gated epitaxial graphene as pH sensor, J. Am. Chem. Soc. 130 (44) (2008) 14392. -+.
[5] P.K. Ang, M. Jaiswal, C. Lim, Y. Wang, J. Sankaran, A. Li, et al., A bioelectronic platform using a graphene-lipid bilayer interface, ACS Nano 4 (12) (2010) 7387–7394.
[6] D.C. Wang, Y.M. Zhang, Spectroscopic and scanning probe analysis on large-area epitaxial graphene grown under pressure of 4 mbar on 4H-SiC (0001) substratesl, Chin. Phys. B 23 (7) (2014) 6.
[7] R. Kadowaki, M. Kuriyama, T. Abukawa, K. Sagisaka, D. Fujita, PEEM and micro PES study of graphene growth on Ni(110) substrate, E-Journal of Surface Science and Nanotechnology 13 (2015) 347–351.
[8] W. Liu, H. Li, C. Xu, Y. Khatami, K. Banerjee, Synthesis of high-quality monolayer and bilayer graphene on copper using chemical vapor deposition, Carbon 49 (13) (2011) 4122–4130.
[9] X.S. Li, Y.W. Zhu, W.W. Cai, M. Borysiak, B.Y. Han, D. Chen, et al., Transfer of large-area graphene films for high-performance transparent conductive electrodes, Nano Lett. 9 (12) (2009) 4359–4363.
[10] S. Unarunotai, Y. Murata, C.E. Chialvo, H.S. Kim, S. MacLaren, N. Mason, et al., Transfer of graphene layers grown on SiC wafers to other substrates and their integration into field effect transistors, Appl. Phys. Lett. (20) (2009) 95.
[11] J.W. Suk, A. Kitt, C.W. Magnuson, Y.F. Hao, S. Ahmed, J.H. An, et al., Transfer of CVD-grown monolayer graphene onto arbitrary substrates, ACS Nano 5 (9) (2011) 6916–6924.
[12] J.D. Caldwell, T.J. Anderson, J.C. Culbertson, G.G. Jernigan, K.D. Hobart, F.J. Kub, et al., Technique for the dry transfer of epitaxial graphene onto arbitrary substrates, ACS Nano 4 (2) (2010) 1108–1114.
[13] C. Mattevi, H. Kim, M. Chhowalla, A review of chemical vapour deposition of graphene on copper, J. Mater. Chem. 21 (10) (2011) 3324–3334.
[14] M.S. Xu, D. Fujita, J.H. Gao, N. Hanagata, Auger electron spectroscopy: a rational method for determining thickness of graphene films, ACS Nano 4 (5) (2010) 2937–2945.
[15] W.Y. Jang, Z. Chen, W.Z. Bao, C.N. Lau, C. Dames, Thickness-dependent thermal conductivity of encased graphene and ultrathin graphite, Nano Lett. 10 (10) (2010) 3909–3913.
[16] G.M. Rutter, J.N. Crain, N.P. Guisinger, T. Li, P.N. First, J.A. Stroscio, Scattering and interference in epitaxial graphene, Science 317 (5835) (2007) 219–222.
[17] Z.H. Aitken, R. Huang, Effects of mismatch strain and substrate surface corrugation on morphology of supported monolayer graphene, J. Appl. Phys. 107 (12) (2010) 10.
[18] D.S. Geng, S.L. Yang, Y. Zhang, J.L. Yang, J. Liu, R.Y. Li, et al., Nitrogen doping effects on the structure of graphene, Appl. Surf. Sci. 257 (21) (2011) 9193–9198.
[19] J.Q. Xu, P. Kruger, C.R. Natoli, K. Hayakawa, Z.Y. Wu, K. Hatada, X-ray absorption spectra of graphene and graphene oxide by full-potential multiple scattering calculations with self-consistent charge density, Phys. Rev. B 92 (12) (2015).
[20] R. Frost, G.E. Jonsson, D. Chakarov, S. Svedhem, B. Kasemo, Graphene oxide and lipid membranes: interactions and nanocomposite structures, Nano Lett. 12 (7) (2012) 3356–3362.
[21] W.H. Briscoe, M. Chen, I.E. Dunlop, J. Klein, J. Penfold, R.M.J. Jacobs, Applying grazing incidence X-ray reflectometry (XRR) to characterising nanofilms on mica, J. Colloid Interface Sci. 306 (2) (2007) 459–463.
[22] R.P. Giri, A. Chakrabarti, M.K. Mukhopadhyay, Cholesterol-induced structural changes in saturated phospholipid model membranes revealed through X-ray scattering technique, J. Phys. Chem. B 121 (16) (2017) 4081–4090.
[23] F. Speranza, G.A. Pilkington, T.G. Dane, P.T. Cresswell, P.X. Li, R.M.J. Jacobs, et al., Quiescent bilayers at the mica-water interface, Soft Matter 9 (29) (2013) 7028–7041.
[24] B. Sironi, T. Snow, C. Redeker, A. Slastanova, O. Bikondoa, T. Arnold, et al., Structure of lipid multilayers via drop casting of aqueous liposome dispersions, Soft Matter 12 (17) (2016) 3877–3887.
[25] S.J. Jeong, Y. Gu, J. Heo, J. Yang, C.S. Lee, M.H. Lee, et al., Thickness scaling of atomic-layer-deposited Hf02 films and their application to wafer-scale graphene tunnelling transistors, Sci. Rep. 6 (2016).
[26] M. Kalbac, V. Vales, J. Vejpravova, The effect of a thin gold layer on graphene: a Raman spectroscopy study, RSC Adv. 4 (105) (2014) 60929–60935.
[27] J.D. Emery, Q.H. Wang, M. Zarrouati, P. Fenter, M.C. Hersam, M.J. Bedzyk, Structural analysis of PTCDA monolayers on epitaxial graphene with ultra-high vacuum scanning tunneling microscopy and high-resolution X-ray reflectivity, Surf. Sci. 605 (17–18) (2011) 1685–1693.
[28] M. Conrad, J. Rault, Y. Utsumi, Y. Garreau, A. Vlad, A. Coati, et al., Structure and evolution of semiconducting buffer graphene grown on SiC(0001), Phys. Rev. B 96 (19) (2017).
[29] J.D. Emery, V.D. Wheeler, J.E. Johns, M.E. McBriarty, B. Detlefs, M.C. Hersam, et al., Structural consequences of hydrogen intercalation of epitaxial graphene on SiC(0001) (vol. 105, 161602, 2014), Appl. Phys. Lett. 107 (18) (2015).
[30] W.Y. Li, K. Goto, R. Shimizu, PEEM is a suitable tool for absolute work function measurements, Surf. Interface Anal. 37 (2) (2005) 244–247.
[31] W.H. Briscoe, F. Speranza, P.X. Li, O. Konovalov, L. Bouchenoire, J. van Stam, et al., Synchrotron XRR study of soft nanofilms at the mica-water interface, Soft Matter 8 (18) (2012) 5055–5068.
[32] A. Nelson, Co-refinement of multiple-contrast neutron/X-ray reflectivity data using MOTOFIT, J. Appl. Crystallogr. 39 (2006) 273–276.
[33] S. Stankovich, D.A. Dikin, R.D. Piner, K.A. Kohlhaas, A. Kleinhammes, Y. Jia, et al., Synthesis of graphene-based nanosheets via chemical reduction of exfoliated graphite oxide, Carbon 45 (7) (2007) 1558–1565.
[34] B. Lesiak, L. Stobinski, A. Malolepszy, M. Mazurkiewicz, L. Kover, J. Toth, Preparation of graphene oxide and characterisation using electron spectroscopy, J. Electron. Spectrosc. Relat. Phenom. 193 (2014) 92–99.
[35] L. Stobinski, B. Lesiak, A. Malolepszy, M. Mazurkiewicz, B. Mierzwa, J. Zemek, et al., Graphene oxide and reduced graphene oxide studied by the XRD, TEM and electron spectroscopy methods, J. Electron. Spectrosc. Relat. Phenom. 195 (2014) 145–154.
[36] Y.C. Lin, C.C. Lu, C.H. Yeh, C.H. Jin, K. Suenaga, P.W. Chiu, Graphene annealing: how clean can it Be? Nano Lett. 12 (1) (2012) 414–419.
[37] R.S. Yan, Q. Zhang, W. Li, I. Calizo, T. Shen, C.A. Richter, et al., Determination of graphene work function and graphene-insulator-semiconductor band alignment by internal photoemission spectroscopy, Appl. Phys. Lett. 101 (2) (2012).
[38] C.S.A. Fang, C.E. Maloney, The effect of substrate work function on work function reduction of Re/W alloy-coated impregnated cathodes, Appl. Phys. Mater. Sci. Process 50 (6) (1990) 603–607.
[39] M.T. Greiner, M.G. Helander, W.M. Tang, Z.B. Wang, J. Qiu, Z.H. Lu, Universal energy-level alignment of molecules on metal oxides, Nat. Mater. 11 (1) (2012) 76–81.
[40] H. Hibino, H. Kageshima, M. Kotsugi, F. Maeda, F.Z. Guo, Y. Watanabe, Dependence of electronic properties of epitaxial few-layer graphene on the number of layers investigated by photoelectron emission microscopy, Phys. Rev. B (12) (2009) 79.
[41] S.S. Datta, D.R. Strachan, E.J. Mele, A.T.C. Johnson, Surface potentials and layer charge distributions in few-layer graphene films, Nano Lett. 9 (1) (2009) 7–11.
[42] P. Nemes-Incze, Z. Osvath, K. Kamaras, L.P. Biro, Anomalies in thickness measurements of graphene and few layer graphite crystals by tapping mode atomic force microscopy, Carbon 46 (11) (2008) 1435–1442.
[43] A.N. Sidorov, M.M. Yazdanpanah, R. Jalilian, P.J. Ouseph, R.W. Cohn, G.U. Sumanasekera, Electrostatic deposition of graphene, Nanotechnology 18 (13) (2007).
[44] Z.H. Chen, Y.M. Lin, M.J. Rooks, P. Avouris, Graphene nano-ribbon electronics, Phys. E Low-dimens. Syst. Nanostruct. 40 (2) (2007) 228–232.
[45] P.K. Schelling, R. Keblinski, Thermal expansion of carbon structures, Phys. Rev. B (3) (2003) 68.
[46] M.Z. Islam, M. Mahboob, R.L. Lowe, Characterization of the thermal expansion properties of graphene using molecular dynamics simulations (vol. 46, 435302, 2013), J. Phys. Appl. Phys. 47 (40) (2014).
[47] D. Yoon, Y.W. Son, H. Cheong, Negative thermal expansion coefficient of graphene measured by Raman spectroscopy, Nano Lett. 11 (8) (2011) 3227–3231.
[48] S.K. Deng, V. Berry, Wrinkled, rippled and crumpled graphene: an overview of formation mechanism, electronic properties, and applications, Mater. Today 19 (4) (2016) 197–212.
[49] W.Z. Bao, F. Miao, Z. Chen, H. Zhang, W.Y. Jang, C. Dames, et al., Controlled ripple texturing of suspended graphene and ultrathin graphite membranes, Nat. Nanotechnol. 4 (9) (2009) 562–566.

Graphene surface structure in aqueous media: Evidence for an air-bubble layer and ion adsorption

Liangzhi Zhou[1], Luisa Islas [1], Nicholas Taylor[1], Oier Bikondoa[2,3], Eric Robles[4], and Wuge H. Briscoe[1]*

[1]School of Chemistry, University of Bristol, Cantock's Close, Bristol BS8 1TS, UK

[2]XMaS, the UK-CRG, European Synchrotron Radiation Facility (ESRF), 6 Rue Jules Horowitz, BP 220, 38043 Grenoble CEDEX 9, France

[3]Department of Physics, University of Warwick, Gibbet Hill Road, Coventry CV4 7AL, UK

[4]Household Care Analytical, Procter & Gamble Newcastle Innovation Centre Whitley Road, Longbenton, Newcastle NE12 9TS, UK

Abstract: Understanding graphene surface structure in aqueous media is essential for its biotechnological applications. Here, using synchrotron X-ray reflectivity (energy 14 keV), AFM imaging, and contact angle measurements, we have investigated the surface structure of CVD graphene on SiO_2/Si in water and phosphate buffered saline (PBS) at 25-60 °C. We found a diffuse layer immediately adjacent to graphene with a scattering length density (SLD) of 6.72×10^{-6} Å^{-2}, attributed to the presence of air bubbles on graphene under water. AFM imaging was indicative of interfacial inhomogeneity, but did not provide conclusive topography information on the bubble-covered graphene-water interface. The diffuse layer diminished after the graphene was submerged in water for 24 h at 25 °C. This is also evident from its enhanced wettability, with the water contact angle on graphene decreasing from 84.9±0.4° to 55.6±0.4° after submergence. An additional layer atop graphene appeared after soaking, with a thickness 10.1 Å, and a higher SLD of 19.5×10^{-6} Å^{-2} at 25 °C, which increased to 11.8 Å and 21.8×10^{-6} Å^{-2} at 60 °C in PBS, respectively. We discuss this observation in terms of ion mobility, possible formation of a silanol layer on the SiO_2 substrate, and water structure disruption at higher temperatures.

1 Introduction

Since the first exfoliation of graphene [1, 2], it has attracted intense interest in both scientific research and industrial applications as a promising 2D material due to its physicochemical properties [2, 3], including electronic properties [4], high thermal conductivity [5], mechanical strength [6], optical transparency [7], and large surface area to volume ratio. For instance, numerous studies have explored the high electrical conductivity and carrier mobility of

graphene at room temperature (RT) [2] for usage in energy storage devices [8, 9] and transistors [10, 11]. With a large active surface area, one-atom thickness, and delocalised π electrons, graphene enables the detection of changes in the surrounding environment with molecular level sensitivity [12], *e.g.* for sensing gases [12], humidity [13], and biomolecules [14]. Potential bioanalytic applications of graphene have also attracted wide attention. For these applications, graphene often needs to be exposed to or in contact with aqueous systems. Therefore, it is important to understand the structure of graphene in water, since the physical properties of graphene are influenced by its structure (*i.e.* thickness [15, 16], lattice order [17, 18], defects [19, 20], and impurities [21]) and that of the underlying substrate [22].

Several investigations have been reported on the effects of water on graphene and its derivatives. Using contact angle (CA) measurements, it has been shown that the structure (such as thickness and layer stacking) and charge transfer between graphene and its surrounding environment could influence the interaction between water and graphene [13], although the mechanism remains unclear. Specifically, it has been reported that the hydrophobicity of graphene on a copper foil [13] and a SiC wafer [23] increased with the number of graphene layers. Molecular dynamic simulations showed that free-standing graphene was hydrophobic [23, 24], due to the hydrogen bond network within a water double layer formed on the graphene surface.

Studies on the interaction between biomolecules and graphene and its derivatives in aqueous media have also been reported [14, 25]. A number of techniques for studying interfacial adsorption, such as atomic force microscopy (AFM) [26, 27], imaging total internal reflection fluorescence correlation spectroscopy (ITIR-FCS) [27], quartz crystal microbalance with dissipation monitoring technique (QCM-D), and dual polarization interferometry (DPI) [28], have been applied to graphene. In addition, adsorption of biomolecules on graphene can be monitored by changes in the electrochemical performances of graphene, using techniques such as cyclic voltammetry and differential pulse voltammetry [29, 30].

However, these methods provide limited structural information on the adsorbed molecular layer at the buried graphene-water interface. X-Ray reflectivity (XRR) is a rigorous and quantitative technique for probing structural features of nanofilms at buried interfaces [31-35] with sub-Ångström resolution. It has been used to study epitaxial graphene on SiC in air [36, 37] and in water [23]. Moreover, in combination with photoemission electron microscopy (PEEM) and AFM imaging, XRR has been recently used to provide detailed structural

The cantilever employed was SCANASYST_FLUID+ with nominal spring constant of 0.7 N m^{-1} and a tip radius of 2 nm. The static contact angle measurements were performed using the Sessile drop method on a KRÜSS® DSA100 instrument. Synchrotron XRR measurements were performed at beamline BM28-XMaS, European Synchrotron Radiation Facility (ESRF), Grenoble, France. A custom-designed liquid cell shown schematically in Figure 1 [32, 38, 41] was used for XRR experiments, with graphene samples mounted on the sample stage. The cell was sealed by two polyester (Mylar®) windows, providing a total liquid capacity of 5 ml.

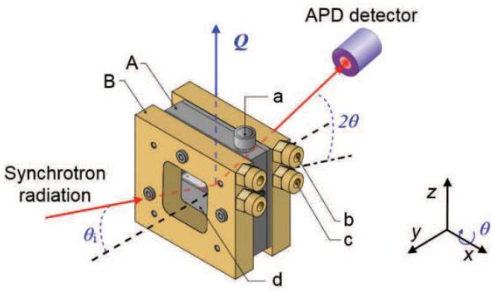

Figure 1. Schematic of the XRR experiment setup with an incident synchrotron X-ray beam reflected from the sample with an incident angle θ_i to the avalanche photodiode detector (APD) that collects the specular reflection. The momentum transfer is defined as $\boldsymbol{Q} = 4\pi sin(2\theta/2)/\lambda$, where λ is the wavelength of the X-ray beam. The sample of 1 cm × 1 cm in size is clamped onto a stainless-steel stage (d) in a customised liquid cell (A) with a nozzle (a) that allows in situ liquid/gas exchange. Temperature control can be provided by two heating jackets (B), which can be connected to a water circulating bath *via* an inlet (c) and an outlet (b).

To investigate the influence of submerging graphene in water on its surface structure, XRR curves were collected on graphene within 10 min after it was exposed to Milli-Q water, which was the time required for sample alignment. The graphene then remained submerged under water for a further 23-24 h before XRR measurements were made again. Subsequently, water was replaced by PBS, and the XRR curves were collected at 25 °C, 40 °C and 60 °C, after which the samples were cooled back to 25°C to compare with the initial stage. As a control, bare graphene that had not been submerged in water was also measured in PBS at RT. Each heating and cooling step took ~10 min and ~20 min, respectively, with a furhter10 min allowed for thermal equilibrium before the measurement was made.

The X-ray beam energy was 14 keV (with a corresponding wavelength λ = 0.8856 Å), and the beam size as defined by aperture slits was 100 μm (vertical FWHM) × ~255 μm (horizontal FWHM). A consideration for XRR measurements in aqueous media is the absorption of X-rays by water. The liquid thickness in the custom-designed XRR cell (*cf.* Figure 1) was 1 cm, permitting ~20% transmission at 14 keV X-ray energy, which is sufficient for XRR measurements [41]. Specular XRR scans were collected with the incident angle θ_i varying from 0.06-3.0° and the reflection angle $\theta_r = \theta_i$, corresponding to a momentum of transfer $\boldsymbol{Q} = 4\pi\sin(2\theta/2)/\lambda$ range of 0.015-0.74 Å^{-1}, where $2\theta = \theta_r + \theta_i$. The specular reflection was detected at each angle using an avalanche photodiode detector (APD), as shown in Figure 1. XRR data fitting was performed by using *Motofit* in Igor Pro (WaveMetrics, Inc., Lake Oswego, OR, USA), using the Abeles matrix method, which generates the same result as Parratt's recursive method [42]. A genetic algorithm optimisation is adopted in this software to minimize the χ^2 value, which shows the goodness of fitting,

$$\chi^2 = \sum_{n=1}^{L} \frac{1}{L-P}\left(y_{0,n} - y_n\right)^2, \qquad \text{Equation 1}$$

where L is the number of collected data points; P the number of variables which are varied during fitting, *e.g.* the number of layers (n), the scattering length density (SLD, ρ_n, definition and calculation in Supporting Information section SI-1), the thickness (t_n), and the interfacial roughness ($R_{a,n}$); y_0 the measured value; and y the corresponding theoretically fitted value yielded from the used parameters. Reflectivity curves with mild fringes (*i.e.* reflectivity R variations w.r.t. $\boldsymbol{Q}$) were plotted as $R\boldsymbol{Q}^4$ *vs.* $\boldsymbol{Q}$ instead of log$R$ *vs.* $\boldsymbol{Q}$, as shown in Figure 2b and Figure 5a, to show more clearly the Kiessig fringes [43]. In total, 12 XRR measurements on 3 graphene samples were studied in 2 separate synchrotron experiments, and the results shown below are representative of these measurements. The XRR curves collected from different graphene samples were reproducible.

3 Results and discussion

3.1 XRR of the graphene-water interface

XRR data fitting used a Slab Model, with ρ_n, t_n, and $R_{a,n}$ the SLD, thickness, and roughness of the n^{th} slab/layer as defined in Figure 2a. This yielded fits (χ^2 <0.0012) for the reflectivity curves of the graphene samples in different conditions. Figure 2b shows example XRR curves for bare graphene in air (circles) and water (triangles), and the soaked graphene in water (squares), with the fitted reflectivity curves shown as continuous lines. The XRR intensity

oscillations (Kiessig fringes [44]) damped (*i.e.* became less pronounced) in water compared to air due to reduced SLD contrast with graphene.

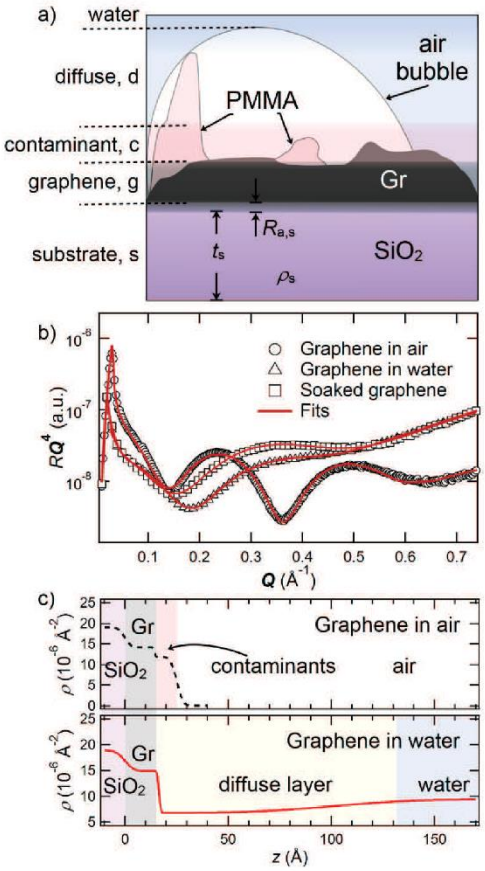

Figure 2. a) Physical model used to fit the XRR curves of graphene in water. b) The experimental (open symbols) and fitted (solid lines) XRR curves plotted as RQ^4 vs. Q for graphene in air (circles), in water (triangles), and 24 h-water soaked graphene (squares). The fitting parameters are listed in Table S2 in SI-1). c) The fitted SLD ρ_n of the graphene sample in air (dash line) and in water (solid line), plotted against z, the distance form the SiO_2 surface, with the SLD variations highlighted in different coloured regions across the interfaces of the graphene sample in air and in water. Each coloured region, with the width representing t_n,

represents a modelled layer as defined in a). The contaminant layer on graphene (represented as **Gr**) in air [38] is highlighted in pink, and a diffuse layer is present on the graphene in water.

From the fitted SLD profile of graphene in air shown in Figure 2c, the interfacial structure of the sample consisted of a graphene layer (represented as **Gr** in Figure 2a) with a contaminant layer comprising graphene multilayers and PMMA residues atop. The latter layer exhibited a thickness t_c = 11.8±1.2 Å and an SLD $\rho_c = 9.80\times10^{-6}$ Å^{-2} [38]. After the injection of water or PBS in the XRR liquid cell (*cf.* Figure 1), the contaminant layer on the graphene sample seemed undetectable, substituted by a diffuse layer at the interface with an SLD profile which gradually increased from ρ_d = ~6.7×10^{-6} Å^{-2} to $\rho_{water} = 9.44\times10^{-6}$ Å^{-2} of the bulk water. The SLD of this diffuse layer was smaller than that of graphene ($\rho_g = 18.20\times10^{-6}$ Å^{-2}) or PMMA ($\rho_{PMMA} = 10.81\times10^{-6}$ Å^{-2}), and was between that of air ($\rho_{air} = 0$ Å^{-2}) and water, whilst the high roughness $R_{a,d}$ (>30 Å) value indicates a highly heterogenous interfacial structure (fitted values shown in Table 1). We suggest that this reduced SLD of the interfacial layer could be attributed to the formation of flattened air bubbles of nonuniform coverage on the graphene surface, as shown schematically in Figure 2a. The mixed SLD (ρ_{mix}) of a binary mixture could be calculated as

$$\rho_{mix} = \phi\rho_1 + (1-\phi)\rho_2, \qquad \text{Equation 2}$$

where ϕ is the volume fraction of one component and ρ_i is the SLD of constituent i, respectively; the volume fraction of air in this diffuse layer, ϕ_{air}, can be then calculated, which is ~30 % as shown in Table 1 and the calculation method of ϕ_{air} is described in detail in SI-1.3. Such an SLD reduction has been previously observed on a rough polystyrene surface [45]. Further AFM imaging suggested that this diffuse layer was a consequence of both the contaminant and the air bubbles present on the surface [46].

Table 1. Fitting parameters for the XRR data collected from graphene in air, in water, in PBS, and 24 h water-soaked graphene in water at 25 ºC.

Sample	**Layers in the Slab Model**	t_n **(Å)**	ρ_n **(10^{-6} Å^{-2})**	$R_{a,n}$ **(Å)**	ϕ_{air} **(%)**	χ^2 **(10^{-3})**
Graphene in air at 25°C	Contaminants	10.8	11.87	2.4		
	Graphene	14.4	14.13	0.4	100	1.11
	SiO_2	3000	19.01	2.4		

Graphene in water at 25°C	Diffuse layer	84.9	6.72	31.9	36.7	0.47
	Graphene	16.5	14.93	0.7		
	SiO_2	3000	18.91	3.4		
Graphene in PBS at 25 °C	Diffuse layer	118.3	6.75	49.3	30.9	0.71
	Graphene	15.4	19.71	4.5		
	SiO_2	3000	18.91	3.5		
Soaked graphene in water at 25°C	Ion adsorbed layer	10.1	19.45	1.0	0	0.19
	Graphene	5.0	14.91	2.3		
	silanol	78.9	21.32	4.6		
	SiO_2	3000	18.96	69.7		

3.2 AFM imaging at the graphene-water interface

AFM topological images (Figure 3a) have also been collected to reveal the morphology of the graphene-water interface and were processed using the *NanoScope Analysis* software. The topological image of the graphene sample in air was comprised of the SiO_2 substrate, graphene, and the defects (highlighted in white rectangles in Figure 3a) that consisted of PMMA and multilayer graphene flakes [38]. However, it was a lot more challenging to obtain good quality, reproducible images under water, which is probably ascribable to a more complicated structure with inhomogeneous coverage. In addition, the presence of soft air bubbles could make it difficult for the AFM scanning tip to engage with surface. As a result, the AFM images of the graphene-water interface did not provide conclusive supporting evidence for the presence of the bubbles.

For the example under-water image shown in Figure 3a, the maximum difference in the height, Δh_{max}, increased by ~11 Å compared to air (Table 2). Meanwhile, the graphene roughness given by the height deviation R_{ave} and height root-mean square R_{sq} also increased, consistent with a more inhomogeneous interface caused by the formation of air bubbles (high resolution AFM topological images in Figure S3a in SI-2).

Table 2. The maximum difference in the relative height, Δh_{max}, the root-mean square average, R_{sq}, and the arithmetic average values of height deviations, R_{ave}, of the surface height deviations in the AFM topological images of graphene in air and in water following the plane fitting.

	Δh_{max} (Å)	R_{sq} (Å)	R_{ave} (Å)
In air	124	6.61	4.68
In water	135	10.8	8.37

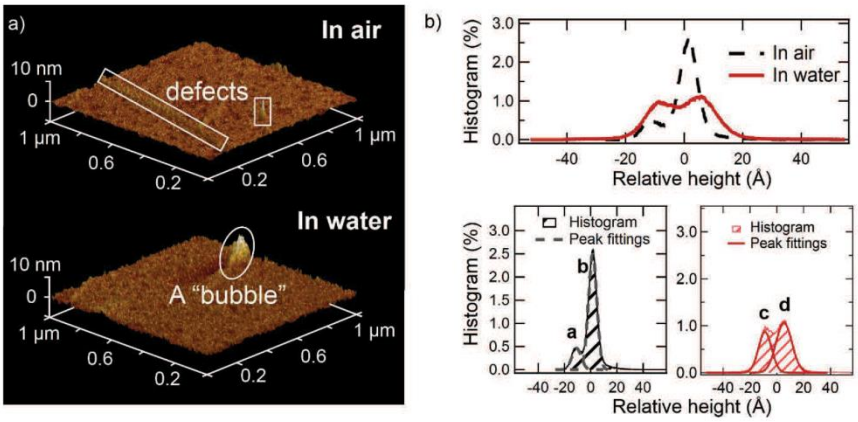

Figure 3. a) Example AFM topological images of graphene and its defects (indicated by the rectangles) in air, and a possible bubble (indicated by an oval) in water on a 1 μm × 1 μm scale; and b) the corresponding histograms of height distributions on the sample surface with the Gaussian peak fittings for the measurements in air (left) and in water (right).

It can be observed from the Gaussian peak fittings shown in Figure 3b that the height distribution on the solid-water interface (with FWHM values of peaks **c** and **d** 11.5 Å and 10.6 Å, respectively) was broader than that at the air-water interface (with peaks **a** and **b** possessing FWHM values 8.4 Å and 7.5 Å, respectively), suggesting the existence of more inhomogeneous structures on the graphene-water interface compared to air. Particularly, as indicated by an oval in Figure 3a, a bubble-like area of size ~189 nm (length) × 88 nm (width) × 10 nm (height) was detected. The air bubble layer from XRR fitting (*cf.* Table 1) has a smaller thickness (t_d = 84.9 Å) but a higher roughness ($R_{a,d}$ = 31.9 Å). One possible reason for the differences is that the XRR measures and thus gives the average value of a surface layer over a much larger footprint (~200 μm × 1 cm), whilst AFM measures a much smaller sample area (~ a few μm^2) and thus reflects a much more localized structure [38]. It should be borne in mind that a more complex structure could be present on graphene, including residual PMMA contaminants and graphene multilayers, which could not be distinguished by topological images only. Although AFM

imaging did not provide conclusive topography information on graphene under water, it indicated that the interfacial structure was different from that in air. It was also qualitatively consistent with the XRR results which were indicative of an inhomogeneous interface. Further effort with AFM imaging remains a focus of our future work.

3.3 Effect of submerging CVD graphene on Si/SiO_2 under water

The sessile drop water contact angles (CAs) of graphene before and after soaking graphene in water for 24 h are shown in Figure 4b. For the soaked graphene samples, the water residues were removed by two methods: drying naturally or using an Ar flow to dry the surface gently. A noticeable reduction of graphene water CA was observed with both methods. The results (described in detail in SI-3) showed that the water CA on graphene decreased from 84.9±0.4° to 55.6±0.4° after it had been submerged under water for 24 h, indicating that the graphene sample became more hydrophilic. Whether graphene is hydrophobic or hydrophilic is still somewhat controversial in the literature. Graphene was once believed to have similar wettability to graphite (water CA = ~80-100°), while some CA measurements suggested it was hydrophobic, and even superhydrophobicity [47]. More recent studies showed that the interaction between water and graphene was affected by the graphene surface structure and related parameters, such as the graphene layer thickness [23, 48], the presence of defects [23, 47] and adsorbates [24, 47], underlying substrates [49], and the doping of graphene [50]. Both the surface energy and the topological features should contribute to the observed wettability of such a heterogeneous material. Thus, it is possible that graphene hydrophobicity reflects its various surface roughness and related chemical inhomogeneities due to different fabrication methods [47, 48].

It has been reported that trapped air bubbles could form at the solid-liquid interface particularly when nanotextures or multi-scale roughness were present at the interface, resulting in the Cassie–Baxter wetting state, which would then lower the solid-liquid adhesion and manifest in apparent higher hydrophobicity [51, 52]. If water permeates the surface textures, transforming the wettability from the Cassie-Baxter state to the Wenzel state [53], the hydrophobicity of the material would decrease, consistent with our observation of the decreased CA after 24 h water submergence. In addition, the SLD profile in Figure 4a indicates that no diffuse air-bubble layer was present on top of graphene after water-soaking, and that water had fully spread on the surface, as shown schematically in Figure 4c. The fitted graphene thickness $t_{g(water)}$ = 5.0 Å with $\rho_g = 14.91\times10^{-6}$ Å^{-2}, decreased appreciably after soaking, compared with the graphene

thickness $t_{g(air)}$ = 14.4 Å detected in air. In the meantime, an additional layer appeared, with a higher SLD $\rho_a = 19.5\times10^{-6}$ Å^{-2}, and thickness t_a = 10.1 Å. The total thickness $t_{total} = t_{g(water)} + t_a$ = 15.1 Å is very similar to $t_{g(air)}$, and we attributed this observation to the adsorption of ions within the defect structures on graphene, which will be discussed below in section 3.4.

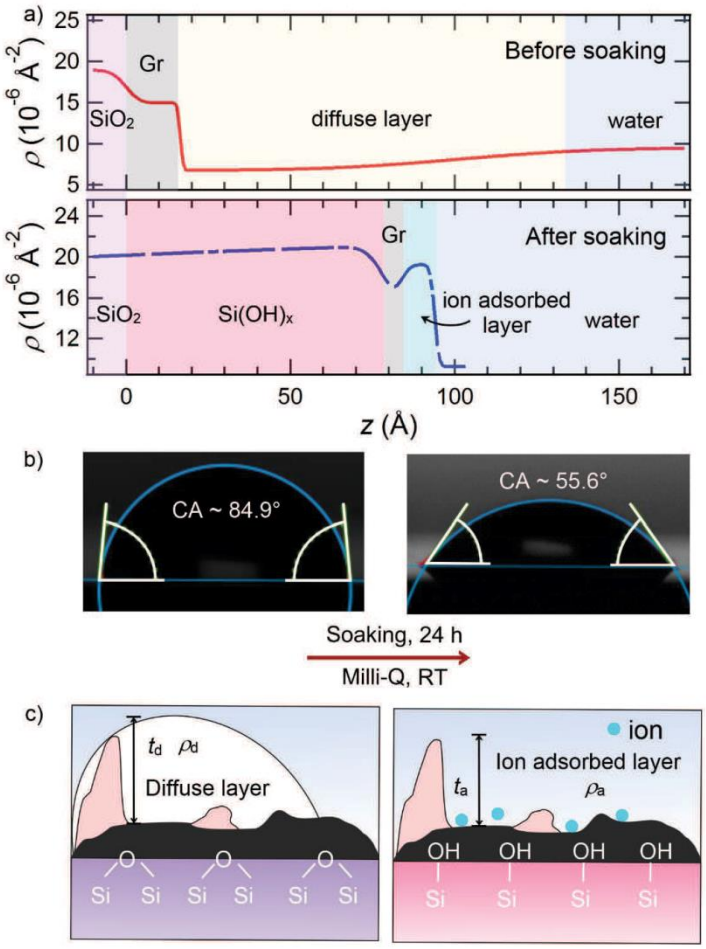

Figure 4. a) Fitted XRR SLD profiles in water of the un-soaked graphene (red solid line) and soaked graphene (blue dashed line), with the coloured regions representing different layers in the Slab Model used to fit the data. b) The water CA = 84.9° of a bare graphene sample reduced to CA = 55.6° after soaking in Milli-Q for 24 h. The diminishing of the air bubble layer, the

hydration of the SiO_2 substrate, and the formation of the ion adsorbed layer upon soaking are schematically illustrated in (c).

Furthermore, the SLD of the underlying substrate increased from $\rho_s = 18.91\times10^{-6}$ Å^{-2} before water soaking, a value matching the theoretical SLD of SiO_2, to $\rho_s = 21.32\times10^{-6}$ Å^{-2} after soaking (*cf.* Table 2). We attributed this to the formation of $Si(OH)_x$ by the rehydration of the amorphous silica, as the SLD of silanol is $\rho = 28.72\times10^{-6}$. Water molecules can permeate through graphene lattices and interact with silica substrate [54], leading to a higher electron density due to the formation of hydroxyl groups on the surface. The silica substrate is normally stable in water, and the formation of silanol layer is not considered in most of the cases, because of the low diffusion velocity of water molecules (only 6 Å per 1000 min at 25 ºC) in bulk silica. However, molecular diffusion can be accelerated by increasing temperature [55]. We thus postulate that the prolonged submergence of the sample in water and subsequent increased temperature during XRR measurements led to the formation of detectable silanol groups.

The fitted thickness of the silanol layer is t_s = ~75 Å, a value much higher than the theoretical one (8.64 Å after soaking in water for 24 h [55]), and the ρ_s profile also decreased gradually towards the bulk silica. Meanwhile, the fitted roughness of the silica substrate is also high $R_{a,silica}$ = ~65 Å. It is possible for water to penetrate the amorphous silica, leading to a relatively thick and rough interfacial layer. The observation of this silanol layer underneath graphene has important implications, as the acidity of silanol could lead to high affinity for ions and biomolecules [56]. It has also been reported that the presence of silanol on the SiO_2 substrate underlying graphene could change the electric properties of graphene, due to the electric dipoles possessed by the adsorbed water [57].

3.4 Effect of temperature and PBS on CVD graphene on Si/SiO_2

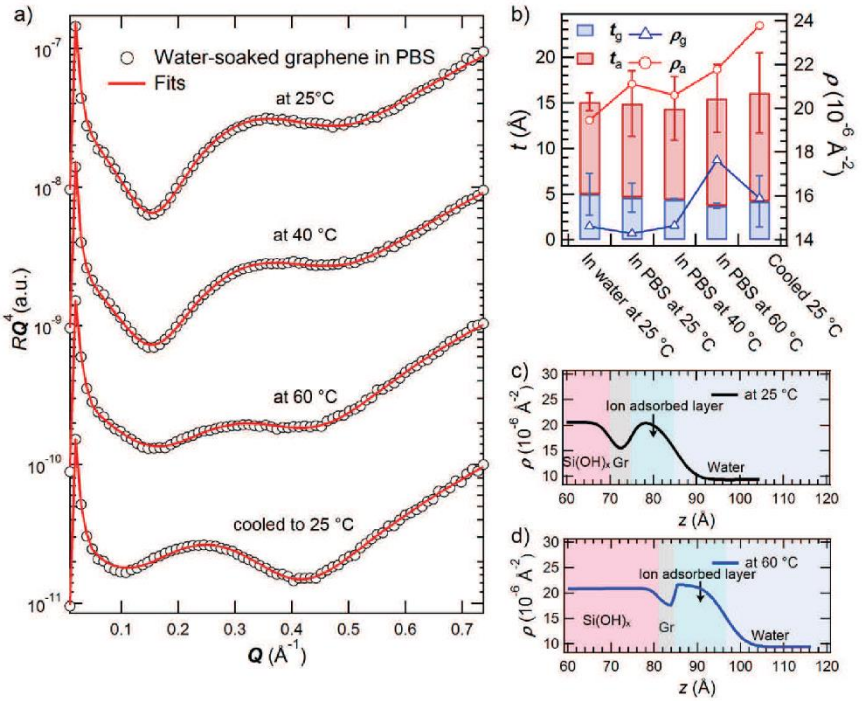

Figure 5. a) The experimental (open circles) and fitted (solid lines) XRR curves (offset vertically for clarity) of water-soaked graphene in PBS at different temperatures, with the fitting parameters (t_n, ρ_n and $R_{a,n}$) tabulated in Table S2. The fits show that the graphene thickness t_g remained at ~4.2 Å at all temperatures; while its SLD was relatively constant at ρ_g ~15×10^{-6} Å^{-2} at lower temperatures, it increased to $\rho_g = 17.6\times10^{-6}$ Å^{-2} at 60 °C. Similarly, the SLD and thickness of the ion adsorbed layer ρ_a and t_a increased at 60 °C, and the increment remained after cooling back to RT as shown in b). The SLD profiles of graphene samples at 25 °C and 60 °C are shown in (c) and (d), respectively, which show that the thickness of the silanol layer also increased at 60 °C, with the interface between graphene and the ion adsorbed layer becoming smoother.

Figure 5a shows XRR curves of water-soaked graphene in PBS, at 25 °C, 40 °C, 60 °C, and then cooled back down to 25 °C. The change in the Kiessig fringes is noticeable upon heating and cooling, and the XRR profiles are also different from those in pure water (*cf.* Figure 2c). The fitting parameters and SLD profiles for these XRR curves are given in Table S2 and Figure

S2, respectively, in SI-1. The thickness t_a and SLD ρ_a of the ion adsorbed layer atop graphene (as illustrated in Figure 4c in section 3.3) increased after water was replaced with PBS at RT. In addition, as listed in Table 1, the fitted SLD value $\rho_g = 19.17\times10^{-6}$ Å^{-2} of un-soaked graphene is also higher in PBS than that in air ($\rho_g = 14.93\times10^{-6}$ Å^{-2}). This again is consistent with the assumption of ion adsorption on graphene. It has been shown by molecular dynamics simulations that graphene could attract, due to π-conjunction and polarizability, both cations [58-60] and anions [61, 62], such as Na^+ ($\rho = 86.75\times10^{-6}$ Å^{-2}) and K^+ ($\rho = 55.06\times10^{-6}$ Å^{-2}) in PBS to the graphene-water interface. Furthermore, the fitted SLD profiles to the XRR curves of the soaked graphene in PBS at 25 °C (Figure 5c) and 60 °C (Figure 5d) also show that ion adsorption was promoted upon heating. The thickness and SLD of the ion adsorbed layer increased to $t_a = 11.8$ Å, and $\rho_a = 21.8\times10^{-6}$ Å^{-2}, with respective increment $\Delta\rho_a = 0.7\times10^{-6}$ Å^{-2} and $\Delta t_a = 1.5$ Å compared with 25 °C), whilst the graphene thickness $t_g = 4.2$ Å (*cf.* the theoretical thickness of a monolayer graphene of 3.35 Å) remained constant, with the fitted SLD in PBS $\rho_g = \sim15\times10^{-6}$ Å^{-2} also comparable to that in air.

The interfacial roughness $R_{a,g}$ between graphene and the ion adsorbed layer decreased at higher temperatures (Figure 5b), which could be due to the ions residing in the defects and on the contaminants of the graphene surface and reducing the apparent roughness. The thickness t_s of the silanol layer also increased upon heating (Figure 5d), thereby promoting ion adsorption to the substrate [56]. The effect of temperature on the ion adsorption can be triggered by the enhanced mobility of ions at higher temperatures [63]. In addition, the structure of graphene itself can also play an important role in response to the temperature-dependent ion adsorption. A simulation study has reported that water could form an ice-like double layer structure on free standing graphene, preventing the interaction between graphene and the bulk solution [24]. This interfacial water structure was found disrupted at 340 K (67 °C), which is close to where we observed enhanced ion adsorption.

4 Summary and concluding remarks

In this study, we have applied synchrotron XRR to characterise the surface structure of graphene in water and PBS. The surface structure of graphene submerged under water for 24 h was also studied. AFM imaging provided inconclusive topological morphology of graphene under water, due to the intrinsic experimental difficulties associated with the technique while imaging a soft, bubble-covered surface. The surface roughness data however was consistent with a much more inhomogeneous graphene-water interface compared to air. Fitting the SLD

to the XRR curves on graphene indicated the presence of an air bubble layer (ρ_d = 6.72×10^{-6} Å^{-2}, t_d = 84.9 Å, and $R_{a,d}$ = 31.9 Å) on top of graphene when firstly immersing it in water. AFM imaging also revealed the presence of isolated bubbles (*e.g.* ~189 nm (length) × 88 nm (width) × 10 nm (height)) on graphene. These bubbles of a few nm in height with a flattened morphology diminished after the graphene sample was submerged under water for a prolonged period. Concurrently, the water contact angle on graphene decreased from 84.9±0.4° (before soaking) to 55.6±0.4° (after soaking), indicating a decrease in its hydrophobicity, which is consistent with the XRR evidence for the diminishment of the air bubble layer. XRR results also suggested that, after water soaking, a silanol layer formed on the SiO_2/Si substrate, which could alter the electric properties of the graphene/silica sample [57]. Furthermore, ion adsorption was inferred from the increased SLD of the layer atop graphene observed on water-soaked graphene in PBS, with the fitted interfacial structure consisting of an additional ion adsorbed layer. The ion adsorption was enhanced by heating the solution to 60 ºC, which was retained after cooling. We attributed this change to the higher ion mobility, the higher ion affinity of the formed silanol layer on the substrate, and the disruption of the ordered water structure at high temperatures as reported previously [24]. These unprecedented results are relevant to bioanalytic and nanotechnological applications of graphene in which its structure at the interface between water and electrolyte solutions is an important consideration to the efficacy and functionality of the devices or the processes. The capability of XRR to detect the air bubbles exist on the hydrophobic interfaces can be also utilized on examining the wettability of a surface with sub-micro precision, compared with CA measurements that only provide the bulk wetting.

Acknowledgement

We acknowledge funding from the Engineering and Physical Science Research Council (EPSRC EP/H034862/1, EP/K035746/1 for PeakForce atomic force microscopy that was carried out by Dr R. Harniman in the Chemical Imaging Facility, University of Bristol). Funding from the Royal Society, the European Cooperation in Science and Technology (CMST COST) Action CM1101, the Consejo Nacional de Ciencia y Tecnologia (CONACyT) Postdoctoral Fellowship 291231, and the Marie Curie Initial Training Network (MC-ITN) "Soft, Small, and Smart: Design, Assembly, and Dynamics of Novel Nanoparticles for Novel Industrial Applications (NanoS3)" (FP7 Grant No. 290251) was also acknowledged. We also thank P&G for financial support *via* the Bristol Final Year Industrial Project Scheme.

Synchrotron X-ray access at ESRF CRG XMas beamline and the support by the beamline staff is acknowledged. XMaS is a UK national facility supported by EPSRC.

References

[1] K.S. Novoselov, A.K. Geim, S.V. Morozov, D. Jiang, Y. Zhang, S.V. Dubonos, I.V. Grigorieva, A.A. Firsov, Electric field effect in atomically thin carbon films, Science 306(5696) (2004) 666-669.
[2] K.S. Novoselov, V.I. Fal'ko, L. Colombo, P.R. Gellert, M.G. Schwab, K. Kim, A roadmap for graphene, Nature 490(7419) (2012) 192-200.
[3] A.K. Geim, Graphene: Status and Prospects, Science 324(5934) (2009) 1530-1534.
[4] A.H. Castro Neto, F. Guinea, N.M.R. Peres, K.S. Novoselov, A.K. Geim, The electronic properties of graphene, Rev Mod Phys 81(1) (2009) 109-162.
[5] A.A. Balandin, Thermal properties of graphene and nanostructured carbon materials, Nat Mater 10(8) (2011) 569-581.
[6] C. Lee, X.D. Wei, J.W. Kysar, J. Hone, Measurement of the elastic properties and intrinsic strength of monolayer graphene, Science 321(5887) (2008) 385-388.
[7] Z. Lee, K.J. Jeon, A. Dato, R. Erni, T.J. Richardson, M. Frenklach, V. Radmilovic, Direct Imaging of Soft-Hard Interfaces Enabled by Graphene, Nano Lett 9(9) (2009) 3365-3369.
[8] D.A.C. Brownson, D.K. Kampouris, C.E. Banks, An overview of graphene in energy production and storage applications, J Power Sources 196(11) (2011) 4873-4885.
[9] Q. Wu, Y.X. Xu, Z.Y. Yao, A.R. Liu, G.Q. Shi, Supercapacitors Based on Flexible Graphene/Polyaniline Nanofiber Composite Films, Acs Nano 4(4) (2010) 1963-1970.
[10] F. Schwierz, Graphene transistors, Nat Nanotechnol 5(7) (2010) 487-496.
[11] L. Britnell, R.V. Gorbachev, R. Jalil, B.D. Belle, F. Schedin, A. Mishchenko, T. Georgiou, M.I. Katsnelson, L. Eaves, S.V. Morozov, N.M.R. Peres, J. Leist, A.K. Geim, K.S. Novoselov, L.A. Ponomarenko, Field-Effect Tunneling Transistor Based on Vertical Graphene Heterostructures, Science 335(6071) (2012) 947-950.
[12] O. Leenaerts, B. Partoens, F.M. Peeters, Adsorption of H(2)O, NH(3), CO, NO(2), and NO on graphene: A first-principles study, Phys Rev B 77(12) (2008).
[13] C. Melios, C.E. Giusca, V. Panchal, O. Kazakova, Water on graphene: review of recent progress, 2d Mater 5(2) (2018).
[14] Y. Wang, Z.H. Li, J. Wang, J.H. Li, Y.H. Lin, Graphene and graphene oxide: biofunctionalization and applications in biotechnology, Trends Biotechnol 29(5) (2011) 205-212.
[15] M.S. Xu, D. Fujita, J.H. Gao, N. Hanagata, Auger Electron Spectroscopy: A Rational Method for Determining Thickness of Graphene Films, Acs Nano 4(5) (2010) 2937-2945.
[16] W.Y. Jang, Z. Chen, W.Z. Bao, C.N. Lau, C. Dames, Thickness-Dependent Thermal Conductivity of Encased Graphene and Ultrathin Graphite, Nano letters 10(10) (2010) 3909-3913.
[17] G.M. Rutter, J.N. Crain, N.P. Guisinger, T. Li, P.N. First, J.A. Stroscio, Scattering and interference in epitaxial graphene, Science 317(5835) (2007) 219-222.
[18] Z.H. Aitken, R. Huang, Effects of mismatch strain and substrate surface corrugation on morphology of supported monolayer graphene, Journal of Applied Physics 107(12) (2010) 10.
[19] A.W. Robertson, C.S. Allen, Y.A. Wu, K. He, J. Olivier, J. Neethling, A.I. Kirkland, J.H. Warner, Spatial control of defect creation in graphene at the nanoscale, Nat Commun 3 (2012).
[20] F. Banhart, J. Kotakoski, A.V. Krasheninnikov, Structural Defects in Graphene, Acs Nano 5(1) (2011) 26-41.
[21] Y.C. Lin, C.C. Lu, C.H. Yeh, C.H. Jin, K. Suenaga, P.W. Chiu, Graphene Annealing: How Clean Can It Be?, Nano Lett 12(1) (2012) 414-419.
[22] Z.H. Ni, L.A. Ponomarenko, R.R. Nair, R. Yang, S. Anissimova, I.V. Grigorieva, F. Schedin, P. Blake, Z.X. Shen, E.H. Hill, K.S. Novoselov, A.K. Geim, On Resonant Scatterers As a Factor Limiting Carrier Mobility in Graphene, Nano Lett 10(10) (2010) 3868-3872.
[23] H. Zhou, P. Ganesh, V. Presser, M.C.F. Wander, P. Fenter, P.R.C. Kent, D.E. Jiang, A.A. Chialvo, J. McDonough, K.L. Shuford, Y. Gogotsi, Understanding controls on interfacial wetting at epitaxial graphene: Experiment and theory, Phys Rev B 85(3) (2012).

[24] A. Akaishi, T. Yonemaru, J. Nakamura, Formation of Water Layers on Graphene Surfaces, Acs Omega 2(5) (2017) 2184-2190.
[25] S. Gurunathan, J.H. Kim, Synthesis, toxicity, biocompatibility, and biomedical applications of graphene and graphene-related materials, Int J Nanomed 11 (2016) 1927-1945.
[26] H.Z. Lei, X.J. Zhou, H.X. Wu, Y. Song, J. Hu, S.W. Guo, Y. Zhang, Morphology Change and Detachment of Lipid Bilayers from the Mica Substrate Driven by Graphene Oxide Sheets, Langmuir 30(16) (2014) 4678-4683.
[27] P.K. Ang, M. Jaiswal, C.H.Y.X. Lim, Y. Wang, J. Sankaran, A. Li, C.T. Lim, T. Wohland, B. Ozyilmaz, K.P. Loh, A Bioelectronic Platform Using a Graphene-Lipid Bilayer Interface, Acs Nano 4(12) (2010) 7387-7394.
[28] R. Frost, G.E. Jonsson, D. Chakarov, S. Svedhem, B. Kasemo, Graphene Oxide and Lipid Membranes: Interactions and Nanocomposite Structures, Nano Lett 12(7) (2012) 3356-3362.
[29] A. Rabti, N. Raouafi, A. Merkoci, Bio(Sensing) devices based on ferrocene-functionalized graphene and carbon nanotubes, Carbon 108 (2016) 481-514.
[30] D. Khatayevich, T. Page, C. Gresswell, Y. Hayamizu, W. Grady, M. Sarikaya, Selective detection of target proteins by peptide-enabled graphene biosensor, Small 10(8) (2014) 1505-13, 1504.
[31] W.H. Briscoe, M. Chen, I.E. Dunlop, J. Klein, J. Penfold, R.M.J. Jacobs, Applying grazing incidence X-ray reflectometry (XRR) to characterising nanofilms on mica, J Colloid Interf Sci 306(2) (2007) 459-463.
[32] F. Speranza, G.A. Pilkington, T.G. Dane, P.T. Cresswell, P.X. Li, R.M.J. Jacobs, T. Arnold, L. Bouchenoire, R.K. Thomas, W.H. Briscoe, Quiescent bilayers at the mica-water interface, Soft Matter 9(29) (2013) 7028-7041.
[33] B. Sironi, T. Snow, C. Redeker, A. Slastanova, O. Bikondoa, T. Arnold, J. Klein, W.H. Briscoe, Structure of lipid multilayers via drop casting of aqueous liposome dispersions, Soft Matter 12(17) (2016) 3877-3887.
[34] M. Wlodek, M. Kolasinska-Sojka, M. Wasilewska, O. Bikondoa, W.H. Briscoe, P. Warszynski, Interfacial and structural characteristics of polyelectrolyte multilayers used as cushions for supported lipid bilayers, Soft Matter 13(43) (2017) 7848-7855.
[35] T.G. Dane, P.T. Cresswell, O. Bikondoa, G.E. Newby, T. Arnold, C.F.J. Faul, W.H. Briscoe, Structured oligo(aniline) nanofilms via ionic self-assembly, Soft Matter 8(10) (2012) 2824-2832.
[36] M. Conrad, J. Rault, Y. Utsumi, Y. Garreau, A. Vlad, A. Coati, J.P. Rueff, P.F. Miceli, E.H. Conrad, Structure and evolution of semiconducting buffer graphene grown on SiC(0001), Phys Rev B 96(19) (2017).
[37] J.D. Emery, V.H. Wheeler, J.E. Johns, M.E. McBriarty, B. Detlefs, M.C. Hersam, D.K. Gaskill, M.J. Bedzyk, Structural consequences of hydrogen intercalation of epitaxial graphene on SiC(0001), Appl Phys Lett 105(16) (2014).
[38] L. Zhou, L. Fox, M. Wlodek, L. Islas, A. Slastanova, E. Robles, O. Bikondoa, R. Harniman, N. Fox, M. Cattelan, W.H. Briscoe, Surface structure of few layer graphene, Carbon 136 (2018) 255-261.
[39] P.K. Ang, M. Jaiswal, C. Lim, Y. Wang, J. Sankaran, A. Li, C.T. Lim, T. Wohland, B. Ozyilmaz, K.P. Loh, A Bioelectronic Platform Using a Graphene-Lipid Bilayer Interface, Acs Nano 4(12) (2010) 7387-7394.
[40] K. Yamazaki, S. Kunii, T. Ogino, Characterization of Interfaces between Graphene Films and Support Substrates by Observation of Lipid Membrane Formation, J Phys Chem C 117(37) (2013) 18913-18918.
[41] W.H. Briscoe, F. Speranza, P.X. Li, O. Konovalov, L. Bouchenoire, J. van Stam, J. Klein, R.M.J. Jacobs, R.K. Thomas, Synchrotron XRR study of soft nanofilms at the mica-water interface, Soft Matter 8(18) (2012) 5055-5068.
[42] A. Nelson, Co-refinement of multiple-contrast neutron/X-ray reflectivity data using MOTOFIT, J Appl Crystallogr 39 (2006) 273-276.
[43] G. Porod, Die Rontgenkleinwinkelstreuung Von Dichtgepackten Kolloiden Systemen .1., Kolloid Z Z Polym 124(2) (1951) 83-114.
[44] J. Als-Nielsen, D. McMorrow, Elements of modern X-ray physics, Wiley,, Hoboken, 2011, pp. xii, 419 pages.

[45] J.R. Howse, R. Steitz, M. Pannek, P. Simon, D.W. Schubert, G.H. Findenegg, Adsorbed surfactant layers at polymer/liquid interfaces. A neutron reflectivity study, Phys Chem Chem Phys 3(18) (2001) 4044-4051.
[46] R. Steitz, T. Gutberlet, T. Hauss, B. Klosgen, R. Krastev, S. Schemmel, A.C. Simonsen, G.H. Findenegg, Nanobubbles and their precursor layer at the interface of water against a hydrophobic substrate, Langmuir 19(6) (2003) 2409-2418.
[47] A. Ashraf, Y.B. Wu, M.C. Wang, N.R. Aluru, S.A. Dastgheib, S. Nam, Spectroscopic Investigation of the Wettability of Multilayer Graphene Using Highly Ordered Pyrolytic Graphite as a Model Material, Langmuir 30(43) (2014) 12827-12836.
[48] C. Melios, A. Centeno, A. Zurutuza, V. Panchal, C.E. Giusca, S. Spencer, S.R.P. Silva, O. Kazakova, Effects of humidity on the electronic properties of graphene prepared by chemical vapour deposition, Carbon 103 (2016) 273-280.
[49] J. Rafiee, X. Mi, H. Gullapalli, A.V. Thomas, F. Yavari, Y.F. Shi, P.M. Ajayan, N.A. Koratkar, Wetting transparency of graphene, Nat Mater 11(3) (2012) 217-222.
[50] A. Ashraf, Y. Wu, M.C. Wang, K. Yong, T. Sun, Y. Jing, R.T. Haasch, N.R. Aluru, S. Nam, Doping-Induced Tunable Wettability and Adhesion of Graphene, Nano Lett 16(7) (2016) 4708-12.
[51] A. Tuteja, W. Choi, M.L. Ma, J.M. Mabry, S.A. Mazzella, G.C. Rutledge, G.H. McKinley, R.E. Cohen, Designing superoleophobic surfaces, Science 318(5856) (2007) 1618-1622.
[52] M. Nosonovsky, B. Bhushan, Superhydrophobic surfaces and emerging applications: Non-adhesion, energy, green engineering, Curr Opin Colloid In 14(4) (2009) 270-280.
[53] M. Sbragaglia, A.M. Peters, C. Pirat, B.M. Borkent, R.G.H. Lammertink, M. Wessling, D. Lohse, Spontaneous breakdown of superhydrophobicity, Phys Rev Lett 99(15) (2007).
[54] T.O. Wehling, A.I. Lichtenstein, M.I. Katsnelson, First-principles studies of water adsorption on graphene: The role of the substrate, Appl Phys Lett 93(20) (2008).
[55] R.H. Doremus, Internal Hydroxyl Groups near Surface of Silica, J Phys Chem-Us 75(20) (1971) 3147-&.
[56] A.A. Hassanali, S.J. Singer, Model for the water-amorphous silica interface: The undissociated surface, J Phys Chem B 111(38) (2007) 11181-11193.
[57] J. Sabio, C. Seoanez, S. Fratini, F. Guinea, A.H. Castro, F. Sols, Electrostatic interactions between graphene layers and their environment, Physical Review B 77(19) (2008).
[58] M.L. Sun, W.C. Tang, Q.Q. Ren, S.K. Wang, JinYu, Y.H. Du, Y.J. Zhang, First-principles study of the alkali earth metal atoms adsorption on graphene, Appl Surf Sci 356 (2015) 668-673.
[59] A. Bostwick, T. Ohta, T. Seyller, K. Horn, E. Rotenberg, Quasiparticle dynamics in graphene, Nat Phys 3(1) (2007) 36-40.
[60] O.I. Malyi, K. Sopiha, V.V. Kulish, T.L. Tan, S. Manzhos, C. Persson, A computational study of Na behavior on graphene, Appl Surf Sci 333 (2015) 235-243.
[61] D.L. McCaffrey, S.C. Nguyen, S.J. Cox, H. Weller, A.P. Alivisatos, P.L. Geissler, R.J. Saykally, Mechanism of ion adsorption to aqueous interfaces: Graphene/water vs. air/water, P Natl Acad Sci USA 114(51) (2017) 13369-13373.
[62] G.S. Shi, Y.H. Ding, H.P. Fang, Unexpectedly strong anion-p interactions on the graphene flakes, J Comput Chem 33(14) (2012) 1328-1337.
[63] M. Tabrizchi, F. Rouholahnejad, Comparing the effect of pressure and temperature on ion mobilities, J Phys D Appl Phys 38(6) (2005) 857-862.

References

1. Lesiak, B., et al., *Preparation of graphene oxide and characterisation using electron spectroscopy.* Journal of Electron Spectroscopy and Related Phenomena, 2014. **193**: p. 92-99.

2. Tang, L.H., et al., *Preparation, structure, and electrochemical properties of reduced graphene sheet films.* Advanced Functional Materials, 2009. **19**(17): p. 2782-2789.

3. Thomas, J.C., *The determination of log normal particle-size distributions by dynamic light-scattering.* Journal of Colloid and Interface Science, 1987. **117**(1): p. 187-192.

4. Sironi, B., et al., *Structure of lipid multilayers via drop casting of aqueous liposome dispersions.* Soft Matter, 2016. **12**(17): p. 3877-3887.

5. Patterson, A.L., *The scherrer formula for X-ray particle size determination.* Physical Review, 1939. **56**(10): p. 978-982.